UNIVERSITY OF CALIFORNIA, MERCED

Modeling Light Propagation in Luminescent Media

A dissertation submitted
in partial fulfillment of the requirements
for the degree Doctor of Philosophy

in

Applied Mathematics

by

Derya Şahin

Committee in charge:

Professor Boaz Ilan, Chair

Professor Francois Blanchette

Professor Arnold D. Kim

2014

The Dissertation of Derya Şahin is approved, and it is acceptable
in quality and form for publication on microfilm and electronically:

Francois Blanchette

Arnold D. Kim

Boaz Ilan, Chair

University of California, Merced

2014

Contents

I would like to dedicate my thesis to my loving husband Berk Biryol and my wonderful parents. They have given me their unequivocal support throughout, as always, for which my mere expression of thanks does not suffice. Teşekkürler güzel ailem.

Acknowledgements

It would not have been possible to write this doctoral thesis without the help and support of the kind people around me, to only some of whom it is possible to give particular mention here.

Foremost, I would like to express my sincere gratitude to my advisor Prof. Boaz Ilan for his continuous support, kindness, patience, motivation, and enthusiasm. His guidance helped me in all the time of my research. I am greatly indebted to him.

Besides my advisor, I would like to express my gratitude to my thesis committee: Prof. Arnold D. Kim and Prof. Francois Blanchette for their encouragement, insightful comments and questions. Their valuable comments and suggestions helped me to improve my thesis. Also, my sincere thanks go to Dean Prof. Juan Meza for honoring my final year of my research with an award of "2014 Dean's distinguished scholars dissertation fellowship". I would like to acknowledge that my Ph.D study is partly supported by NSF Solar initiative under grant CHE-0934615.

I also thank all UC Merced applied mathematics faculty members for creating a welcoming academic and social environment here. Through my PhD, I made very important long lasting friends. I would like to thank my friend Nitesh Kumar for several fruitful discussions about mathematics in particular and life in general. I greatly appreciated his help and useful feedbacks about my research. Also, I would like to thank my officemate Jane HyoJin Lee for her friendship, kindness and generosity, and I would like to thank Garnet Vaz for his insightful discussions on my research. I am very grateful for going through the graduate school with them. They made my grad school life enjoyable and exciting. I am happy to have them as my friends.

In addition, I would like to thank Prof. Nalan Antar and Prof. İlkay Bakırtaş Akar who taught me and encouraged me pursuing my academic career goals. Without their encouragement, I would not have decided to go to a graduate school here. I greatly appreciated their help and kindness.

I am also grateful for the time that I spent with my kind roommate Rebecca Sweeley. I am thankful for her great support, friendship, and for being a part of my family. It was wonderful.

Last but not the least, I would like to take this opportunity to thank my close friends: Selin Taşkent, Hande Adıyaman, Ahsen Utku who have had similar experiences with the graduate school in USA. I give my special thanks to them for having enjoyable, meaningful chats with me, and for giving me full support. They have been my best cheerleaders.

VITA

1999-2004 Bachelor of Science, Mathematics, Yıldız Technical University, Istanbul, Turkey

2004 - 2007 Master of Science, Mathematics, Istanbul Technical University, Istanbul, Turkey

2009 - 2014 Doctor of Philosophy, Applied Mathematics,University of California Merced

PUBLICATIONS

- Lie group analysis of gravity currents, *Nonlinear Analysis: Real World Applications*, 11 (2), 978-994, 2010 (with N. Antar, T. Ozer)
- Theoretical-group analysis of the inviscid gravity currents, *Journal of Interdisciplinary Mathematics*, 13, 355-376, 2010 (with T. Ozer)
- Monte Carlo simulations of light scattering in luminescent solar concentrators based on semiconductor nanoparticles, *Journal of Applied Physics*, 110, 033108, 2011 (with B. Ilan and D. F. Kelley)
- Radiative transport theory for light propagation in luminescent media, *Journal of the Optical Society America A*, 30, 813, 2013 (with B. Ilan)
- Asymptotic solution of light transport problems in optically-thick luminescent media, (*submitted*) (with B. Ilan)

FIELDS OF STUDY

Major Field: Applied Mathematics

Studies in Mathematics
Professor Hakan DemirBuker

Studies in Mathematics
Professor Nalan Antar

Studies in Applied Mathematics
Professor Boaz Ilan

Modeling Light Propagation in Luminescent Media

by

Derya Şahin

University of California, Merced, 2014

Professor Boaz IIan, Chair

ABSTRACT OF THE DISSERTATION

This study presents physical, computational and analytical modeling approaches for light propagation in luminescent random media. Two different approaches are used, namely (i) a statistical approach: Monte-Carlo simulations for photon transport and (ii) a deterministic approach: radiative transport theory. Both approaches account accurately for the multiple absorption and reemission of light at different wavelengths and for anisotropic luminescence. The deterministic approach is a generalization of radiative transport theory for solving inelastic scattering problems in random media. We use the radiative transport theory to study light propagation in luminescent media. Based on this theory, we also study the optically thick medium. Using perturbation methods, a corrected diffusion approximation with asymptotically accurate boundary conditions and a boundary layer solution are derived. The accuracy and the efficacy of this approach is verified for a plane-parallel slab problem. In particular, we apply these two approaches (MC and radiative transport theory) to model light propagation in semiconductor-based luminescent solar concentrators (LSCs). The computational results for both approaches are compared with each other and found to agree. The results of this dissertation present practical and reliable techniques to use for solving forward/inverse inelastic scattering problems arising in various research areas such as optics, biomedical engineering, nuclear engineering, solar science and material science.

Chapter 1

Introduction

Radiative transport theory is a phenomenological approach for modeling the propagation, the absorption and scattering of radiation through random media using the radiative transport equation (**RTE**) [1, 2]. It has been applied successfully to many problems, such as atmospheric scattering of light, neutron scattering, and light propagation in tissue with application to medical imaging. The atmospheric science (astrophysics) was the first which initiates the theoretical foundations and analytical methods of the radiative transport theory at the beginning of the 20th century (cf. [1]). As an another application area, in nuclear physics, radiative transport theory has been extensively used to describe the neutron transports (cf. [3, 4]). Computational modeling of neutron transport was one of the first engineering applications of this theory. In parallel with the nuclear studies, radiative transport theory was studied and further developed by researchers working in the field of optics and medical imaging (cf. [2, 5]).

Most of the previous studies in these application areas, radiative transport theory is used to model **elastic** scattering media. In the elastic scattering media, the scattered radiation has the same energy as the incident one. This is a form of particle scattering where the kinetic energy is conserved ($e.g.$, nuclear physics and particle physics). When the scattered energy differs from the incident one, this corresponds to the case of inelastic scattering. For example, the neutron scattering for fission reactors is inelastic scattering (cf. [6–8]).

In this research, we focus on the application of radiative transport theory for solving inelastic scattering problem, in particular, for solving scattering problems in **luminescent** media. In luminescent media, when light is absorbed by particles and is reemitted, the reemitted wavelength (energy) differs from the absorbed one. Namely, luminescence is a form of **inelastic** scattering. This is the case, for example, for light propagation in luminescent solar concentrators (**LSCs**) and in tissue containing lumophores for luminescence optical tomography. When light propagates through such a medium, it can undergo multiple absorption and reemission, which is detrimental for most applications.

For luminescence, almost all of the previous studies have modeled the system in terms of coupled radiative transport equations for the absorption and reemission (*i.e.*, the excitation and fluorescence). This problem has been studied in the context of luminescence optical tomography (cf. [9–18]) and recently also in the context of solar energy concen-

tration (cf. [19, 20]). However, these model equations do **not** account for **reabsorption** accurately.

In this dissertation, analytical and computational techniques are studied to model light propagation through a medium that contains random luminescent scatterers. We use the statistical and deterministic approaches based on radiative transport theory. This is the first detailed study which allows the **reabsorption** effects to be accounted for. In particular, we apply this theory to model light propagation in luminescent solar concentrators. The structure of this dissertation is organized as follows.

In Chapter 3, a statistical method: **Monte-Carlo simulations** (**MC**) is used to solve light transport problem in inelastic scattering media. In general, MC simulations are a flexible yet rigorous approach to simulate "photon transport" in random media. We use this approach including luminescence in random media. In particular, the MC simulations are employed to analyze the performance of the semiconductor-based LSCs and to predict the optimal design parameters. The results of this study have been published in the Optical Society (OSA) conference proceeding [21] and the Journal of Applied Physics [22].

In Chapter 4, a novel deterministic modeling approach is studied. This deterministic approach is a generalization of the radiative transport theory including wavelength dependency for the radiation of light in luminescent media. We call the governing transport equation "**luminescent radiative transport equation**" (**LRTE**). In particular, we apply this approach to model light propagation in luminescent solar concentrators. The results of this study have been published in the SPIE conference proceeding [23] and the Journal of Optical Society America A [19].

In Chapter 5, asymptotic solutions of the LRTE are studied for optically thick media. Using asymptotic methods, a corrected diffusion approximation is derived. The diffusion approximation consists of a single partial differential equation, in which the wavelength appears as a parameter, with associated boundary conditions and a boundary layer solution. The accuracy of the diffusion approximation is verified for a plane-parallel slab problem. In particular, the reduced system captures accurately the reabsorption of light, which is an important aspect of the problem for applications. The results of this study have been submitted and under review [24].

Chapter 2

Luminescent Solar Concentrators

Solar PV cells produce direct current electricity from sunlight which can be used to power equipment or to recharge a battery. Due to the increased demand for renewable energy sources, the manufacturing of solar PV cells has advanced considerably over the past few decades. However, efficient solar PV cells are fairly expensive compared with the competing energy sources. Another limitation of using direct solar cells is that solar PV cells are inefficient for collecting diffuse sunlight.They can be addressed by using cooling and tracking mechanisms. As a result, the worldwide usage of solar PV power is still very low (see Figure 2.1).

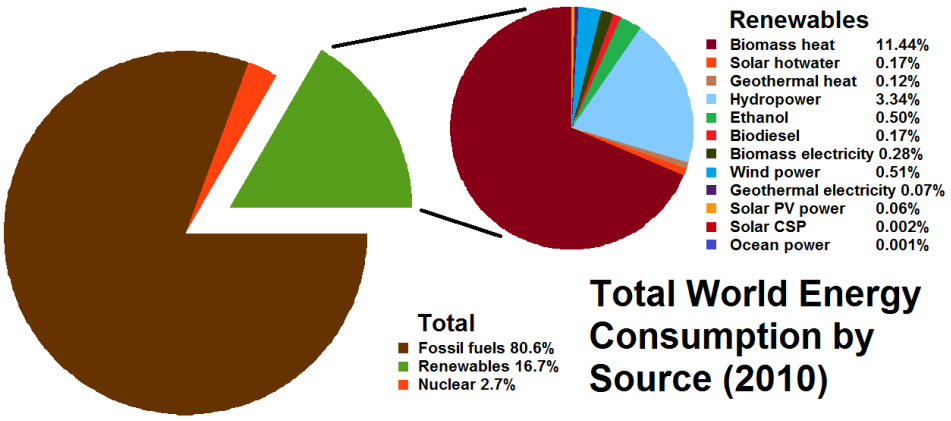

Figure 2.1: The recorded data from 2010 for total world consumption of renewable energy sources. The worldwide usage of solar photovoltaic power is 0.06% [25].

As an alternative to using direct solar PV cells, since the 1970s researchers have been developing such devices called luminescent solar concentrators (**LSCs**) [26–29].

LSCs can concentrate light onto a small scale PV cell at the edge of the device (see Figure 2.2). Incoming sunlight is collected over a large surface of a LSC and then is absorbed and reemitted by luminescent materials. The resulting luminescence is transported to the edge of the LSC sheet and concentrated onto PV cells.

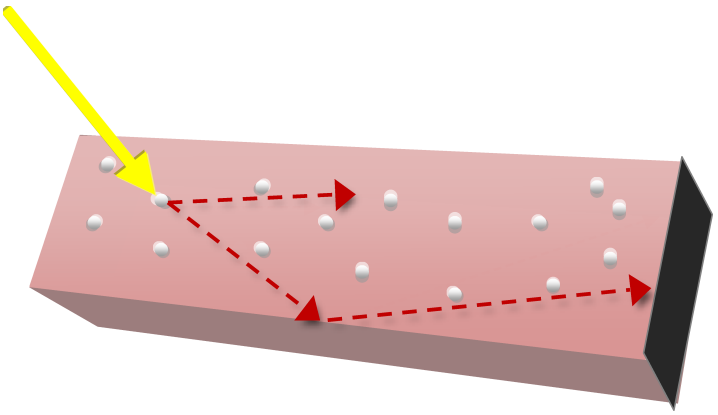

Figure 2.2: Illustration of light propagation in a luminescent solar concentrator. Sunlight (solid arrow) is incident on the top surface, absorbed and reemitted by fluorescent nanoparticles (small spheres), and guided toward the PV cell on the right edge [19].

The main idea behind the design of LSCs is to reduce operational cost substantially by requiring less amount of expensive PV material. In addition, unlike PVs, LSCs can produce highly concentrated light output under either diffuse or direct insolation [28, 30], thereby negating the need for any tracking mechanism. However, despite more than 30 years of research, LSCs are not yet commercially available, primarily due to their inefficiency (cf. [28, 31] for recent studies of LSCs).

Two major challenges are increasing the reemission of light (the photoluminescence quantum yield) while reducing the self-absorption, *i.e.*, increasing the Stokes shift between the absorption and reemission spectra (see Fig. 2.3). Another challenge is decreasing the escape of light from the top surface of the LSC. Recently, it has been proposed to use aligned nano particles in LSCs in order to reduce these losses [22, 32]. To address the self-absorption (reabsorption) loss, most current LSCs rely on luminescent small-molecule dyes or organic polymer dyes (cf. [33–35]), whose performance has been considerably improved over the past two decades. A more recent approach is using semiconductors nanoparticles, thus far mostly of "type-I" (commonly based on CdSe or PbSe) [36–39]. Unfortunately, neither approach has yielded LSCs that are efficient enough to be cost effective. Both approaches suffer from the same fundamental limitation: to absorb more sunlight the concentration of the active media needs to be high, but with higher concentration the luminescence is more likely to be reabsorbed. The performance of the LSC is then limited by the losses incurred by reabsorption / reemission events [29].

2.1 Semiconductor-based Luminescent Solar Concentrators

In this study, we focus on computational modeling of LSCs based on "type-II" semiconductor CdSe-CdTe nanoparticles, *i.e.*, quantum dots and nanorods [40–42]. The computational results show that these semiconductor-based LSCs can be significantly more efficient and cost effective compared with current LSCs. CdSe-CdTe nanoparticles have two main advantages (see Figure 2.3),

(i) A wider absorption band at shorter wavelengths,

(ii) A smaller reabsorption probability, making them less prone to losses due to multiple absorption-remission events.

In addition, the photoluminescence quantum yield of CdSe-type **quantum dots** can be quite high (see [22] for quantum yields above 90%), while overcoating such quantum dots with a larger bandgap semiconductor has been shown to greatly increase the stability for use in LSCs [38].

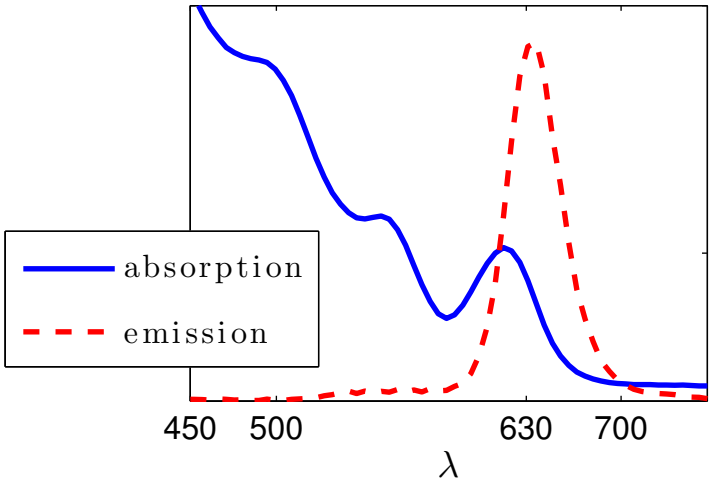

Figure 2.3: This figure shows the absorption spectra for CdSe/Te nano-particles (measured by D. Kelley's group at UC Merced) [22].

Besides the choice of particles, LSCs have several design parameters that can affect their performance such as the particle concentration the optimal LSC geometry. The escape of light from the top surface is a significant loss mechanism in LSCs. To address the escape loss, we explore the use of CdSe-CdTe **nanorods** that are aligned perpendicular to the top surface. This design induces anisotropic luminescence with a preferred direction, that reduces the escape of light from the LSC (see Figure 2.4).

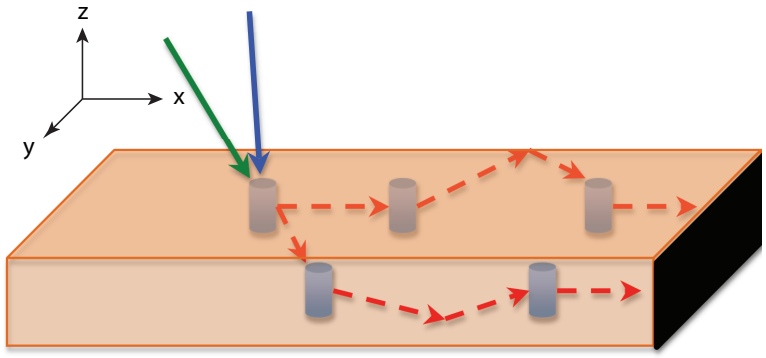

Figure 2.4: llustration of light propagation in a 3D LSC based on anisotropic nanorods. A PV cell is located at the right edge. Perfect mirrors are assumed to cover the bottom surface and all the other edges [19].

Chapter 3

Monte Carlo Simulations for Photon Transport

Monte Carlo (**MC**) method is a technique first proposed by [43] using a stochastic model, which has been applied to many problems in scattering theory and also other fields (Finance, Biology etc.). In scattering theory, MC is used to simulate physical processes in random media. In particular, for light scattering, this method is called as "photon transport". MC allows calculation of reflection, transmission, fluence rates in the medium. This method is a flexible tool to use when phase-dependent wave effects, such as interference and diffraction, are negligible (cf. [4]). It is a powerful technique because of the ability to incorporate multi-physics phenomena.

Computational Modeling

MC has been applied to various fields such as astrophysics, optical tomography, biomedical imaging etc. (cf. [5, 44]). Recently, it has been applied to the field of LSCs [22, 29, 32, 37]. In this study, MC simulations are used to compute the performance of LSCs based on semiconductor nanoparticles. We seek optimal design parameters such as particle concentration, the size of LSC etc. In addition, we analyze anisotropy affects on the performance of a LSC based on aligned nanorods. MC is particularly efficacious for light propagation in LSCs, because of the flexibility to model the multi-physics phenomena that take place, *i.e.*, absorption and emission over a broad spectrum, reflection and transmission at the LSC boundaries, and collection at the PV cell.

3.1 Design and Implementation

We consider a rectangular box-shaped LSC with dimensions $|x| \leq l_x/2$ (length l_x), $|y| \leq l_y/2$ (width l_y), and $|z| \leq l_z/2$ (thickness l_z). A PV cell is assumed to cover the right $y-z$ edge, i.e. $x = +l_x/2$. Perfect mirrors are assumed to cover the bottom surface ($z = -l_z/2$) and on all the other edges. Therefore, light can only escape from the top surface (see Figure

3.1).

A photon is launched into the LSC and tracked until it is either lost due to radiation effects (not absorbed or not reemitted), escapes from the LSC, or reaches the PV cell at the edge, where it is collected (counted).

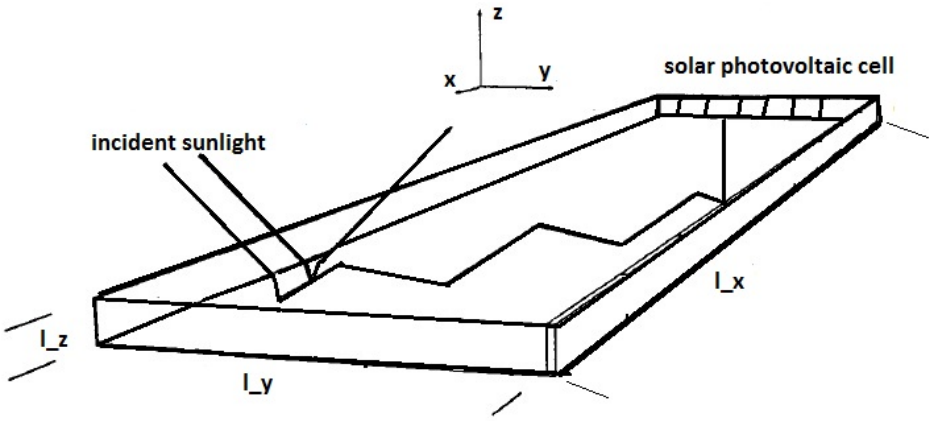

Figure 3.1: Illustration of a rectangular box-shaped LSC, where the PV cell is located at the single edge and the bottom surface and other sides are covered by mirrors. Sunlight is incident on the LSC's top surface and guided on to the PV cell.

To obtain statistically reliable results, at least 10^6 photons are used for each incident wavelength and LSC parameters (particle concentration, LSC size, etc.). The algorithm is discussed below in detail (see Figure 3.2)

3.1.1 Absorption and emission

In general, the probability of a photon being absorbed after propagating a distance Δs (in cm) is given by the Beer-Lambert law [45],

$$p(\Delta s; \lambda) = 1 - 10^{-\epsilon(\lambda) M \Delta s} \, , \tag{3.1}$$

where M is the molar concentration of the particles (in $^{\mathrm{mol}}/_{\mathrm{L}}$) and $\epsilon(\lambda)$ is the extinction coefficient (in $^{\mathrm{L}}/_{\mathrm{mol\ cm}}$), which we obtain from the measured absorption spectrum (see Figure 2.3).

Initially, a photon is launched at the center of the LSC's top surface at normal angle (see also Section 3.5 for extensions), with a wavelength λ that is sampled randomly from the absorption spectrum. If the photon is not absorbed within a distance

$$\Delta s_0 = l_z \, , \tag{3.2}$$

where l_z is the LSC height, the photon is assumed to bounce from the bottom mirror at

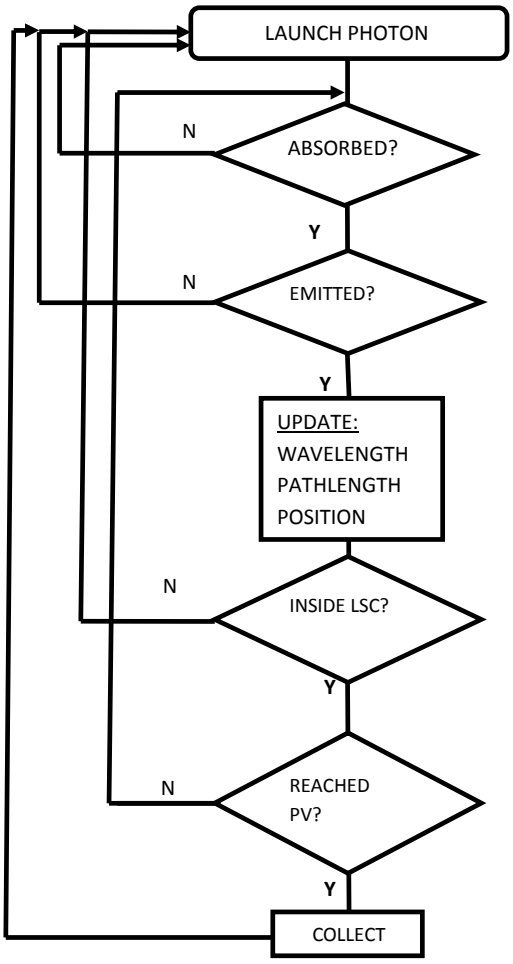

Figure 3.2: Schematic representation of the MC algorithm.

normal angle and then escape from the top surface (see Section 3.1.2). In that case, the simulation resumes with a new photon. For subsequent remission events a random path-length is chosen by "solving" (3.1) to get

$$\Delta s = -\frac{1}{\epsilon(\lambda)M}\log_{10}\xi\ , \tag{3.3}$$

where, here and in what follows, ξ denotes a random variable that is uniformly distributed in $[0,1]$.

If the photon is absorbed, it is reemitted only if

$$\xi < \mathrm{QY}\ , \tag{3.4}$$

where QY, the quantum yield, is the measured ratio of reemitted to absorbed photons.

If the photon is reemitted, its wavelength, position and direction are updated as follows. The photon's new wavelength is sampled randomly from the normalized emission spectrum, as if the luminescence were memoryless. We note that for semiconductor particles, the assumption of completely memoryless luminescence overestimates the reabsorption losses from the second event. This is because when photons are (re)absorbed at the red edge of the absorption spectrum, they will more likely be reemitted further to the red due to inhomogeneous broadening, in which case they are less likely be reabsorbed again.

The photon's new position (x', y', z') is updated based on its incident direction as

$$\begin{aligned} x' &= x + \mu_x \Delta s, \\ y' &= y + \mu_y \Delta s, \\ z' &= z + \mu_z \Delta s\ , \end{aligned} \tag{3.5}$$

where (μ_x, μ_y, μ_z) are the direction cosines and Δs is given by (3.3). The direction cosines themselves are updated in two-step process. For isotropic QDs, the new azimuthal angle and cosine of the deflection angle are obtained using

$$\varphi = 2\pi\xi \tag{3.6}$$

and

$$\cos\theta = \mathrm{sign}(\chi) - \chi, \quad \chi \equiv 2\xi - 1\ , \tag{3.7}$$

so that $\phi \in [0, 2\pi)$, $\theta \in (0, \pi)$, and the reemitted light is distributed isotropically. Us-

ing (3.6)–(3.7) the direction cosines are then updated according to

$$\begin{aligned}\mu_x' &= \frac{\sin\theta}{\sqrt{1-\mu_z^2}}\left(\mu_x\mu_z\cos\varphi - \mu_y\sin\varphi\right) \\ &\quad + \mu_x\cos\theta \qquad (3.8a)\\ \mu_y' &= \frac{\sin\theta}{\sqrt{1-\mu_z^2}}\left(\mu_y\mu_z\cos\varphi + \mu_x\sin\varphi\right) \\ &\quad + \mu_y\cos\theta\,, \qquad (3.8b)\\ \mu_z' &= -\sin\theta\cos\varphi\sqrt{1-\mu_z^2} \;+\; \mu_z\cos\theta\,. \qquad (3.8c)\end{aligned}$$

Equations (5.29) correspond to luminescence at deflection angles (θ, φ) with respect to the incident radiation [44]. If the incident direction is almost normal to the (x, y) plane, i.e. $|\mu_z| > 0.99999$, the direction cosines are updated using the asymptotic formulae for $|\mu_z| \to 1$, which are

$$\mu_x' = \sin\theta\cos\varphi\,, \qquad (3.9a)$$

$$\mu_y' = \sin\theta\sin\varphi\,, \qquad (3.9b)$$

$$\mu_z' = \mathrm{sign}(\mu_z)\cos\theta\,. \qquad (3.9c)$$

See Eqs. (3.16) and (3.17) for the case of anisotropic luminescence.

3.1.2 LSC size and boundary conditions

LSCs are designed to reflect most of the light back from the top surface by using a medium with an index of refraction greater than 1. We assume $n_{\mathrm{LSC}} = 1.7$, which allows for total internal reflection whenever $\mu_z < \mu_{\mathrm{cr}} = \sin^{-1}(1/1.7) \approx 0.81$ (i.e. light is reflected when the incident angle is greater than 36° with respect to the zenith). When $\mu_z > \mu_{\mathrm{cr}}$ the photon is assumed to reflect if

$$\xi < R(\beta)\,, \quad \beta \equiv \cos^{-1}(\mu_z)\,,$$

where $R(\beta)$ is the Fresnel reflection coefficient for unpolarized light [46]. Otherwise, the photon escapes from the LSC.

When a photon arrives at the PV cell it is assumed to be collected. In reality, PV cells have a bandgap for efficient conversion of light into electricity. In this regard, our computations yield an upper bound on the optical efficiency of the LSC [see Eq. (3.10)]. Nevertheless, these particles have a narrow emission band that falls well within the typical bandgap of PV cells.

3.1.3 Solar-averaged optical efficiency and LSC gain

A common metric for LSC performance is the *optical efficiency*, $\eta(\lambda)$, defined as the ratio of incident photons at wavelength λ to the collected photons (at any wavelength). A more

relevant metric for LSC performance is the *solar-averaged optical efficiency*,

$$\overline{\eta} \;=\; \frac{\int_{\lambda_{\min}}^{\lambda_{\max}} N_{\text{solar}}(\lambda)\eta(\lambda)d\lambda}{\int_{\lambda_{\min}}^{\lambda_{\max}} N_{\text{solar}}(\lambda)d\lambda}\,, \quad N_{\text{solar}}(\lambda) \doteq \frac{I_{\text{solar}}(\lambda)}{\lambda}\,, \tag{3.10}$$

where $I_{\text{solar}}(\lambda)$ is the solar irradiance at sea level and $N_{\text{solar}}(\lambda)$ is proportional to the number of photons per area per wavelength. We obtain $I_{\text{solar}}(\lambda)$ from [47] and use $\lambda_{\min} = 400\,\text{nm}$ and $\lambda_{\max} = 750\,\text{nm}$. Thus, $\overline{\eta}$ is a measure of the ratio between the total photons collected by the PV cell and the total photons incident on the LSC.

The solar-averaged optical efficiency is an adequate metric of the LSC performance when the LSC dimensions are fixed. However, a more useful metric is the *LSC gain*,

$$\Gamma(\lambda) \;=\; \eta(\lambda) \times G\,, \tag{3.11}$$

and the *solar-averaged LSC gain*,

$$\overline{\Gamma} \;=\; \overline{\eta} \times G\,, \tag{3.12}$$

where G, the geometric factor, is the ratio of the area directly exposed to sunlight (the top surface area) to the area covered by the PV cell, i.e.

$$G \equiv \frac{A_{\text{top}}}{A_{\text{PV}}}\,. \tag{3.13}$$

See Section 3.3 for further details. The advantage of using the LSC gain is twofold:

1. The gain $\overline{\Gamma}$ measures the ratio of collected photons using the LSC compared with exposing the (same) PV cell directly at the sun. As such, it must be (substantially) greater than 1 in order for the LSC to be cost-effective.

2. Unlike $\overline{\eta}$, which generally decreases with the LSC size, $\overline{\Gamma}$ attains its maximum value at some finite dimensions (see Figure 3.7). This is useful for finding the optimal LSC dimensions.

We note that $\overline{\Gamma}$ serves as a *lower bound* on the actual gain, because the LSC can also capture diffuse light and also converts light into the PV bandgap.

3.2 Optimal particle concentration

A photon can undergo multiple absorption and and reemission events inside the LSC. The quantum yield, QY, is a measure of emitted to absorbed photons. Light that is not reemitted is typically lost. For these CdSe-CdTe QDs, QY=95%. However, the probability of reemission diminishes quickly with the number of reabsorption-reemission events. Therefore, under ideal conditions, most photons should be absorbed and remitted once before being collected by the PV. Whether this happens depends on the particle concentration, M, in a

complex way. The value of M that will maximize $\eta(\lambda)$ varies with λ. We are therefore interested in the optimal concentration that yields the maximum of $\overline{\eta}$ [Eq. (3.10)].

Since the probability of absorption increases with the particle concentration [see Eq. (3.1)], the concentration should not be too high. On the other hand, the concentration should not be too low, lest the photons will not be absorbed at all. Hence, the optimal concentration must strike a balance between these competing loss mechanisms. However, there is more to the story, since the probability of reabsorption depends on the overlap between the absorption and emission spectra. In this regard, the small reabsorption of semiconductor nanoparticles is a key advantage. Therefore, by using semiconductor particles a higher concentration can be chosen while keeping the the reabsorption losses small.

To find the optimal concentration we fix the LSC dimensions as $l_x \times l_y \times l_z = 6\,\mathrm{cm} \times 2\,\mathrm{cm} \times 0.4\,\mathrm{cm}$ and vary M between 10^{-8} and 10^{-5} mol/L. The maximum solar-averaged optical efficiency is

$$\overline{\eta}_{\max} \equiv \max_{M} (\overline{\eta}) \approx 24\% \,,$$

which is achieved at $M = M_\star \approx 4.3 \times 10^{-6}$ mol/L (see Figure 3.3).

Figure 3.3 also shows that, if considering light incident at a particular wavelength, the optimal concentration generally increases somewhat with longer incident wavelengths. This is expected as $\epsilon(\lambda)$ mostly decreases with λ. The optimal concentration is also approximately the same as would be obtained using $\lambda = 630\,\mathrm{nm}$ alone (see also Figure 3.6).

Figure 3.4 shows the breakdown of the (statistically averaged) loss mechanisms and their dependence on particle concentration. As M increases, more photons are initially absorbed in the LSC. At the same time, more photons are lost either due to not being reemitted (i.e. not emitted or not reabsorbed in the first or subsequent luminescence events) or due to escaping from the top surface. At the optimum, approximately 57% of the incident photons are not absorbed, the emission / reabsorption losses are 8.5%, and the escape loss is 12%.

Figure 3.5 shows that the collected spectrum is slightly shifted to the red compared with the single-emission spectrum. This tiny Stokes shift is due to the reabsorption, which peaks around $630\,\mathrm{nm}$. To analyze this further, Figure 3.6 shows that the reabsorption and escape losses have a local peak around $630\,\mathrm{nm}$, as does the initial absorption (i.e. the not-absorbed curve has a dimple). As mentioned above, at $M = M_\star$ the solar-averaged efficiency $\overline{\eta}_{\max}$ is also about the same as $\eta(630\,\mathrm{nm})$. Thus, the maximum solar-averaged efficiency $\overline{\eta}_{\max}$ is achieved by balancing the competing loss mechanisms over the visible spectrum.

3.3 Optimal LSC size

Thus far, the results were for fixed LSC size and assuming a PV cell that covers the right $y - z$ edge. It is interesting to study how the LSC performance changes with size and location of the PV cell. In general, as the area of the top surface of the LSC increases, more light enters the medium, but has a greater chance of being lost due to reabsorption or escape. The question arises as to *what are the optimal LSC dimensions?* To address this,

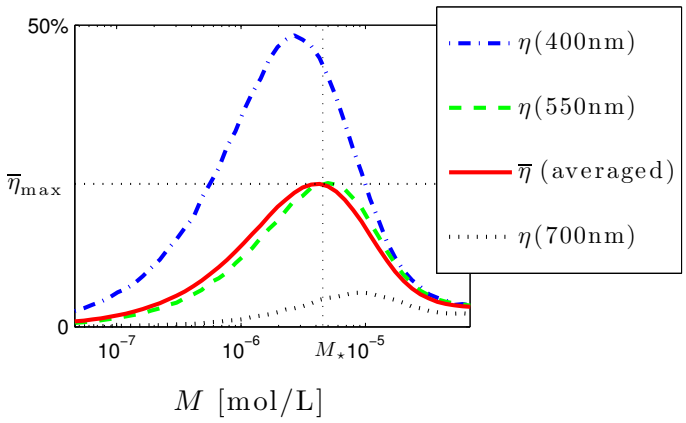

Figure 3.3: Solar-averaged optical efficiency $\overline{\eta}$ (solid) and the wavelength-dependent optical efficiency for three different incident wavelengths (see legend) as functions the quantum-dot concentration (log scale). A maximum optical efficiency of $\overline{\eta}_{\max} = 23.67\%$ is reached at $M_\star = 4.3 \times 10^{-6\,\text{mol}/\text{L}}$.

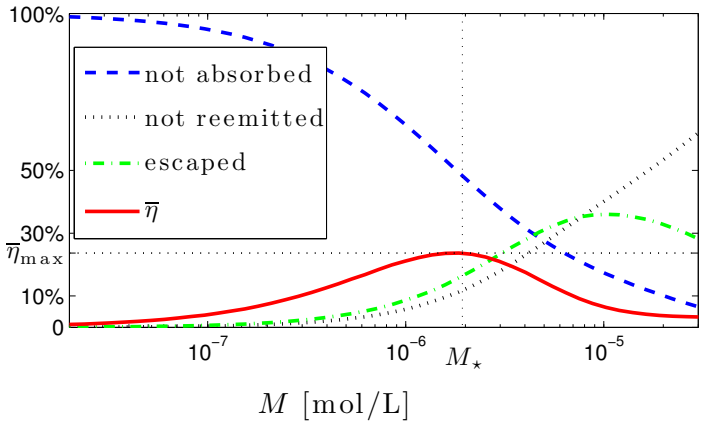

Figure 3.4: Dependence of the solar-averaged optical efficiency $\overline{\eta}$ (solid), initially not absorbed photons (dashes), emission / reabsorption losses (dots), and escape from the top surface (dash-dots) on particle concentration.

the LSC gain [Eqs. (3.11) and(3.12)] serves as the most relevant performance metric.

We first assume (as above) that the PV cell covers the *single edge*, i.e. the right $y-z$ edge ($x = +l_x$). The *single-edge geometric gain factor* (3.13) is

$$G_{\text{single}} = \frac{A_{\text{top}}}{A_{\text{PV}}} = \frac{l_x l_y}{l_y l_z} = \frac{l_x}{l_z} \,. \tag{3.14}$$

We fix $l_y = 2\,\text{cm}$ and $l_z = 0.4\,\text{cm}$ and vary the LSC length, l_x. Therefore, the area covered

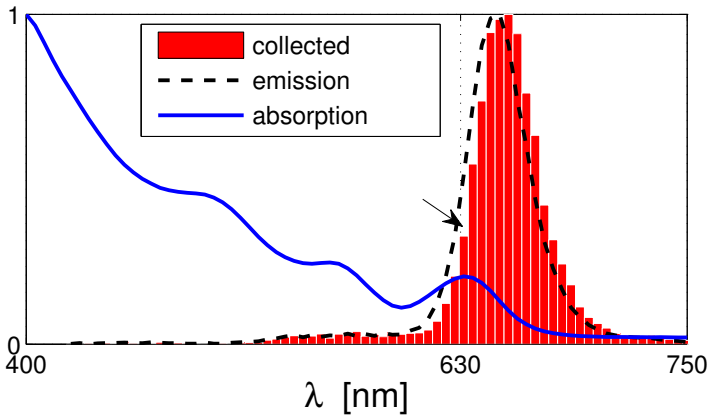

Figure 3.5: Same as Figure 2.3 with the addition of the collected spectrum at the PV cell using $M = M_\star$ (see Figure 3.3). The arrow indicates a small Stokes shift ($\approx 5\,\mathrm{nm}$) between the emission spectrum of the QDs (dashes) and collected spectrum (histogram).

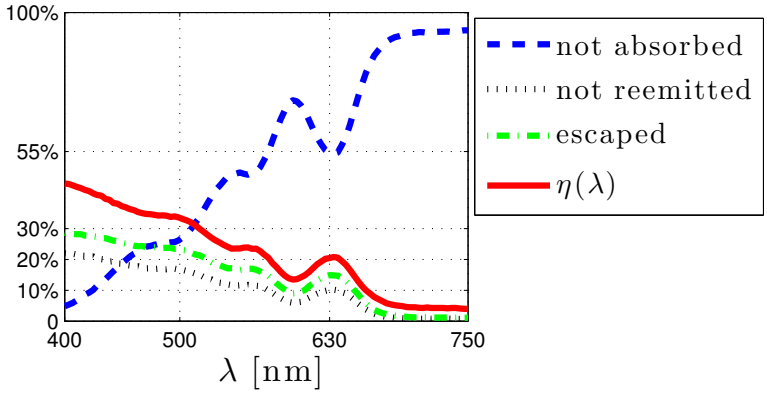

Figure 3.6: Same as in Figure 3.4 showing the dependence of $\eta(\lambda)$ and the loss mechanisms on the incident wavelength λ with $M = M_\star$.

by the PV cell remains constant, while the top surface area increases. Our computations show that the optimal LSC dimensions depend only weakly on the particle concentration and incident wavelength. For this reason, we initially fix $M = 4.3 \times 10^{-6\,\mathrm{mol}/\mathrm{L}}$ ($M_\star$ found above for $l_x = 6\,\mathrm{cm}, G_{\mathrm{single}} = 15$) and use incident light at $\lambda = 630\,\mathrm{nm}$. Figure 3.7 present the results. As the length l_x increases the optical efficiency decreases. This is not surprising, as a smaller fraction of the total incident photons arrives at the edge covered by the PV cell due to reabsorption and escape losses. What is perhaps more relevant is that the LSC gain peaks at $\overline{\Gamma} = 4$ when $G_{\mathrm{single}} = 26$, which corresponds to $l_x/l_y = 5.2, l_x = 10.4\,\mathrm{cm}$. Hence, the optimum performance is reached with a fairly long LSC box. This is also evident from Table 3.1. Indeed, at the optimal LSC size ($G_{\mathrm{single}} = 26$), the solar averaged efficiency is $\overline{\eta} = 13\%$, which is somewhat lower than 23.67% obtained using $G_{\mathrm{single}} = 15$, yet the gain

is a bit larger. Moreover, if a square LSC were to be used ($l_x = l_y = 2, G_{\text{single}} = 5$), then $\overline{\eta} \approx 37\%$ becomes even higher, but the gain would reduce by more than half compared with the optimum.

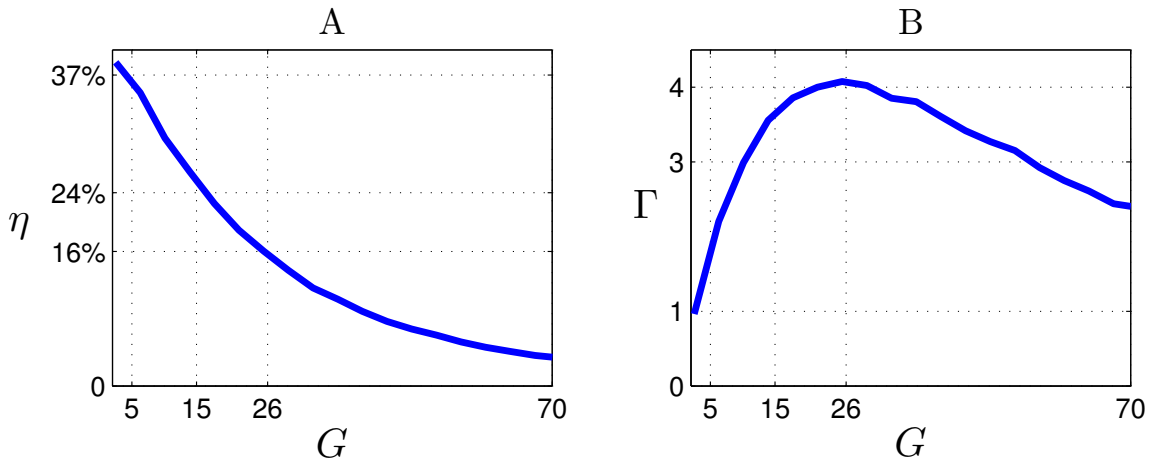

Figure 3.7: Optical efficiency η (A) and LSC gain Γ (B) at $630\,\text{nm}$ as functions of the single-edge geometric factor (3.14).

Table 3.1: Gain and loss characteristics using QDs for different LSC dimensions, when the PV cell covers the edge $x = l_x/2$.

G_{single}	l_x/l_y	not absorbed	not reemitted	escaped	$\overline{\eta}$	$\overline{\Gamma}$
5	1	48%	7%	8%	37%	1.85
15	3	49%	14%	13%	24%	3.2
26	5.2	48%	15%	21%	16%	4

A related question is whether it is better to cover *all the LSC edges* with PV cells, i.e. on $|x| = l_x$ and $|y| = l_y$. Due to symmetry considerations, the optimal dimensions are achieved using a square LSC, $l_x = l_y$. At first thought, covering all the edges with PV cells might seem like a good idea because light has to travel a shorter distance to reach a PV cell, thereby reducing the reabsorption and escape losses. However, since in this case, $A_{\text{PV}} = 2(l_x + l_y) = 4l_x$, the *all-edges geometric gain factor* is only

$$G_{\text{all}} = \frac{l_x}{4l_z} = \frac{1}{4} \times G_{\text{single}} \,. \tag{3.15}$$

In fact, our computations show that when all the LSC edges are covered with PV cells, $\overline{\Gamma}_{\text{max}}$ is only marginally greater than 1 (see Table 3.2). In this vain, we remark that, under the condition of optimal particle concentration, most photons are absorbed and reemitted only once, an advantage due to the small reabsorption cross-section of these QDs. The

Table 3.2: Same as Table 3.1 when the PV cells cover all the edges of a square LSC.

$G_{\rm all}$	$l_x = l_y$	not absorbed	not reemitted	escaped	$\overline{\eta}$	$\overline{\Gamma}$
5.4	8.6	48.4%	12.1%	16.2%	23.3%	1.25
7.3	11.7	48.3%	14.1%	19.07%	18.53%	1.35
15	24	48.5%	18.2%	25.2%	8.1%	1.21

reemitted light rays bounce back and forth, impinging on the top surface at the same (or more grazing and hence more reflecting) angle each time, until they reach the edge covered by a PV cell. Indeed, as the geometric factor increases, the fraction of light flux that is not reemitted or escapes grows at a much slower rate (see as Tables 3.1 and 3.2). Taking into account the cost of the extra PV material needed compared with a single-edge PV cell, we conclude that a single-edge PV cell is a much more cost-effective design.

3.4 Anisotropic luminescence

As shown in Table 3.1, under optimal conditions almost 20% of the light escapes from the LSC. While this can be mitigated using special coatings and filters [cf. [48, 49]], the escape of light from the LSC remains a significant loss mechanism. In order to ameliorate this, we investigate using *aligned semiconductor nanorods*, i.e. rod-shaped CdSe-CdTe nanoparticles that are aligned in the LSC with their long axis perpendicular to the top surface (see Figure 2.4 in Section 2). This induces anisotropic luminescence that peaks in the plane parallel to the top surface, thus reducing the escape of light from the LSC. Similar approaches have been studied recently for dye-based LSCs [32, 50–53].

One of the advantages of semiconductor nanorods compared with dyes is that, when semiconductor nanorods are aligned and cannot rotate, their luminescence is polarized, while their absorption is approximately isotropic [54–56]. This is due to their electronic structure. Specifically, for single-material nanorods (CdSe or CdTe), the transition from the top of the valence band to the bottom of the conduction band is polarized along the long axis of the nanorods. However, at higher energies, there is a high density of transitions that are polarized both along and normal to the nanorod axis. The net effect is that, except at the red edge of the spectrum, the absorption is approximately isotropic. The same is true of CdSe/CdTe nanorods that form a type-II heterojunction [57–59]. In that case, the luminescence is from a charge transfer transition, which is also polarized along the nanorod long axis.

For aligned nanorods we assume isotropic absorption. However, instead of using (5.29), the direction of the reemitted photon is given by

$$\mu_x' = \sin\theta\cos\varphi, \quad \mu_y' = \sin\theta\sin\varphi, \quad \mu_z' = \cos\theta\,, \tag{3.16}$$

where, in this case, $\theta \in [0, \pi)$ is the *absolute luminescence angle* with respect to the zenith. To compute θ we use the inverted the Henyey-Greenstein formula for anisotropic lumines-

cence [44]

$$\begin{aligned} \cos\theta &= \text{sign}(\chi) - \chi\,, \\ \chi &\equiv \frac{1}{2g}\left[1+g^2-\left(\frac{1-g^2}{1+2g\xi-g^2}\right)^2\right]\,, \end{aligned} \tag{3.17}$$

where g the anisotropy coefficient. The limit $g \to 0$ gives isotropic luminescence. When $g = 1$, Eq. (3.17) gives $\theta = \pi/2$, which corresponds to luminescence only in the plane parallel to the top surface. Any other value of $0 < g < 1$ corresponds to conical luminescence relative to the (x, y) plane.

Fixing the LSC dimensions with $l_x = 6\,\text{cm}$, $l_y = 2\,\text{cm}$, $l_z = 0.4\,\text{cm}$, using $\lambda = 630\,\text{nm}$and $M = 5.8 \times 10^{-6}\ \text{mol}/\text{L}$ (see below), we compute the optical efficiency and LSC gain as function of the anisotropy g. Figure 3.9 shows that the LSC performance increases monotonically with g. For $g \approx 1$, with aligned nanorods, the LSC gain is more than 70% higher compared with using isotropic QDs.

For comparison, we also consider *forward conical luminescence* (see Figure 3.8). This would be the case, for example, for spherical quantum dots or anisotropic nanorods that are randomly oriented in the LSC. In the latter case, the luminescence would peak in the same direction as the absorbed light, but since the particles are randomly aligned, on average their luminescence would be in a random direction. To model this computationally, we revert to (5.29), but with the cosine of the *deflection angle* (with respect to the incident direction of light) given by (3.17). Figure 3.9 shows that, not surprisingly, the results are almost the same as using isotropic QDs. Hence, achieving well-aligned nanorods is important.

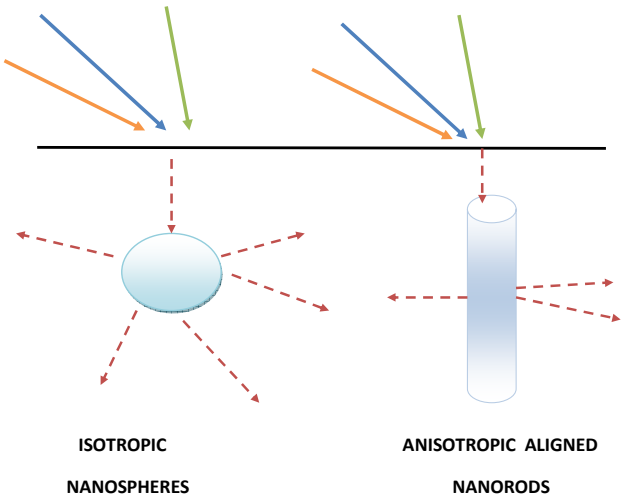

Figure 3.8: Illustration of forward luminescence by spherical quantum dots and anisotropic luminescence by aligned nanorods.

Figure 3.10 shows the loss mechanisms using aligned nanorods with $g = 0.95$. Comparing with Figure 3.4, the most significant difference is that almost no light escapes from the LSC. Consequently, the optimal particle concentration is somewhat higher than for isotopic QDs.

Table 3.3 presents a comparison of the LSC performance metrics using aligned nanorods with $g = 0.95$ for different LSC dimensions for the same l_y and l_z used for Table 3.1 and the PV on a single edge. Once again, the optimal dimensions are approximately $l_x : l_y = 5 : 1$. However, in this case, the maximal solar-averaged gain is 7.6.

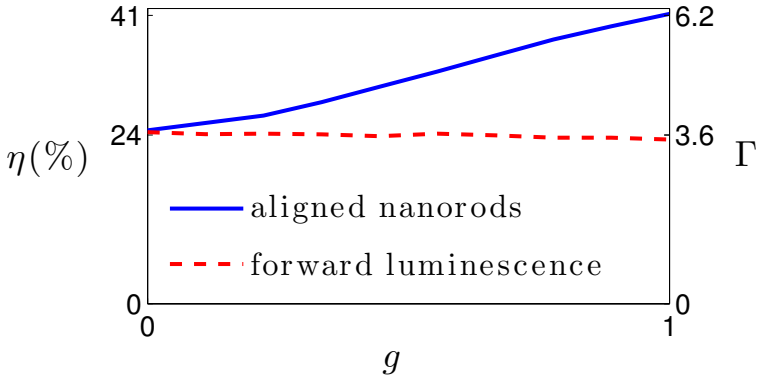

Figure 3.9: Optical efficiency (left axis) and LSC gain (right axis) for $\lambda = 630\,\mathrm{nm}$ based on anisotropic luminescence of aligned nanorods (solid) vs. forward luminescence (dashes) as functions of the anisotropy parameter g [Eq. (3.17)].

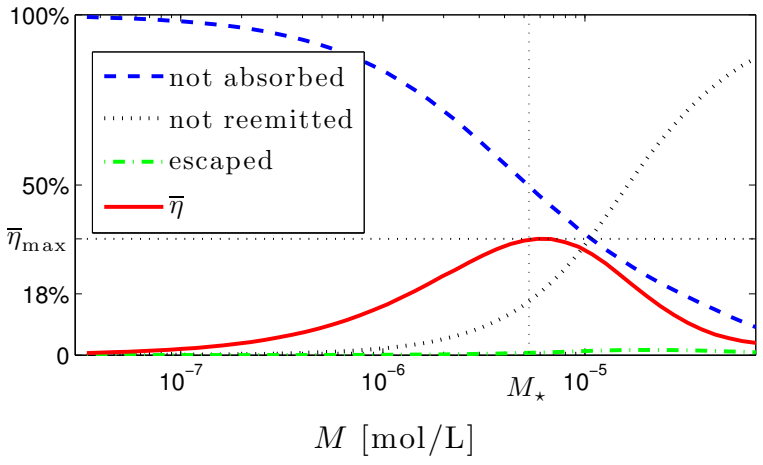

Figure 3.10: Same as Figure 3.4 using aligned nanorods with $g = 0.95$.

Table 3.3: Same as Table 3.1 for LSCs with aligned nanorods and $g = 0.95$.

G	l_x/l_y	not absorbed	not reemitted	escaped	$\overline{\eta}$	$\overline{\Gamma}$
5	1	54.4%	5.9 %	0.2%	39.5%	1.97
15	3	37.5%	21.3%	0.9%	40.3%	6
25	5	47%	24%	1.1%	27.9%	7.6

3.5 Spatial and angular distributions of the incident light

The results above assumed that light is incident at the center of the top surface, at normal angle to the surface, and is transmitted into the LSC with probability 1. In this section we study the dependence of the gain on the spatial and angular distribution of the incident light.

In general, light incident closer to the edge covered by the PV cell has a greater collection probability and light that is incident on the opposite edge has a smaller collection probability. This is demonstrated in Figure 3.11, where the PV cell is at $x_0 = l_x/2 = 5$. This figure shows that light that is incident on the opposite edge ($x_0 = -5$) has almost the same chance of collection as light incident at the center of the top surface ($x_0 = 0$). This is because: *(i)* the reemitted light has a fairly small chance of being reabsorbed, and *(ii)* if the reemitted light reflects from the top surface (back into the LSC) once, it is very likely to reflect in all the subsequent scatterings from the top surface. Since sunlight impinges on the LSC surface with an almost spatially uniform radiant intensity, the results obtained in previous sections by assuming that light is incident at the center of the top surface yield a *lower bound* on the LSC performance.

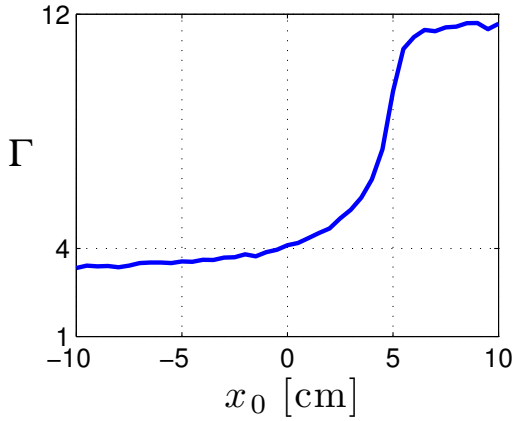

Figure 3.11: Dependence of gain on the location of the incident light along the length of the LSC. The PV cell covers the $y - z$ edge at $x = 5$.

Figure 3.12A shows the dependence of the Fresnel transmission coefficient for light incident on the top surface as a function of the angle of incidence (with respect to the

zenith). For angles below 1 rad, almost all the light is transmitted into the LSC. Figure 3.12B shows the dependence of the gain on the angle of incidence, taking into account the transmission coefficient and generalizing (3.2) to include the transmission angle as

$$\Delta s_0 = \frac{l_z}{\cos(\alpha_t)} \,, \tag{3.18}$$

where α_i and α_t are related via Snell's Law. Equation (3.18) implies that light travels a greater distance initially as the incident angle increases (becomes more grazing), thereby decreasing the initial losses due to escape. Furthermore, Figure 3.12 B shows that, for light that is incident in a cone with a opening half-angle of 1 rad from the zenith, the gain is approximately the same as at normal incidence ($\alpha_i = 0$). Since most of the diurnal irradiance falls within this cone, the results obtained in previous sections by assuming that the light is incident at a normal angle to the surface yield a very good approximation of the diurnal LSC performance.

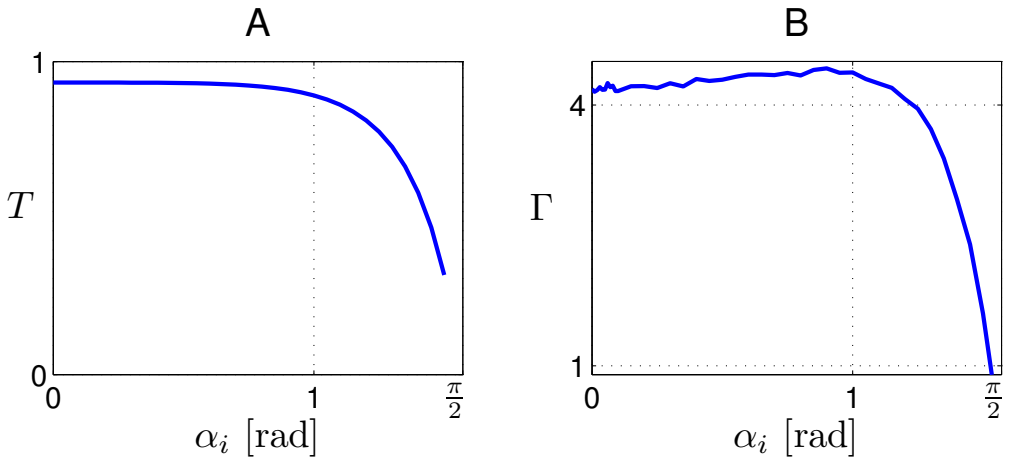

Figure 3.12: Transmission coefficient (A) and gain (B) as functions of the incident angle.

3.6 Summary and Discussions

We employ Monte Carlo method to simulate the photon transport in semiconductor-based luminescent solar concentrators. Using various statistical scenarios, each photon's movement is being tracked till either it is lost or collected by PV. In the computations, the luminescence and reabsorption features of the medium are included. This differentiates our MC approach from the ones used for (elastic) scattering problems (cf. [5, 44]). The computations are found to be consistent with physics. Even though, the convergence rate of MC is very slow, because of its flexibility it is a desirable technique for the multi-physics and inelastic scattering problems. In particular, the MC approach is applied to compute the LSC

performance metrics by using the measured data of semiconductor (CdSe-CdTe) nano particles. The results of the computations in this study suggest that LSCs based on CdSe-CdTe quantum dots (*i.e.*, isotropic nanospheres) can be more efficient than current LSC designs. Moreover, using aligned nanorods can increase the LSC performance by 70% compared with using quantum dots. We find the maximal LSC gain of 7.6 (Table 3.3). This implies that LSCs can be that much more efficient compared with exposing the PV cell directly at the sun and even more so, since LSCs can collect diffuse light as well. These theoretical findings are encouraging for further research into LSCs.

Chapter 4

Radiative Transport Theory

Radiative transport theory (also called radiative transfer) describes the wave propagation through a medium characterized by a random distribution of scatterers. Radiative transfer has been extensively used to deal with radiation, absorption and multiple scattering problems ([1–4]). Radiative transfer is commonly used to model **elastic** scattering, *i.e.*, when the scattered energy is the same as the incident one. In contrast, **inelastic** scattering means that energy is not conserved. In nuclear engineering radiative transfer has been applied extensively to model the inelastic scattering of massive particles (cf. [8, 60]). However, there have been few studies of inelastic scattering of light. This is the case of light scattering in luminescent media: the reemitted wavelength is typically longer than the absorbed one. Therefore, whereas the flux can be conserved, the energy decreases.

Almost all of the previous studies have modeled the system in terms of **coupled radiative transport equations for the absorption and reemission** (*i.e.*, the excitation and fluorescence). This problem has been studied in the context of luminescence optical tomography (cf. [9–18]) and recently also in the context of solar energy concentration (cf. [19, 20]).

Analytical & Computational Modeling

In [19], we developed a radiative transport theory for light propagation in luminescent media based on a **single radiative transport equation that takes both absorption and reemission into account.** We call the governing equation the luminescent radiative transport equation (LRTE). Particularly, in our study this theory is applied to model light propagation in LSCs. One advantage of this approach is that it uses measurable optical properties and physical parameters. The measured data enter as parameters in the LRTE. We use the LRTE approach to find the optimal particle concentration and the optimal LSC geometry, for LSCs based on these semiconductor nanoparticles. Direct computations of the solutions of the LRTE are performed in two spatial dimensions using the source-iteration method (cf. [4]). We compare the results of the LRTE with MC simulations. The two approaches (MC and LRTE) are found to agree. In particular, they yield comparable optimal particle concentrations for LSC performance. These results show the accuracy and

feasibility of the approach based on the deterministic LRTE. Another advantage of this methodology is that, as a deterministic equation, the LRTE lends itself naturally to detailed analytic modeling (see Chapter 5).

4.1 Luminescent radiative transport theory

The theory of radiative transfer / transport has been successful for describing scattering of light in random media, where the scattering is **elastic**, *i.e.*, the scattered wavelength (which is inversely proportional to photon energy) is the same as the incident wavelength (cf. [1–3]). On the other hand, fluorescence and other luminescence effects are examples of **inelastic** scattering, where the reemitted wavelength differs from the absorbed one. By analogy, it is reasonable to assume that light propagation in a random luminescent medium can be described by an extension of radiative transport theory. Such a theory would be useful in various areas of research, including solar science (see below) and fluorescence optical tomography (cf. [61]). However, very few studies have considered such models. We propose a radiative transport theory to model light propagation in luminescent media [23]. Our approach begins with a general formalism and focuses on modeling luminescent solar concentrators (LSCs).

The fundamental quantity in this theory is the radiance (or specific intensity), which is the power per projected surface area per unit direction per unit wavelength. In elastic scattering, the wavelength dependence of the radiance is usually suppressed. Here, this dependence is included explicitly and the radiance is denoted by

$$I(\mathbf{x}, \Omega, \lambda, t) : \mathfrak{D} \times \mathbf{S}^2 \times \Lambda \times [0, t_{max}] \to \mathbb{R} \geq 0,$$

with $\mathfrak{D} \subset \mathbb{R}^3$ the spatial domain, $\mathbf{S}^2$ the unit sphere of directions, and Λ the set of wavelengths participating in the processes. In general, light propagation in random luminescent media can be described by a general luminescent radiative transport equation (LRTE),

$$\frac{1}{c}\frac{\partial I}{\partial t} + \Omega \cdot \nabla I + \mu_a \mathcal{L}_a I - \mu_r \mathcal{L}_r I = 0 \,, \tag{4.1}$$

where c is light speed, μ_a and μ_r are absorption and reemission constants (in $[1/\mathrm{cm}]$), respectively, and $\mathcal{L}_a, \mathcal{L}_r$ are the corresponding absorption and reemission operators defined below. To model the absorption operator, we recall the Beer-Lambert law, according to which the probability of absorption of light after a propagation distance Δs is

$$P_{abs}(\Delta s; \lambda) = 1 - 10^{-\epsilon(\lambda) M \Delta s} \,, \tag{4.2}$$

where $\epsilon(\lambda)$ is the (dimensional) extinction coefficient (in $[\mathrm{L}/\mathrm{mol\ cm}]$) and M the molar concentration of the luminescent particles (in $[\mathrm{mol}/\mathrm{L}]$). The absorption constant μ_a is proportional to the molar concentration as (see also Appendix A and [45])

$$\mu_a = \ln(10) M \int_\Lambda \epsilon(\lambda)\, d\lambda \,. \tag{4.3}$$

It is convenient to define the normalized absorption spectrum

$$f_a(\lambda) = \frac{\epsilon(\lambda)}{\int_\Lambda \epsilon(\lambda)\, d\lambda}\ . \tag{4.4}$$

Thus, $\int_\Lambda f_a(\lambda) d\lambda = 1$. Combining these definitions, the Beer-Lambert law (4.2) is modeled by

$$\mathcal{L}_a I = f_a(\lambda) I\ . \tag{4.5}$$

In general, the reemission operator in Eq. (4.1) can be written as

$$\mathcal{L}_r I = \int_\Lambda \int_{\mathbf{S^2}} K_r(\lambda, \lambda', \Omega, \Omega') I(\mathbf{x}, \Omega', \lambda')\, d\Omega' d\lambda', \tag{4.6}$$

where $K_r(\lambda, \lambda', \Omega, \Omega')$ is a reemission kernel. The physical meaning of the reemission kernel is the probability that light that is absorbed in direction Ω' and wavelength λ' will be reemitted in direction Ω and wavelength λ.

Since the reemitted wavelength is almost longer than the absorbed one, the reemission operator can be considered as wavelength increasing operator (or energy-decreasing operator),

$$\mathcal{L}_r I = \int_\Lambda \int_{\mathbf{S^2}} P_f(\lambda', \lambda) P_r(\Omega \cdot \Omega') I d\Omega' d\lambda'. \tag{4.7}$$

where $P_r(\Omega \cdot \Omega')$ is the normalized phase function denoting the direction of scattering,

$$\int_{\mathbf{S^2}} P_r(\Omega \cdot \Omega') d\Omega' = 1$$

and $P_f(\lambda', \lambda)$ is the joint probability distribution function for absorption and reemission, *i.e.*

$$P_f(\lambda', \lambda) = f_r(\lambda) f_a(\lambda'), \tag{4.8}$$

$f_r(\lambda)$ is the reemission spectrum [*i.e.*, $\int_\Lambda f_r(\lambda)\, d\lambda = 1$]. To define the direction of reemission, we use the isotropic Henyey-Greenstein scattering phase function [62],

$$P_r(\Theta; g) = \frac{1}{4\pi} \frac{1 - g^2}{(1 - 2g\cos\Theta + g^2)^{3/2}}, \quad \cos\Theta = \Omega \cdot \Omega' \tag{4.9}$$

This determines the amount of light scattered at a relative angle Θ with respect to the direction of incidence. It is important to note that the (elastic scattering) RTE is a special case of the LRTE, *i.e.*

$$K_r(\lambda, \lambda', \Omega, \Omega'; g) = \delta(\lambda - \lambda') P_r(\Omega \cdot \Omega')\ , \tag{4.10}$$

where δ is the Dirac delta function.

In that case, Eq. (4.1) reduces to the standard RTE

$$\frac{1}{c}\frac{\partial I}{\partial t} + \Omega \cdot \nabla I = -\mu_a I + \mu_t \int_{\mathbf{S^2}} P_r(\Omega \cdot \Omega') I(\mathbf{x}, \Omega')\, d\Omega' \,,$$

where $\mu_t = \mu_a + \mu_s$ and μ_s is the scattering constant.

Let us consider light propagation in LSCs based on semiconductor particles. Since solar illumination on the LSC changes very slowly, time dependence can be neglected, leading to the time-independent LRTE

$$\Omega \cdot \nabla I + \mu_a f(\lambda) I - \mu_r \mathcal{L}_r I = 0 \,. \tag{4.11}$$

For LSCs based on semiconductor nanoparticles, such as CdSe-CdTe, the luminescence is approximately independent of the incident radiation [63]. To model this, we propose the "memoryless" anisotropic reemission phase function, $P_r(\Omega \cdot \Omega') = p_r(\Omega; g)\delta(\Omega - \Omega')$, where g is an anisotropy parameter. Unlike the usual notion of anisotropy in radiative transport theory [2], $p_r(\Omega; g)$ depends on the **absolute** angle Ω rather than $\Omega \cdot \Omega'$ for forward-scattering kernels. The corresponding reemission operator is

$$\mathcal{L}_r I = p_r(\Omega; g) f_r(\lambda) \int_{\mathbf{S^2}} \int_{\Lambda} f_a(\lambda') I \, d\Omega' d\lambda' \,, \tag{4.12}$$

where $f_r(\lambda)$ is the normalized reemission spectrum [*i.e.*, $\int_\Lambda f_r(\lambda)\, d\lambda = 1$]. In fluorescent media, the quantum yield, QY, is the probability that a photon that is absorbed will be reemitted (at any wavelength). Therefore, the absorption and reemission constants are related by

$$\mu_r = \mathrm{QY}\mu_a. \tag{4.13}$$

The physical meaning of the reemission operator (5.1) is that the total absorbed light power, *i.e.*, the double integral on the right-hand side of (5.1), is reemitted at wavelengths in accordance with the reemission spectrum, $f_r(\lambda)$.

Recently, [64] proposed two coupled radiative transport equations to model fluorescence imaging (see also [10–12]) for related studies within the diffusion approximation). We also note that radiative transport equations with general kernels of the type (4.6) have been proposed for modeling luminescence for computer graphics applications (cf. [65]). The main advantage of (4.11)–(4.13) is that it depends only on **physically measurable quantities**, *i.e.*, the absorption and reemission spectra, the absorption constant [or, by (4.3), the molar concentration], and the quantum yield. Moreover, this theory allows for modeling accurately the phenomenon of **self-absorption**, *i.e.*, light that has been reemitted can be reabsorbed. Self-absorption is due to the overlap of the absorption and reemission spectra (see Figure 2.3 in Section 2) and sets a fundamental limitation on the performance of LSCs.

To solve (4.11), the boundary conditions must be specified in a well-posed manner. In order to find the radiance in a given luminescent medium $\mathfrak{D}$, we prescribe the boundary

conditions of the form,

$$\begin{aligned} I &= \mathfrak{B} + \mathcal{R}I \quad \text{on } \Gamma_{in} \,, \\ \Gamma_{in} &= \{(\mathbf{x}, \Omega, \lambda) \in \partial D \times \mathbf{S}^2 \times \Lambda,\ \Omega \cdot \hat{n} < 0\}. \end{aligned} \tag{4.14}$$

These conditions prescribe the radiance at the spatial boundary for all directions pointing into the domain, *i.e.*, along the unit outward normal $\hat{n}$. Here, $\mathfrak{B}$ denotes the exterior source incident on the boundary, such as sunlight or a probe beam, and $\mathcal{R}$ denotes the Fresnel reflection operator for the light reflected internally at the boundary due to a mismatch in the refractive index inside and outside of the domain.

Analytical solutions of (4.11) can only be found in special cases. In this study, solutions of this boundary value problem are computed using numerical methods. For simplicity, we assume below that the LSC is infinite in extent in the y direction, so that only one angular variable is needed. As we shall see, the 2D results are qualitatively similar to 3D results for the same setup obtained using Monte Carlo simulations [22]. Therefore, we consider a rectangular LSC, such that x and z are the horizontal and vertical spatial variables on the LSC's edge surface, respectively, and $\varphi \in [0, 2\pi)$ is the angular variable ($\varphi = 0$ along the positive $x-$axis). In this case, the radiance $I(x, z, \varphi, \lambda)$ is measured in units of [$\mathrm{W}/\mathrm{cm\,sr\,nm}$]. The LRTE (4.11) reduces to

$$\cos\varphi \frac{\partial I}{\partial x} + \sin\varphi \frac{\partial I}{\partial z} + \mu_a f_a(\lambda) I - \mu_r f_r(\lambda) p_r(\varphi; g) \int_0^{2\pi} \int_\Lambda f_a(\lambda') I \, d\varphi' d\lambda' = 0 \,.$$

We consider two kinds of particles: spherical CdSe-CdTe quantum dots, which reemit isotropically ($g = 0$ below), and heterojunction CdSe-CdTe nanorods. The nanorods are assumed to absorb light isotropically and luminesce in a preferred direction orthogonal to the long axis ([66]). Assuming these nanorods can be aligned in the LSC (*e*.g. in a liquid crystal matrix) with their long axis perpendicular to the top surface, the luminescence is preferentially in the direction parallel to the top surface. This is designed to reduce the escape of light from the top surface (see corresponding 3D illustration in Figure 2.4 in Section 2).

To model this anisotropic luminescence, we use the Henyey-Greenstein reemission function [[62]] (see Figure 4.1),

$$p_r(\varphi; g) = \frac{1}{2\pi} \frac{1 - g^2}{1 - 2g\cos 2\varphi + g^2} \,. \tag{4.15}$$

For spherical quantum dots, $g = 0$ and $p_r = (2\pi)^{-1}$ is isotropic. In the idealized limiting case, the luminescence would be only in the direction parallel to the top surface. This corresponds to $g \to 1$ and $\lim_{g\to 1} p_r(\varphi; g) = \delta(\cos 2\varphi - 1)$. However, the nanorods cannot be perfectly aligned and cannot luminesce exactly in this way. Therefore, a more realistic case is to consider $0 < g < 1$, which serves to model nanorods that are not ideal in this sense. Thus, for any $0 < g < 1$,, Eq. (4.15) describes luminescence that is preferentially along the $x-$axis in a cone centered about the $x-$axis, whose opening angle decreases monotonically

as g approaches 1 (in the 3D case this corresponds to conical luminescence centered about the $x-y$ plane).

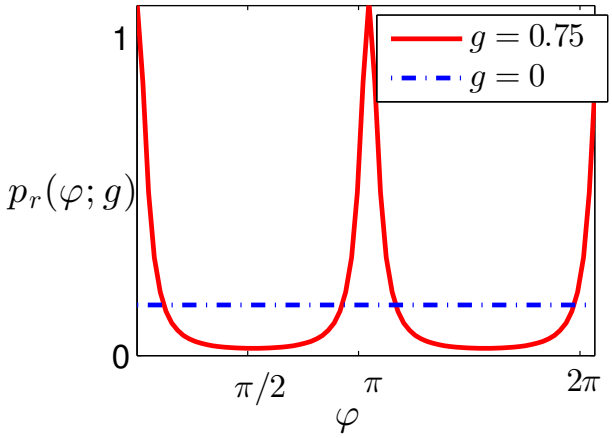

Figure 4.1: Dependence of the reemission phase function (4.15) on the polar angle φ for isotropic quantum dots ($g = 0$, dot-dashed line) and aligned nanorods ($g = 0.75$, solid curve). The nanorods luminesce preferentially along the $x-$axis, *i.e.*, $\varphi = 0$ and $\varphi = \pi$.

We now consider a box-shaped LSC of length is l_x, $x \in [-\frac{l_x}{2}, \frac{l_x}{2}]$ and thickness (or height) l_z, $z \in [-\frac{l_z}{2}, \frac{l_z}{2}]$. The solar PV cell covers the right side $x = \frac{l_x}{2}$. We assume the PV absorbs all the light that impinges on it. This can be modeled using the "vacuum" boundary conditions

$$I(\frac{l_x}{2}, z, \varphi, \lambda) = 0, \quad \varphi \in \left(\frac{\pi}{2}, \frac{3\pi}{2}\right) . \tag{4.16}$$

The bottom surface and the left edge surface are assumed to be covered by perfect mirrors. The associated boundary conditions are

$$I(-\frac{l_x}{2}, z, \varphi, \lambda) = I(-\frac{l_x}{2}, z, \pi + \varphi, \lambda), \ \varphi \in \left(-\frac{\pi}{2}, \frac{\pi}{2}\right), \tag{4.17}$$

$$I(x, -\frac{l_z}{2}, \varphi, \lambda) = I(x, -\frac{l_z}{2}, 2\pi - \varphi, \lambda), \ \varphi \in (\pi, 2\pi) . \tag{4.18}$$

At the top surface, for $\varphi \in (\pi, 2\pi)$, light is partially reflected as

$$I(x, \frac{l_z}{2}, \varphi, \lambda) = \mathfrak{B}(\varphi, \lambda) + r(2\pi - \varphi) I(x, \frac{l_z}{2}, 2\pi - \varphi, \lambda) , \tag{4.19}$$

where $r(\varphi)$ is the Fresnel reflection coefficient for unpolarized light [67] and $\mathfrak{B}$ the solar illumination on the top surface (after transmission into the LSC) , which is assumed to be

spatially uniform and centered at normal incidence $\varphi = 3\pi/2$, *i.e.*

$$\mathfrak{B}(\varphi, \lambda) = f_{sol}(\lambda) e^{-8(\varphi - \frac{3\pi}{2})^2}, \quad \varphi \in (\pi, 2\pi), \tag{4.20}$$

where $f_{sol}(\lambda)$ is the solar irradiance measured at sea level [47].

4.2 Solving LRTE numerically

We solve the boundary value problem (4.15)–(4.20) using the Source Iteration method [cf. [4]] and an upwinding numerical scheme.

The Source Iteration method is an efficacious approach for solving boundary value problems that involve large linear systems. To use it, the discretized radiance is denoted as $I_{i,j,m,\ell}$, where (i, j, m, ℓ) are the indices corresponding to (x, z, φ, λ) and the number of corresponding grid points are $(N_x, N_z, N_\varphi, N_\lambda)$. We seek an iterative solution as

$$I(x, z, \varphi, \lambda) \approx I_{i,j,m,\ell} \approx \sum_{s=0}^{\text{maxiter}} I^{(s)}_{i,j,m,\ell} \, ,$$

where maxiter denotes the number of iterations for the solution to converge. As a stopping criterion, we use

$$\|I^{(s)}(x, z, \varphi, \lambda)\|_\infty = \max_{i,j,m,\ell} |I^{(s)}_{i,j,m,\ell}| \leq \Delta$$

within a fixed tolerance of $\Delta = 10^{-5}$ (see Appendix A further details for the implementation) The source iteration method converges rapidly after relatively few iterations. For example, choosing the physical constants as $l_x = 3$ cm, $l_z = 0.4$ cm, $\mu_a = 600[\,1/\text{cm}\,]$, $\text{QY} = 0.95$, and anisotropy parameter $g = 0.75$, and the numerical grid sizes as $N_x = 48, N_z = 6, N_\varphi = 80$, and $N_\lambda = 14$, the solution converges within 250 iterations (see Figure 4.2).

4.3 The LSC Performance Metrics

There are three kinds of loss mechanisms of light in LSCs are (cf. [29, 31, 68]).

1. Reemission losses. Light that is absorbed is not necessarily reemitted. This is captured by the quantum yield, QY.

2. Self-absorption losses. Light that is reemitted can be reabsorbed (self-absorption). In general, light can undergo multiple absorption and reemission events, which reduces its intensity inside the LSC. Self-absorption is due to the overlap of the absorption and reemission spectra. Thus, self-absorption is determined primarily by the quantum yield and the absorption and reemission spectra.

3. Escape losses. Light can escape from the top surface of the LSC.

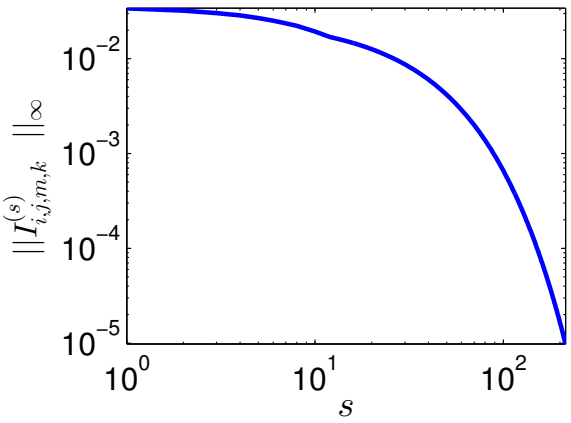

Figure 4.2: Convergence of the LRTE solution as a function of iteration number (loglog plot).

We refer to the combination of the reemission and self-absorption losses as "combined absorption losses".

Our goal is to optimize the experimentally controllable LSC design parameters, so as to minimize these losses and, therefore, maximize the light that reaches the PV. To this end, we assume that the absorption and reemission spectra are fixed as shown in Figure 2.3 in Section 2 and that the quantum yield is fixed as $QY = 0.95$. These are measured values for CdSe/CdTe semiconductor particles [[22]]. We assume that the **controllable LSC design parameters** are:

1. The absorption constant, μ_a, or, equivalently by (4.3), the molar concentration of the particles.

2. The LSC size, *i.e.*, the thickness l_z and length l_x.

3. The anisotropy factor g of the aligned nanorods.

An often used LSC performance metric is the"optical efficiency", which is the ratio of the spectral power at a particular wavelength collected by the PV cell to the solar spectral power at a particular wavelength that is incident on the top surface, *i.e.*,

$$\eta_{pv}(\lambda) = \frac{\Phi_{pv}(\lambda)}{\Phi_{sol}(\lambda)}, \tag{4.21}$$

where

$$\Phi_{pv}(\lambda) = \int_{-\frac{l_z}{2}}^{\frac{l_z}{2}} \int_{-\frac{\pi}{2}}^{\frac{\pi}{2}} I(\frac{l_x}{2}, z, \varphi, \lambda')\, d\varphi dz,$$

Φ_{pv}, denotes the spectral power at a particular wavelength at the PV edge in [W/nm]. Φ_{sol} is the solar spectral power at a particular wavelength at the LSC's top surface in [W/nm],

$$\Phi_{sol}(\lambda) = l_x \int_{\pi}^{2\pi} \mathfrak{B}(\varphi, \lambda)\, d\varphi.$$

Using (4.20),

$$\Phi_{sol}(\lambda) = C l_x f_{sol}(\lambda), \quad C \approx 0.62\ .$$

We define the wavelength-averaged optical efficiency,

$$\overline{\eta}_{pv} = \frac{\int_\Lambda \eta_{pv}(\lambda) d\lambda}{\int_\Lambda \Phi_{sol}(\lambda) d\lambda}\ , \tag{4.22}$$

and wavelength-averaged losses due to escape from the top surface,

$$\overline{\eta}_{top} = \frac{\int_\Lambda \Phi_{top}(\lambda) d\lambda}{\int_\Lambda \Phi_{sol}(\lambda) d\lambda}, \tag{4.23}$$

where the spectral power at a particular wavelength that escapes from the LSC is

$$\Phi_{top}(\lambda) = \int_{-\frac{l_x}{2}}^{\frac{l_x}{2}} \int_0^{\pi} [1 - r(\varphi)] I(x, \frac{l_z}{2}, \varphi, \lambda) d\varphi dx, \tag{4.24}$$

where $[1 - r(\varphi)]$ is the fraction of the reemitted light that is transmitted outside the LSC (cf. [28]). Since light is either collected by the PV, escapes from the top surface, or combined absorption losses, the wavelength-averaged combined absorption loss is

$$\overline{\eta}_{abs} = 1 - \overline{\eta}_{pv} - \overline{\eta}_{top}. \tag{4.25}$$

Finally, as discussed in Section 4.4.1, another useful metric for the LSC performance is the LSC optical gain [22],

$$\overline{\Gamma} = \overline{\eta}_{pv} \times G, \quad G \doteq \frac{A_{top}}{A_{pv}} \doteq \frac{l_x}{l_z}, \tag{4.26}$$

where G is often called the geometric gain factor, A_{top} is top surface area, and A_{pv} is area covered by PV cell.

4.4 Computational results

To make detailed computations for the semiconductor LSC performance, we solve the boundary value problem (4.15)–(4.20) for particular LSC design parameters, *i.e.*, $\mathrm{QY} = 0.95$ and $l_z = 0.4$ cm. The refractive index of the LSC waveguide is taken as $n_{LSC} = 1.7$. From Snell's law, light is captured in the LSC whenever the reemitted polar angle is greater

than 36^o. We seek the optimal design parameters mentioned above, *i.e.*, μ_a and G.

4.4.1 Optimal LSC design parameters

Optimal absorption constant

To optimize the LSC design parameters, at first we seek the optimal absorption constant, μ_a. Here we use $g = 0.75$. Figure 4.3 shows the wavelength-averaged optical efficiency and loss mechanisms as functions of μ_a. At low particle concentrations ($\mu_a < 100$ [1/cm]), much of the incident light is lost due to top loss. Since the light is incident at normal angle, most of the light escapes from the LSC's top surface. At low particle concentration, as seen in Figure 4.3, a small amount of light is either collected or lost due to self-absorption .

It is well known that numerical solutions of radiative transport equation tend to have different characteristics for weak scattering media and localized sources. This is due, in part, to the angular discretization leading to the "ray effects" (cf. [4]), in the weakly scattering regime, *i.e.*, for small μ_a, and when the source is collimated. In this regime, the source iteration method becomes highly sensitive to the angular discretization. The ray effects are implicitly included in the combined absorption loss (4.25). This explains why the absorption loss does not vanish at low particle concentrations. On the other hand, ray effects are mitigated in the strongly scattering regime, *i.e.*, for large μ_a. In the intermediate regime, Figure 4.3 shows that the optical efficiency has a maximum value, $\max_{\mu_a}(\overline{\eta}_{pv}) \approx 0.3$, obtained at $\mu_{opt} \approx 600$ [1/cm]. At this optimal value, the absorption losses are somewhat large and the escape from the top surface is quite small. Hence, the optimal absorption constant is obtained from a balance between these competing loss mechanisms.

Effect of anisotropy

We now seek to study the effect of anisotropy of the luminescence on the LSC performance. We use the previously given LSC dimensions , $\mu_a = 600$, and vary the anisotropy factor, g, in the reemission function (4.15). Figure 4.4 shows that the LSC performance increases monotonically with g. In particular, in the ideal case of $g = 1$, when light is reemitted only in the $\pm x$ directions, the LSC optical gain is 30% greater than using isotropic quantum dots. This suggests that aligning the nanorods can have a significant impact on the LSC performance.

Optimal LSC length

To optimize the LSC's length using the concept of geometric gain factor [see (4.26)], the idea is to make the area covered by the PV cell constant, while the top surface area is varied. To do this, we use $\mu_a = 600$ [1/cm], the anisotropy factor $g = 0.75$, and vary the length l_x, while fixing the thickness at $l_z = 0.4$ cm. The results in Figure 4.5 show that the optical efficiency decreases as the length l_x increases. This makes sense, because as l_x increases, light has to travel a longer distance to reach the PV, thus increasing the losses due to escape from the top surface and self-absorption. However, the optical efficiency is

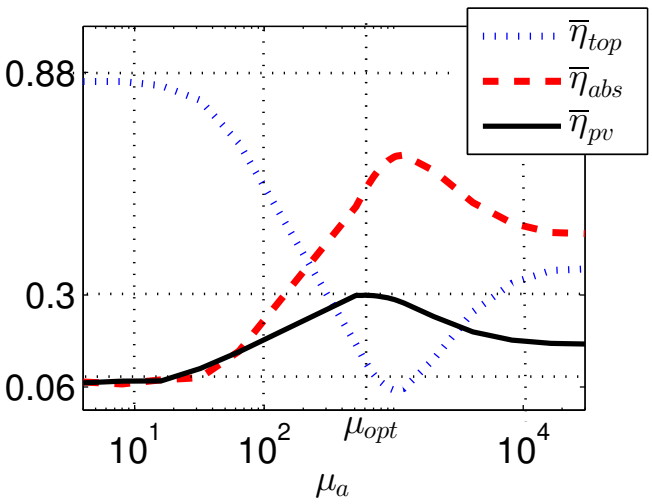

Figure 4.3: Wavelength-averaged optical efficiency [Eq. (4.22) (solid)], the averaged escape losses from the top surface [Eq. (4.23) (dots)], and the combined absorption losses [Eq. (4.25) (dashes)], as functions of the absorption constant, μ_a (in $[1/\text{cm}]$) using aligned nanorods ($g = 0.75$).

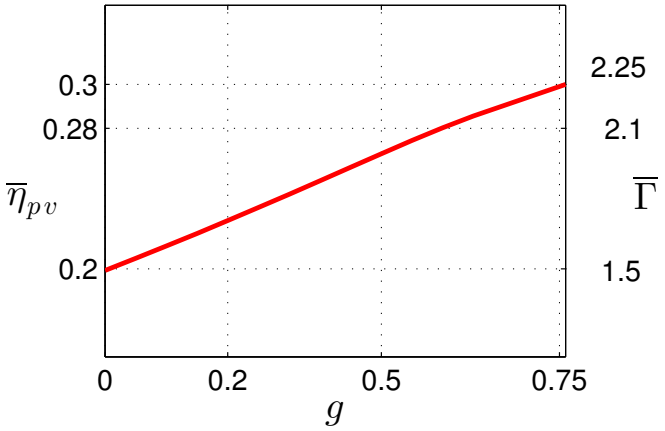

Figure 4.4: Wavelength-averaged optical efficiency (left axis) and LSC optical gain (right axis) as functions of the anisotropy factor.

not the right metric for predicting the LSC's performance, because it is based on power rather than power density.

Figure 4.6 shows that the optimal geometric gain factor is $G_{opt} \approx 27$, which corresponds to $l_x \leq 10.8$ cm. Thus, the optimal LSC design is fairly thin (in z) and long (in

x). Furthermore, the maximal LSC optical gain is $\overline{\Gamma}^{max} \approx 4$. While this is an idealized 2D scenario, it is nonetheless encouraging for using aligned nanorods.

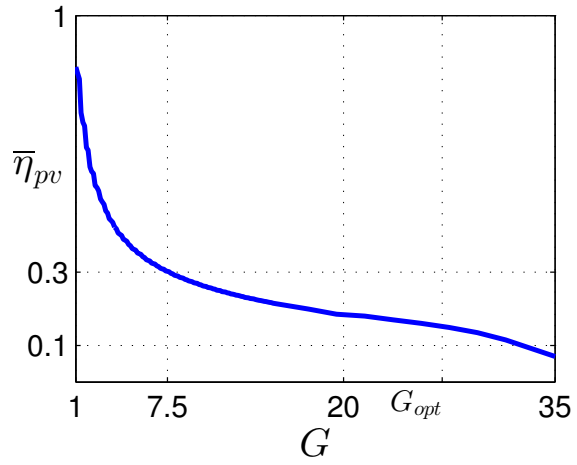

Figure 4.5: Wavelength-averaged optical efficiency with $\mu_a = 600$ and $g = 0.75$ as a function of the geometric gain factor $G = \dfrac{l_x}{l_z}$ with $l_z = 0.4$ cm.

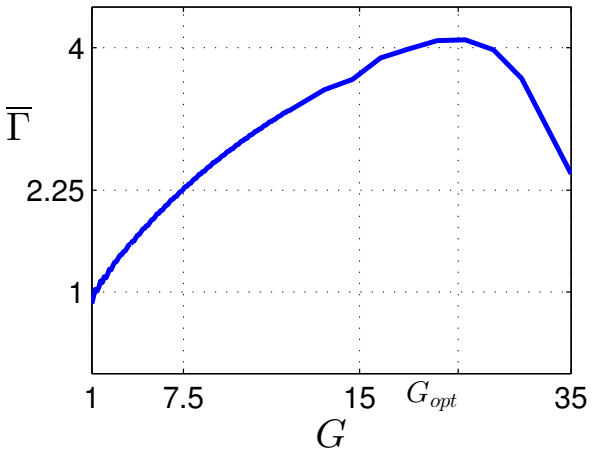

Figure 4.6: LSC optical gain for the same parameters as in Figure 4.5.

4.5 Monte-Carlo method for light propagation in LSCs

In order to validity of the LRTE model, the above LRTE results are compared with the ones obtained by MC simulations. To do that, we use a 2D version of the MC algorithm as previously mentioned in Chapter 3. We assume that light is normally incident on the top surface, use the "particles" as above, *i.e.*, same absorption and reemission spectra, $QY = 0.95, g = 0.75$, and use the same boundary conditions as above.

Briefly, to obtain accurate results, a "photon packet" of 10^6 "photons" (or discrete particles), whose wavelengths are sampled from the solar spectrum, are incident on the top surface uniformly in x. Each photon is tracked until either collected at the PV or lost. The probability of absorption is calculated using (4.2). Specifically, in order to accelerate the MC computations (cf. [22,29,37]), the probability that a photon entering the LSC at normal incidence is initially absorbed is computed as

$$\xi \ \leq \ P_{abs}(2l_z, \lambda_i) \ , \tag{4.27}$$

where λ_i is the incident wavelength and ξ is a uniform random variable in $(0, 1)$. When (4.27) is not satisfied, the incident photon is assumed not to be captured inside the LSC. If a photon is initially captured in the LSC, its reemission probability is the quantum yield, QY. If reemitted, the photon's wavelength, direction, and position are updated as follows. The reemitted wavelength is sampled from $f_r(\lambda)$. The direction of the reemitted photon is found from the accumulated distribution function Θ obtained from (4.15) (see also Appendix B), *i.e.*,

$$P(\varphi; g) \ = \ \frac{1}{2\pi} \begin{cases} \Theta(\varphi; g), & \varphi \in [0, \pi/2), \\ \pi + \Theta(\varphi; g), & \varphi \in [\pi/2, 3\pi/2), \\ 2\pi + \Theta(\varphi; g), & \varphi \in [3\pi/2, 2\pi), \end{cases} \tag{4.28}$$

where

$$\Theta(\varphi; g) = \tan^{-1}\left(\tilde{g} \tan \varphi\right) , \quad \tilde{g} = \frac{1-g}{1+g}.$$

Inverting (B.4), the reemission angle is computed as

$$\varphi \ = \ \begin{cases} \tan^{-1}[\tilde{g} \tan(2\pi\xi)], & \xi \in [0, 1/4); \\ \tan^{-1}[\tilde{g} \tan(\pi(2\xi - 1))], & \xi \in [1/4, 3/4); \\ \tan^{-1}[\tilde{g} \tan(2\pi(\xi - 1))], & \xi \in [3/4, 1), \end{cases}$$

where ξ is a uniformly random variable in $(0, 1)$. The photon's position is then updated using

$$x' = x + \Delta s \cos \varphi, \quad z' = z + \Delta s \sin \varphi \ , \tag{4.29}$$

where Δs is found by inverting the Beer-Lambert law (4.2) as

$$\Delta s \;=\; -\frac{1}{\epsilon(\lambda)\, M}\log_{10}\xi\,, \tag{4.30}$$

where ξ is a random variable uniformly distributed in $(0,1)$. If the photon reaches the PV cell at $x = \frac{l_x}{2}$, it is assumed to be collected. The LSC performance metrics are computed similarly to (4.21)–(4.26).

4.5.1 Comparison of LRTE and Monte Carlo approaches

Using the MC method outlined above and the same LSC size $l_x = 3$ cm $l_z = 0.4$ cm and anisotropy factor $g = 0.75$, the wavelength-averaged optical efficiency (4.22) is computed while varying the absorption constant, μ_a. In order to compare the results with the LRTE computations, we use (4.3). Figure 4.7 shows that the optimal absorption constants are almost the same using the LRTE and MC approaches ($M_{opt} \approx 2.6\times10^{-6}$ $[\mathrm{mol}/\mathrm{L}]$, $\mu_{opt} \approx 600$). Furthermore, the maximal optical efficiency is also approximately the same as found using the LRTE approach, *i.e.*, $\overline{\eta}_{pv} \approx 0.3$. This shows the consistency between the deterministic LRTE and the statistical MC approaches.

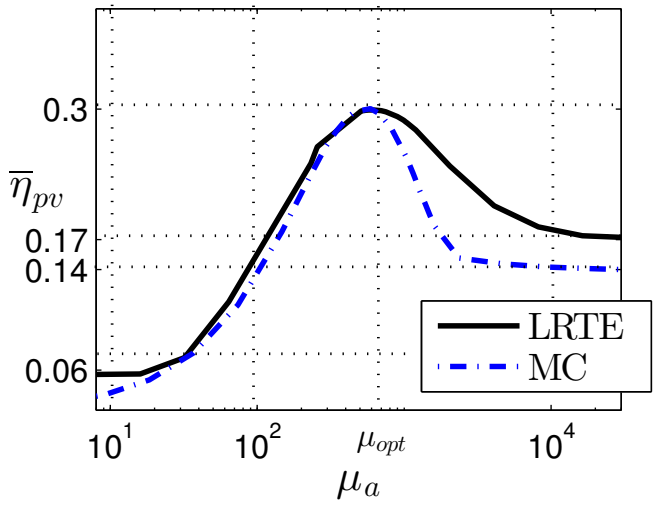

Figure 4.7: Wavelength-averaged optical efficiency as a function of the absorption constant obtained using the LRTE (solid) and MC (dashes).

4.6 Summary and Discussions

The results of this study shows that deterministic and the statistical approaches complement each other. The Monte Carlo approach is conceptually simpler, easier to code, and has certain numerical advantages while dealing with highly-collimated sources and weak scattering medium. The MC method is flexible to use for multi-dimensional problems, however, it converges very slowly. On the other hand, deterministic computational techniques for the standard RTE are quite efficient and are also commonly used in the literature to model real-world problems (cf. [69]). The LRTE has an additional "dimension" compared with the standard RTE, *i.e.*, wavelength λ. This study shows that the LRTE can be solved computationally by adapting existing numerical methods. The agreement between the MC and LRTE approaches serves to validate each other (cf. [70] for a rigorous comparison between these approaches). Another benefit of the LRTE is that it is amenable to further analytical modeling, *i.e.*, rigorous mathematical techniques and asymptotics.

Chapter 5

Radiative Transport Theory for Optically Thick Media

In radiative transport theory, for inelastic scattering problems almost all of the previous studies have modeled the system in terms of **coupled radiative transport equations for the absorption and reemission** (*i.e.*, the excitation and fluorescence). Moreover, almost all of these studies have considered the problems in optically thick media, *i.e.*, in the highly scattering / weakly absorbing regime. Within radiative transfer theory, this is known as the "diffusion approximation", and, in the aforementioned studies, has led to coupled partial differential equations.

As mentioned in chapter 4, in this research we developed a radiative transport theory for light propagation in luminescent media based on a **single radiative transport equation that takes both absorption and reemission into account.** One advantage of this approach is that it uses measurable optical properties and physical parameters. This luminescent radiative transport equation (**LRTE**) is the starting point of our study. We seek asymptotic solutions of the LRTE for optically thick media. Using asymptotic methods, we derive a corrected diffusion approximation, which consists of a single partial differential equation, in which the wavelength appears as a parameter, with associated boundary conditions and a boundary layer solution. The accuracy of this approach is verified for a plane-parallel slab problem. In particular, the reduced system captures accurately the reabsorption of light, which is an important aspect of the problem for applications [24].

In Section 5.1, starting with the LRTE in its scaled form [see (5.3) and (5.6)] and using asymptotic methods, a diffusion approximation is derived including the interior and boundary layer solutions. In Section 5.2, the plane-parallel slab problem is solved for the special case when the incident light is a collimated beam. In particular, we show that the reduced system captures accurately the reabsorption of light. In Section 5.3, the validity of the diffusion approximation is verified by comparison with direct computation of the LRTE. The impact of varying the Stokes shift, *i.e.*, the mean wavelength separation between the absorption and reemission spectra, is investigated in Section 5.3.1. To systematically analyze various physical assumptions and regimes, we employ "synthetic" luminescence data in the form of Gaussian distributions. However, for a more realistic scenario,

in Section 5.3.2 we test the reliability of the diffusion approximation using experimentally measured luminescence data.

In this research, to model propagation of light in optically-thick luminescent media, the following steady-state luminescent radiative transport equation **(LRTE)** is used.

$$\Omega \cdot \nabla I + \mu_a \mathcal{L}_a I = \mu_r \mathcal{L}_r I,$$

$\mathcal{L}_a, \mathcal{L}_r$ are the corresponding absorption and reemission operators defined same as in Chapter 4. The reemission operator in Eq. (4.11) is

$$\mathcal{L}_r I = \int_\Lambda \int_{\mathbf{S^2}} K_r(\lambda, \lambda', \Omega, \Omega'; g) I(\mathbf{x}, \Omega', \lambda')\, d\Omega' d\lambda',$$

where $K_r(\lambda, \lambda', \Omega, \Omega'; g)$ is a reemission kernel,

$$\mathcal{L}_r I = \int_\Lambda \int_{\mathbf{S^2}} P_f(\lambda', \lambda) P_r(\Omega \cdot \Omega') I d\Omega' d\lambda'. \tag{5.1}$$

where $P_r(\Omega \cdot \Omega')$ is the normalized phase function denoting the direction of scattering,

$$\int_{\mathbf{S^2}} P_r(\Omega \cdot \Omega') d\Omega' = 1$$

and $P_f(\lambda', \lambda)$ is the joint probability distribution function for absorption and reemission, *i.e.*

$$P_f(\lambda', \lambda) = f_r(\lambda) f_a(\lambda')$$

$f_r(\lambda)$ is the reemission spectrum [*i.e.*, $\int_\Lambda f_r(\lambda)\, d\lambda = 1$]. To define the direction of reemission, we use the isotropic Henyey-Greenstein scattering phase function [62],

$$P_r(\Theta; g) = \frac{1}{4\pi} \frac{1 - g^2}{(1 - 2g\cos\Theta + g^2)^{3/2}}, \quad \cos\Theta = \Omega \cdot \Omega' \tag{5.2}$$

This determines the amount of light scattered at a relative angle Θ with respect to the direction of incidence.

In order to find the radiance in a given luminescent medium $\mathfrak{D}$, we prescribe the same boundary conditions 4.14 in Chapter 4, *i.e.*

$$I = \mathcal{R} I + \mathfrak{B} \quad \text{on} \quad \Gamma_{in} = \{(\mathbf{x}, \Omega, \lambda) \in \partial\mathfrak{D} \times \mathbf{S}^2 \times \Lambda,\ \Omega \cdot \hat{n} < 0\}.$$

5.1 Diffusion approximation in optically thick media

In general, radiative transport equations are difficult to solve without introducing approximations. In optically-thick, *i.e.*, highly scattering media, the time-independent radiative transfer equation can be approximated with an elliptic (local) partial differential equation,

which is called the diffusion approximation (**DA**) (cf. [5, 71–73]). However, it is well-known that the standard DA is not very accurate near the boundaries (cf. [74–78]). In order to address this limitation accurately, Larsen and Keller used boundary layer matched expansion techniques ([79–81]). Many studies have addressed this limitation using various other methods. In this study, following Larsen and Keller's approach, we use boundary layer matched expansion techniques asymptotically, and we derive a diffusion approximation based on the LRTE. Following [82], our derivation leads to a corrected DA. Here, we refer to the approximation in the interior of the domain as DA, whereas, the corrected DA is referred to as the "diffusion approximation with a boundary layer" or **DABL** (see Figure 5.1).

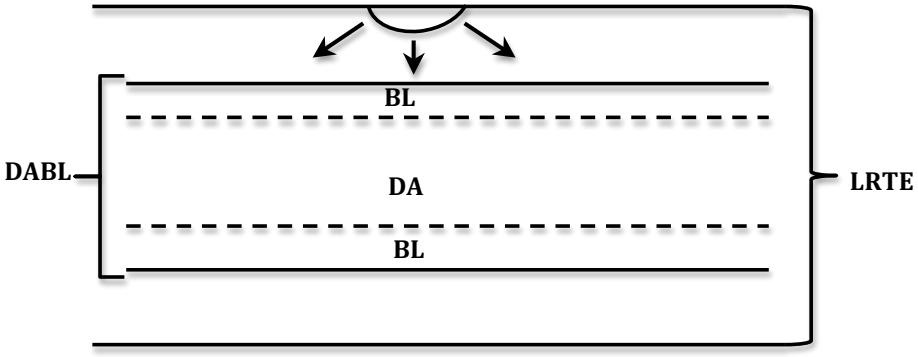

Figure 5.1: A schematic representation of regions of validity for each part of the asymptotic approximation.

Before introducing the asymptotic analysis, it is convenient to rewrite the LRTE (4.11) as

$$\Omega \cdot \nabla I + \underbrace{\mu_a(1-\mathrm{QY})f_a(\lambda)I}_{\text{absorption}} + \underbrace{\mu_a f_a(\lambda)\mathrm{QY}\mathcal{L}I}_{\text{reemission}} = 0\,, \tag{5.3}$$

where

$$\mathcal{L}I = I - \frac{f_r(\lambda)}{f_a(\lambda)} \int_{\mathbf{S^2}} \int_{\Lambda} P_r(\Omega \cdot \Omega') f_a(\lambda') I d\lambda' d\Omega'. \tag{5.4}$$

Assumption 1. *We make the following physical assumptions about the medium and source terms.*

1. *The medium has a quantum yield close to unity,* i.e.*,*

$$\mathrm{QY} \;=\; 1-\epsilon^2\,, \quad 0<\epsilon \ll 1\,. \tag{5.5}$$

2. *The absorption constant is* $\mu_a = \dfrac{\alpha}{\epsilon}$*, where* $\alpha = \mathcal{O}(1)$ *is a rescaled absorption constant.*

3. *The absorption and reemission spectra scale as $f_a = \mathcal{O}(1)$ and $f_r = \mathcal{O}(1)$.*

4. *The spatial variations of the incident source and of the boundary of the domain are small compared with ϵ.*

Assumption (1) is suitable for many organic and semiconductor fluorescent particles, whose quantum yield can be as high as 95% or higher (cf. [22,37]). The other assumptions ensure that the validity of the asymptotic scaling (cf. [79, 81] for a detailed discussion of the smoothness assumptions).

Introducing these assumptions into (5.3) leads to

$$\epsilon\Omega \cdot \nabla I + \epsilon^2 \alpha f_a(\lambda) I + (1-\epsilon^2)\alpha f_a(\lambda)\mathcal{L}I = 0\ . \tag{5.6}$$

This equation is our starting point of the asymptotic analysis.

5.1.1 Asymptotic analysis

We seek an approximate solution of (5.6) with the boundary condition (4.14) in the form

$$I_{\mathrm{DABL}} \approx \Phi_{int} \ + \ \Psi_{BL}, \tag{5.7}$$

where Φ_{int} is the interior solution, *i.e.*the corrected DA, and Ψ_{BL} is the boundary layer solution. The governing equations for Φ_{int} and Ψ_{BL} are derived below.

Corrected interior layer solution Φ_{int}

In the interior of the domain, we expand the solution as

$$\Phi_{int} = \phi_0 + \epsilon\phi_1 + \dots\ . \tag{5.8}$$

Substituting (5.8) into (5.6) and collecting in powers of ϵ, leads to

$$-\alpha f_a(\lambda)\mathcal{L}\phi_k = \Omega \cdot \nabla\phi_{k-1} + \alpha f_a(\lambda)[\mathbb{I} - \mathcal{L}]\phi_{k-2}, \quad k = 0, 1, \dots\ , \tag{5.9}$$

where $\mathbb{I}$ is the identity operator and it is implied that $\phi_{-2} = \phi_{-1} \equiv 0$. For $k = 0$, the leading order equation in (5.9) is

$$\mathcal{L}\phi_0 = 0. \tag{5.10}$$

Using (5.4) and (5.10) gives

$$\phi_0 = \frac{f_r(\lambda)}{f_a(\lambda)} \int_{\mathbf{S^2}} \int_{\Lambda} P_r(\Omega \cdot \Omega') f_a(\lambda')\phi_0 d\Omega' d\lambda'. \tag{5.11}$$

Since the right-hand side does not depend on Ω, ϕ_0 does not depend on the direction. In other words, the eigenfunction of $\mathcal{L}$ with a zero eigenvalue is an isotropic function. Hence,

$$\phi_0 = \phi_0(\mathbf{x}, \lambda). \tag{5.12}$$

For $k = 1$, Eq. (5.9) gives

$$-\alpha f_a(\lambda)\mathcal{L}\phi_1 = \Omega \cdot \nabla\phi_0 \tag{5.13}$$

We seek a solution of the form

$$\phi_1 = \frac{C}{f_a(\lambda)}\Omega \cdot \nabla\phi_0 \; . \tag{5.14}$$

where C is the undetermined constant. Substituting (5.14) into (5.13) leads to

$$-\alpha C\Omega \cdot \nabla\phi_0 + \alpha C f_r(\lambda) \int_\Lambda \int_{\mathbf{S^2}} P_r(\Omega \cdot \Omega')\Omega' \cdot \nabla\phi_0 d\Omega' d\lambda' = \Omega \cdot \nabla\phi_0 \; . \tag{5.15}$$

To continue, we need a certain identity. It can be shown that for any isotropic function, $P(\Omega \cdot \Omega')$, and any vector function $\mathbf{F}(\cdot)$ that does not depend on Ω, the following identity holds [cf. [2]]

$$\int P(\Omega \cdot \Omega')\Omega' \cdot \mathbf{F} d\Omega' = g\Omega \cdot \mathbf{F} \; , \tag{5.16}$$

where the integration is over all directions and g is the first moment of $P(\Omega \cdot \Omega')$. Using (5.16) with P given by (5.2) and $\mathbf{F} = \nabla\phi_0$, Eq. (5.15) becomes

$$\alpha C\Omega \cdot \nabla\phi_0 - \alpha f_r(\lambda) C g \Omega \cdot \int_\Lambda \nabla\phi_0 d\lambda' = -\Omega \cdot \nabla\phi_0. \tag{5.17}$$

Integrating (5.17) over Λ and using $\int_\Lambda f_r(\lambda)d\lambda = 1$, after rearranging the terms we obtain

$$\Omega \cdot \int_\Lambda \nabla\phi_0 d\lambda' \left[1 + C\alpha(1-g)\right] = 0 \; . \tag{5.18}$$

Since ϕ_0 is isotropic and its gradient is nonzero, Eq. (5.18) yields the undetermined constant as

$$C = -\frac{1}{\alpha(1-g)}. \tag{5.19}$$

Hence, the first-order correction term is

$$\phi_1 = -\frac{1}{\alpha(1-g)f_a(\lambda)}\Omega \cdot \nabla\phi_0 \; . \tag{5.20}$$

For $k = 2$, Eq. (5.9) gives

$$\Omega \cdot \nabla\phi_1 + \alpha f_a(\lambda)[\mathbb{I} - \mathcal{L}]\phi_0 = -\alpha f_a(\lambda)\mathcal{L}\phi_2 \; . \tag{5.21}$$

Substituting $\mathcal{L}\phi_0 = 0$ and (5.20) gives

$$\Omega \cdot \nabla \cdot \left[-\frac{\Omega \cdot \nabla\phi_0}{\alpha(1-g)f_a(\lambda)}\right] + \alpha f_a(\lambda)\phi_0 = -\alpha f_a(\lambda)\mathcal{L}\phi_2. \tag{5.22}$$

To continue, we integrate both sides over $\mathbf{S^2} \times \Lambda$. Regarding the right-hand side, we recall that

$$\mathcal{L}\phi_2 = \phi_2 - \frac{f_r(\lambda)}{f_a(\lambda)} \int_{\mathbf{S^2}} \int_{\Lambda} P_r(\Omega \cdot \Omega') f_a(\lambda') \phi_2 d\Omega' d\lambda'. \tag{5.23}$$

Multiplying $\mathcal{L}\phi_2$ by $f_a(\lambda)$ and integrating over $\mathbf{S^2} \times \Lambda$ gives

$$\begin{aligned} \int_{\Lambda} \int_{\mathbf{S^2}} f_a(\lambda) \mathcal{L}\phi_2 \, d\Omega d\lambda &= -\int_{\Lambda} f_r(\lambda) d\lambda \int_{\mathbf{S^2}} P_r(\Omega \cdot \Omega') \, d\Omega \int_{\Lambda} \int_{\mathbf{S^2}} f_a(\lambda) \phi_2 \, d\Omega d\lambda \\ &+ \int_{\Lambda} \int_{\mathbf{S^2}} f_a(\lambda) \phi_2 \, d\Omega d\lambda \end{aligned}$$

.

Since $\int_{\Lambda} f_r(\lambda) d\lambda = 1$ and $\int_{\mathbf{S^2}} P_r(\Omega \cdot \Omega') \, d\Omega = 1$, it follows that the right-hand side is zero. Hence, the double integral of the right-hand side of (5.22) vanishes. Using the divergence theorem for the left-hand side of (5.22), we obtain

$$\int_{\Lambda} \left[\nabla \cdot (\kappa \nabla \phi_0) - \alpha f_a(\lambda) \phi_0 \right] d\lambda = 0 \, . \tag{5.24}$$

where the diffusion coefficient is

$$\kappa(\lambda) = \frac{1}{3(1-g)\alpha f_a(\lambda)}. \tag{5.25}$$

In order to obtain a unique solution of (5.24) subject to the boundary conditions (4.14), a sufficient condition is to require that the integrand of (5.24) vanishes, *i.e.*,

$$\nabla \cdot (\kappa \nabla \phi_0) - \alpha f_a(\lambda) \phi_0 = 0 \, . \tag{5.26}$$

Thus, to $\mathcal{O}(\epsilon)$, the interior solution Φ_{int} is

$$\Phi_{int} \sim \phi_0 - 3\kappa\epsilon\Omega \cdot \nabla \phi_0 \, , \tag{5.27}$$

where ϕ_0 satisfies (5.26). This is the corrected DA. We remark that the "standard" DA is

$$\Phi_{DA} \sim \phi_0 \, , \tag{5.28}$$

i.e., the solution of (5.26). Hence, the corrected DA (5.27) has the additional $\mathcal{O}(\epsilon)$ term. However, for the solution of (5.26) to be correct to $\mathcal{O}(\epsilon)$, **the boundary conditions for** (5.26) **must be asymptotically accurate to** $\mathcal{O}(\epsilon)$ **as well.** As shown in Section 5.2.3, for this to hold, the corrected DA (5.27) is necessary.

Boundary layer solution Ψ_{BL}

In the boundary layer, we seek an approximate solution Ψ_{BL} of (5.6) in a neighborhood of a particular point $\mathbf{x}_b$ on the smooth boundary of $\partial\mathfrak{D}$. To do this, a new coordinate system

is defined with $\mathbf{x}_b$ at the origin and $\mathbf{x} \mapsto (\rho, \zeta)$, where $\zeta \parallel \hat{n}(\mathbf{x}_b)$ and $\rho \perp \hat{n}(\mathbf{x}_b)$. Thus, the new angular variables are

$$\mu = \Omega \cdot \hat{n}(\mathbf{x}_b) = \cos\theta, \quad \mu \in [-1, 1] \,, \tag{5.29}$$

$$\Omega_\perp = \sqrt{1-\mu^2}(\cos\varphi, \sin\varphi), \quad \varphi \in [-\pi, \pi]. \tag{5.30}$$

We consider the source term on $\partial\mathfrak{D}$, *i.e.*, at $\zeta = 0$, to be a slowly-varying and axisymmetric about $\hat{n}(\mathbf{x}_b)$ for all $\mathbf{x}_b \in \partial\mathfrak{D}$. Therefore, using the notation of (4.14), the boundary source term is denoted as $\mathfrak{B}(\rho, \mu, \lambda)$, *i.e.*, independent of $\Omega_\perp$. Similarly, the Fresnel reflection operator in (4.14) is assumed to be axisymmetric and

$$\mathcal{R}[I(\mu, \cdot)] \equiv r(\mu) I(-\mu, \cdot) \,, \tag{5.31}$$

where $r(\mu)$ is the reflection coefficient. Using $I \approx \Phi_{int} + \Psi_{BL}$, the boundary condition on $\zeta = 0$ can be written as

$$\Psi_{BL}(\rho, 0, \mu, \lambda) = -\Phi_{int}(\rho, 0, \mu, \lambda) + r(\mu)\Psi_{BL}(\rho, 0, -\mu, \lambda) + r(\mu)\Phi_{int}(\rho, 0, -\mu, \lambda) + \mathfrak{B}(\rho, \mu, \lambda) \,.$$

Substituting the interior solution (5.27) yields

$$\begin{aligned}\Psi_{BL}(\rho, 0, \mu, \lambda) = &-\phi_0(\rho, 0, \lambda) + 3\kappa\epsilon(\mu\partial_\zeta + \Omega_\perp \cdot \nabla_\perp)\phi_0(\rho, 0, \lambda) + r(\mu)\Psi_{BL}(\rho, 0, -\mu, \lambda) \\ &+ r(\mu)\phi_0(\rho, 0, \lambda) - 3\kappa\epsilon r(\mu)\left[-\mu\partial_\zeta + \Omega_\perp \cdot \nabla_\perp\right]\phi_0(\rho, 0, \lambda) + \mathfrak{B}(\rho, \mu, \lambda) \quad \text{at} \quad \zeta = 0 \,.\end{aligned} \tag{5.32}$$

where we have used the operator identity

$$\Omega \cdot \nabla \equiv \mu\partial_\zeta + \Omega_\perp \cdot \nabla_\perp \,, \tag{5.33}$$

where $\nabla_\perp$ denotes the gradient on the tangent place of $\partial\mathfrak{D}$.

We now introduce the stretched variable $\zeta = \epsilon\zeta^*$. Substituting (5.30) into (5.6) and using (5.33) with the stretched variable gives

$$\mu\frac{\partial\Psi_{BL}}{\partial\zeta^*} + \epsilon\Omega_\perp\nabla_\perp\Psi_{BL} + \epsilon^2\alpha f_a\Psi_{BL} + (1-\epsilon^2)\alpha f_a\mathcal{L}\Psi_{BL} = 0, \tag{5.34}$$

We seek a solution of (5.34) as $\epsilon \to 0^+$. For fixed ζ, this means that $\zeta^* \to \infty$. Therefore, the boundary layer problem is defined in the half space $\zeta^* > 0$. Due to asymptotic matching, a necessary condition to ensure a bounded solution is

$$\Psi_{BL} \to 0 \quad \text{as} \quad \zeta^* \to \infty. \tag{5.35}$$

Similar to the interior solution, we seek a solution in the boundary layer of the form

$$\Psi_{BL}(\rho, \epsilon\zeta^*, \mu, \Omega_\perp, \lambda) = \psi_0 + \epsilon\psi_1 + \mathcal{O}(\epsilon^2). \tag{5.36}$$

Substituting (5.36) into (5.34) and collecting the $\mathcal{O}(1)$ and $\mathcal{O}(\epsilon)$ terms, gives the following equations in $\zeta^* > 0$

$$\mu\frac{\partial\psi_0}{\partial\zeta^*} + \alpha f_a \mathcal{L}\psi_0 = 0\,, \tag{5.37}$$

$$\mu\frac{\partial\psi_1}{\partial\zeta^*} + \alpha f_a \mathcal{L}\psi_1 = \Omega_\perp \cdot \nabla_\perp \psi_0\,. \tag{5.38}$$

Substituting (5.36) into the boundary conditions (5.32) and collecting the $\mathcal{O}(1)$ and $\mathcal{O}(\epsilon)$ terms, gives the following equations on $\zeta^* = 0$

$$\psi_0(\rho,0,\mu,\Omega_\perp,\lambda) = r(\mu)\psi_0(\rho,0,-\mu,\Omega_\perp,\lambda) - [1-r(\mu)]\phi_0(\rho,0,\lambda) + \mathfrak{B}(\rho,\mu,\lambda), \tag{5.39}$$

$$\begin{aligned}\psi_1(\rho,0,\mu,\Omega_\perp,\lambda) &= r(\mu)\psi_1(\rho,0,-\mu,\Omega_\perp,\lambda) + 3\kappa[1+r(\mu)]\mu\frac{\partial\phi_0(\rho,0,\lambda)}{\partial\zeta^*} \\ &+ 3\kappa[1-r(\mu)]\Omega_\perp\nabla_\perp\phi_0(\rho,0,\lambda).\end{aligned} \tag{5.40}$$

Since the operators in Eq. (5.37) and the boundary condition (5.39) are all axisymmetric, the leading order solution ψ_0 does not depend on $\Omega_\perp$. Hence, $\psi_0 = \psi_0(\rho,\zeta^*,\mu,\lambda)$. In addition, we can integrate (5.38) with respect to φ [see also Eq. (5.30)] and observe that the term on the right-hand side vanishes. As the boundary condition (5.39) is axisymmetric, and the solution exists and is unique, it follows that ψ_1 does not depend on φ. As a consequence, Ψ_{BL} satisfies the following boundary value problem

$$\mu\frac{\partial\Psi_{BL}}{\partial\zeta^*} + \alpha f_a \mathcal{L}\Psi_{BL} = 0 \quad \text{in} \quad \zeta^* > 0, \tag{5.41a}$$

with the boundary conditions

$$\Psi_{BL}(\rho,0,\mu,\lambda) - r(\mu)\Psi_{BL}(\rho,0,-\mu\lambda) = \mathcal{S}(\rho,\mu,\lambda)\,, \quad \text{on } 0<\mu\leq 1\,, \tag{5.41b}$$

where the non-homogeneous terms are

$$\mathcal{S}(\rho,\mu,\lambda) \equiv -[1-r(\mu)]\phi_0(\rho,0,\lambda) + 3[1+r(\mu)]\mu\kappa\frac{d\phi_0}{d\zeta^*}(\rho,0,\lambda) + \mathfrak{B}(\rho,\mu,\lambda)\,. \tag{5.41c}$$

5.2 Boundary layer problem for a plane-parallel slab

Here, we apply the foregoing theory to find the boundary layer solutions in the case of an axisymmetric plane-parallel slab (see Figure 5.2).

In the axisymmetric case, $\Psi_{BL} = \Psi_{BL}(\zeta^*,\mu,\lambda)$. The reemission operator can be written as

$$\mathcal{L}\Psi_{BL} = \Psi_{BL} - \frac{1}{2}\frac{f_r(\lambda)}{f_a(\lambda)}\int_\Lambda\int_{-1}^{1} p_0(\mu,\mu')f_a(\lambda')\Psi_{BL}d\mu' d\lambda'\,, \tag{5.42}$$

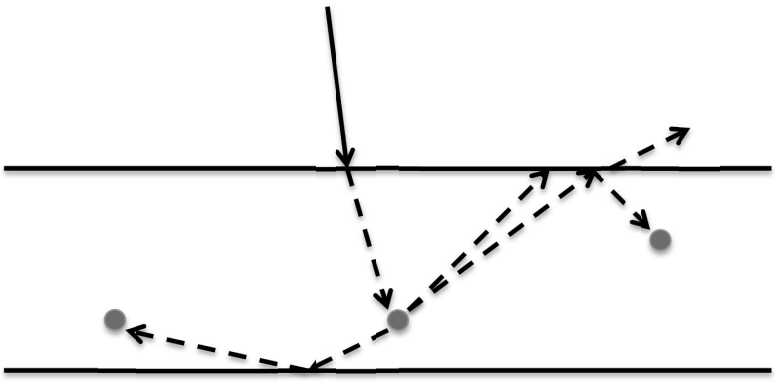

Figure 5.2: A plane-parallel slab with a reflecting bottom surface at $z = z_1$ and transparent top surface at $z = 0$.

where $p_0(\mu, \mu')$ is the redistribution function for the Henyey-Greenstein scattering, *i.e.*,

$$p_0(\mu, \mu') = \frac{1}{2\pi} \int_{-\pi}^{\pi} P_r \left(\mu\mu' + \sqrt{1-\mu^2}\sqrt{1-\mu'^2}\cos(\varphi - \varphi') \right) d(\varphi - \varphi') \, . \tag{5.43}$$

$p_0(\mu, \mu')$ determines the fraction of light from a cone of angle μ' that is reemitted into a cone of angle μ. It can also be expressed as

$$p_0(\mu, \mu') = \frac{2}{\pi} \frac{1-g^2}{\sqrt{\gamma_1 + \gamma_2}(\gamma_1 - \gamma_2)} E(k) \, , \tag{5.44}$$

where

$$\gamma_1 = 1 + g^2 - 2g\mu\mu', \ \gamma_2 = 2g\sqrt{1-\mu^2}\sqrt{1-\mu'^2}, \ k = \frac{2\gamma_2}{\gamma_1 + \gamma_2}, \tag{5.45}$$

and $E(k)$ is the complete elliptic integral of the second kind.

5.2.1 Plane wave solutions

To solve the boundary layer problem (5.41), we use the method of plane waves (cf. [83]). The first step in this approach is to find the plane wave solutions in the whole space and the associated spectrum. To do this, we make the ansatz

$$\Psi_{BL}(\zeta^*, \mu, \lambda) = V(\mu, \lambda) e^{\eta \zeta^*} \, , \tag{5.46}$$

where η and $V(\mu, \lambda)$ are eigenvalues and eigenfunctions, respectively. Substituting (5.46) into (5.41a) gives the generalized eigenvalue problem

$$\mu\eta V(\mu, \lambda) + \alpha f_a(\lambda) \mathcal{L} V(\mu, \lambda) = 0 \, . \tag{5.47}$$

It is convenient to discretize the problem. This helps both to obtain the asymptotic boundary conditions for the DA and also to compute the spectrum of the plane waves. In particular, the $\mathcal{L}$ operator (5.42) is discretized using Gauss-Legendre quadrature rule as

$$\int_{-1}^{1} p_0(\mu,\mu';g)V(\mu,\lambda)d\mu' \approx \sum_{j=-M}^{M} p_0(\mu_j,\mu'_j)V(\mu_j,\lambda)w'_j \tag{5.48}$$

where respectively μ'_j and w'_j are the quadrature abscissas and weights, and M is the number of roots of Legendre polynomials. Additionally, we assume that the Λ is discretized into N equally spaced nodes and use the Simpson quadrature formula, written as

$$\int_{\Lambda} V(\mu,\lambda')d\lambda' \approx \sum_{\ell=1}^{N} V(\mu,\lambda_\ell)q_\ell \tag{5.49}$$

where q_js are the corresponding weights. Using (5.48) and (5.49) in (5.42) and substituting into the eigenvalue problem (5.47) leads to the discrete generalized eigenvalue problem

$$\left(\mu_j\eta_j + \alpha f_a^\ell\right) V_{j,\ell} = \alpha\frac{f_r^\ell}{f_a^\ell}\sum_{\ell=1}^{N} f_a^\ell \sum_{j=-M}^{M} p_0(\mu_j,\mu'_j;g)V_{j,\ell}w'_j q_\ell, \tag{5.50}$$

where $V_{j,\ell} = V(\mu_j,\lambda_\ell)$, $f_a^\ell = f(\lambda_\ell)$, and $f_r^\ell = f_r(\lambda_\ell)$.

It is can be observed that the pairs of $[\eta, V(\mu,\lambda)]$ and $[-\eta, V(-\mu,\lambda)]$ satisfy the same equation (5.41a). Therefore, the plane wave solutions have the symmetry property,

$$\eta_j = \eta_{-j}\ , \quad V_{-j}(\mu,\lambda) = V_j(-\mu,\lambda), \quad j = 0,\ldots,M.$$

Hence, the eigenvalues can be ordered as

$$\cdots < \eta_{-j} < \cdots < \eta_{-1} < \eta_0 < \eta_1 < \cdots < \eta_j < \ldots, \tag{5.51}$$

where $\eta_0 = 0$ corresponds to a constant eigenfunction V_0 [84].

5.2.2 Green's functions for the boundary layer problem

The **whole space** Green's function $G(\zeta^*,\mu,\lambda;\mu',\zeta')$ corresponding to (5.41a) satisfies

$$\mu\frac{\partial G}{\partial\zeta^*} + \alpha f_a(\lambda)\mathcal{L}G = \delta(\mu-\mu')\delta(\zeta^*-\zeta'), \quad \mu\in[-1,1], \zeta^*,\zeta'\in(-\infty,\infty)\ . \tag{5.52}$$

The solution of (5.52) can be obtained using the plane wave solutions as follows

$$G(\zeta^*,\mu,\lambda;\zeta',\mu') = \begin{cases} \sum\limits_{j\geq 0} V_j(\mu,\lambda)e^{\eta_j(\zeta^*-\zeta')}V_j(\mu',\lambda), & \zeta^* < \zeta' \\ \sum\limits_{j\geq 0} W_j(\mu,\lambda)e^{-\eta_j(\zeta^*-\zeta')}W_j(\mu',\lambda), & \zeta^* > \zeta'\ , \end{cases} \tag{5.53}$$

where V_j are the eigenfunctions and $W_j \equiv V_{-j}$.

Next, we introduce the Green's function for (5.41a) in the **upper-half space** $H^0(\zeta^*, \mu, \lambda; \zeta', \mu')$, which satisfies

$$\mu \frac{\partial H^0}{\partial \zeta^*} + \alpha f_a(\lambda) \mathcal{L} H^0 = \delta(\mu - \mu')\delta(\zeta^* - \zeta'), \quad \mu \in (0,1], \zeta^* > 0 \,, \tag{5.54a}$$

$$H^0(0, \mu, \lambda; \zeta', \mu') = r(\mu) H^0(0, -\mu, \lambda; \zeta', \mu'), \quad 0 < \mu \leq 1 \,, \tag{5.54b}$$

where (5.54b) corresponds to the homogeneous (left-hand side) part of (5.41b) on the top surface. The solution of (5.54a) can be expressed in terms of the the whole space Green's function as

$$H^0(\zeta^*, \mu, \lambda; \zeta', \mu') = G(\zeta^*, \mu, \lambda; \zeta', \mu') - \tilde{G}(\zeta^*, \mu, \lambda; \zeta', \mu'), \tag{5.55}$$

where $\tilde{G}(\zeta^*, \mu, \lambda; \zeta', \mu')$ satisfies the problem

$$\mu \frac{\partial \tilde{G}}{\partial \zeta^*} + \alpha f_a(\lambda) \mathcal{L} \tilde{G} = 0, \tag{5.56a}$$

$$\tilde{G}(0, \mu, \lambda; \zeta', \mu') = G(0, \mu, \lambda; \zeta', \mu') \,. \tag{5.56b}$$

The solution of (5.56) can be obtained as a series of plane waves. Combining it with Eqs. (5.53) and (5.55) yields

$$H^0(\zeta^*, \mu, \lambda; \zeta', \mu') = \begin{cases} \sum\limits_{j \geq 0} V_j e^{\eta_j (\zeta^* - \zeta')} V_j' - \sum\limits_{j \geq 0} W_j e^{\eta_j \zeta^*} \sum\limits_{p > 0} C_{j,p} V_p' e^{-\eta_p \zeta'}, \zeta^* < \zeta' \\ \sum\limits_{j \geq 0} W_j e^{-\eta_j (\zeta^* - \zeta')} W_j' - \sum\limits_{j \geq 0} W_j e^{\eta_j \zeta^*} \sum\limits_{p > 0} C_{j,p} V_p' e^{-\eta_p \zeta'}, \zeta^* > \zeta', \end{cases} \tag{5.57}$$

where $C_{j,p}$ are constants, and $V_j = V_j(\mu, \lambda)$, $V_j' = V_j'(\mu', \lambda)$, $W_j = W_j(\mu, \lambda)$, $W_j' = W_j'(\mu', \lambda)$.

Substituting (5.57) into the boundary condition (5.54b) yields the linear system of equations for the constants $C_{j,p}$,

$$\sum_{j \geq 0} \left[W_j(\mu, \lambda) - r(\mu) V_j(\mu, \lambda) \right] C_{j,p} = \left[V_p(\mu, \lambda) - r(\mu) W_p(\mu, \lambda) \right], \quad 0 < \mu \leq 1, \; p > 0 \,. \tag{5.58}$$

The solution of the upper-half space problem is

$$\Psi_{BL}^0(\zeta^*, \mu, \lambda) = \int_0^1 H^0(\zeta^*, \mu, \lambda; 0, \mu') \mathcal{S}(\mu', \lambda) \mu' d\mu' \,, \tag{5.59}$$

where $\mathcal{S}(\mu', \lambda)$ are the non-homogeneous terms in the boundary condition (5.41b). It fol-

lows from (5.57) and (5.59) that

$$\Psi^0_{BL}(\zeta^*,\mu,\lambda) = \sum_{j\geq 0} W_j(\mu,\lambda) e^{-\eta_j \zeta^*} \int_0^1 \left[W_j(\mu',\lambda) + \sum_{p>0} C_{j,p} V_p(\mu',\lambda) \right] \mathcal{S}(\mu',\lambda)\mu' d\mu' \,. \tag{5.60}$$

Similarly, the same approach yields the Green's function in the **lower-half space**, which, due to the symmetries of the problem, can be written as

$$H^1(\zeta^*,\mu,\lambda;\zeta',\mu') = H^0(\zeta_1-\zeta^*,-\mu,\lambda;\zeta_1-\zeta',\mu') \,, \quad \mu\in[-1,0),\ \zeta^*<\zeta_1 \,, \tag{5.61}$$

where $\zeta_1 \equiv z_1/\epsilon$.

5.2.3 Asymptotic boundary conditions

Recall that the asymptotic matching conditions requires that Ψ_{BL} decay to zero as $\zeta^* \to \infty$ [Eq. (5.35)]. The only non-decaying term in (5.60) is the one corresponding to the zero eigenvalue with a constant solution ($j = 0$). Hence, it follows from (5.60) that a necessary condition to satisfy (5.35) is

$$\mathcal{P}\left[\mathcal{S}(\mu,\lambda)\right] \equiv \int_0^1 \left[W_0(\mu',\lambda) + \sum_{p>0} C_{0,p} V_p(\mu',\lambda) \right] \mathcal{S}(\mu',\lambda)\mu' d\mu' = 0 \,. \tag{5.62}$$

Using (5.62) and (5.41c), the following conditions ensure the asymptotic matching condition (5.35),

$$\mathcal{P}\left[\mathfrak{B}(\mu,\lambda) - (1-r(\mu))\,\phi_0(0,\lambda) + 3\epsilon\kappa\mu\,(1+r(\mu))\,\frac{\partial}{\partial\zeta^*}\phi_0(0,\lambda) \right] = 0. \tag{5.63}$$

Using (5.63), the general boundary conditions for the diffusion equation (5.26) are

$$\begin{aligned} a\phi_0 - b\hat{n}\cdot\nabla\phi_0 &= \mathcal{B}_0 \,, && \text{(5.64a)}\\ \mathcal{B}_0 &= \mathcal{P}[\mathfrak{B}(\mu,\lambda)] \,, && \text{(5.64b)}\\ a &= \mathcal{P}[1-r(\mu)] && \text{(5.64c)}\\ b &= 3\epsilon\kappa\mathcal{P}[\mu(1+r(\mu))] \,. && \text{(5.64d)} \end{aligned}$$

We remark that many studies in the optics / physics literature have suggested various ways of choosing these boundary conditions (cf. [85–87] and references therein). The advantage of boundary conditions (5.64) is that they are asymptotically accurate for (5.26) to $\mathcal{O}(\epsilon)$.

5.2.4 Interior solution

In the interior layer, using (5.26) and (5.64) gives the boundary value problem for the interior of the slab as

$$\kappa\frac{\partial^2\phi_0}{\partial z^2} - \alpha f_a(\lambda)\phi_0 = 0 \quad \text{in } 0 < z < z_1, \tag{5.65a}$$

$$a\phi_0 - b\frac{\partial\phi_0}{\partial z} = \mathcal{B}_0 \quad \text{on } z = 0, \tag{5.65b}$$

$$a\phi_0 + b\frac{\partial\phi_0}{\partial z} = 0 \quad \text{on } z = z_1. \tag{5.65c}$$

The solution of (5.65) is

$$\phi_0(z,\lambda) = c_1\cosh(mz) + c_2\sinh(mz), \tag{5.66}$$

where the coefficients are

$$c_1 = \frac{\mathcal{B}_0}{c_0}[a\sinh(mz_1) + mb\cosh(mz_1)], \tag{5.67a}$$

$$c_2 = -\frac{\mathcal{B}_0}{c_0}[a\cosh(mz_1) + mb\sinh(mz_1)], \tag{5.67b}$$

$$c_0 = (a^2 - m^2b^2)\sinh(mz_1) + 2mba\cosh(mz_1)\ , \tag{5.67c}$$

$$m^2 = \frac{\alpha f_a(\lambda)}{\kappa}\ . \tag{5.67d}$$

Substituting (5.66) - (5.67) into (5.27), yields the asymptotically accurate interior layer solution as

$$\Phi_{int} \sim [c_1 - \mu\epsilon 3\kappa m c_2]\cosh(mz) + [c_2 - \mu\epsilon 3\kappa m c_1]\sinh(mz)\ . \tag{5.68}$$

5.2.5 Boundary layer solution

To find the boundary layer solution, we assume that the incident beam on the top surface is collimated and is directed perpendicular to the top surface, *i.e.*, in term of (5.41c),

$$\mathfrak{B}(\mu,\lambda) = \delta(\mu - 1)\ . \tag{5.69}$$

Using (5.59) and (5.69) yields boundary layer solution near the top surface

$$\Psi^0_{BL}(z,\mu,\lambda) = -\phi_0(0,\lambda)\int_0^1 H^0(0^-,\mu,\lambda;0^+,\mu')[1 - r(\mu')]\mu' d\mu' \tag{5.70}$$

$$+3\epsilon\kappa\frac{d\phi_0(0,\lambda)}{dz}\int_0^1 H^0(0^-,\mu,\lambda;0^+,\mu')[1 + r(\mu')]\mu'^2 d\mu' + H^0(0^-,\mu,\lambda;0^+,1)\ .$$

Similarly, using (5.61) yields the boundary layer solution near the bottom surface

$$\Psi^1_{BL}(z,\mu,\lambda) = \phi_0(z_1,\lambda)\int_{-1}^{0} H^0(0^-,-\mu,\lambda;0^+,-\mu')[1-r(\mu')]\mu' d\mu' \quad (5.71)$$

$$-3\epsilon\kappa\frac{d\phi_0(z_1,\lambda)}{dz}\int_{-1}^{0} H^0(0^-,-\mu,\lambda;0^+,-\mu')[1+r(\mu')]\mu'^2 d\mu' \ .$$

The solution of the full problem is then

$$I = \Phi_{int} + \Psi^0_{BL} + \Psi^1_{BL} \ . \quad (5.72)$$

5.3 Physical investigations

Below we perform a series of computational experiments of the LRTE and DABL. The LRTE is solved using the methods presented in Section 5.2.1. The purpose of these investigations is two-fold: to validate the asymptotics and garner physical insight into the salient features of the solutions. In particular, our goal is to capture accurately the reabsorption effects.

5.3.1 Reabsorption effects

To recap, light that is absorbed is reemitted at a different wavelength. The reemitted light can be reabsorbed with probability of the quantum yield, *i.e.*, $0 < \mathrm{QY} < 1$. Hence, qualitatively, the loss of light (photons) increases as QY^n after n reabsorption events. However, the degree or this loss also depends on the **Stokes shift** (*i.e.*, reabsorption cross-section), $\Delta\lambda_S$, which is characteristic wavelength separation between the absorption and reemission spectra. Reabsorption is particular to fluorescence (as opposed to elastic scattering). Modeling the reabsorption accurately is one of the goals of this study.

To illustrate reabsorption, Figure 5.3 shows "synthetic" absorption and reemission spectra (probability distribution functions), chosen as

$$f_r(\lambda) = \frac{e^{-(\lambda-\lambda_r)^2/2\sigma^2}}{\sigma\sqrt{2\pi}}, \quad f_a(\lambda) = \frac{e^{-(\lambda-\lambda_a)^2/2\sigma^2}}{\sigma\sqrt{2\pi}}, \quad (5.73)$$

where λ_a and λ_r are the central absorption and reemission wavelengths, respectively, and σ is the characteristic width of these spectra. The Stokes shift can be defined as

$$\Delta\lambda_S = \lambda_r - \lambda_a \ . \quad (5.74)$$

In all our computations we choose a slab with $z = 0$ and $z_1 = 1$ and the relative refractive index as $n_{rel} = 1.4$. We use the Fresnel reflection coefficient for unpolarized

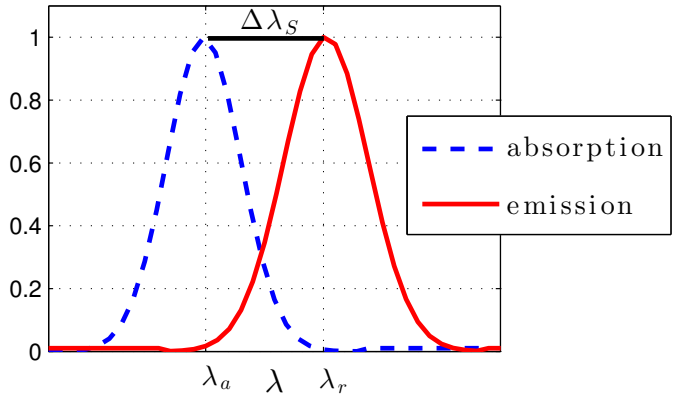

Figure 5.3: Schematic absorption (dashes) and reemission (solid) spectra. $\Delta\lambda = \lambda_r - \lambda_a$ denotes the Stokes shift.

light, given by

$$r(\mu) = \begin{cases} \frac{1}{2} \mid \frac{(n_{rel}\mu_t - \mu)}{(n_{rel}\mu_t + \mu)} \mid^2 + \frac{1}{2} \mid \frac{(n_{rel}\mu - \mu_t)}{(n_{rel}\mu + \mu_t)} \mid^2, & \mu > \mu_c \\ 1, & \mu \leq \mu_c \end{cases} \tag{5.75}$$

where the cosine angle of the transmitted radiation is

$$\mu_t = \sqrt{1 - n_{rel}^2(1 - \mu^2)}$$

and the cosine of the critical angle is $\mu_c = \sqrt{1 - 1/n_{rel}^2}$.

Below we study the reabsorption effects in the LRTE and DABL for varying the Stokes shifts. We show that DABL is accurate when the Stokes shift is small. When the Stokes shift is large, DABL is, in general, not asymptotically valid. However, its results are still qualitatively accurate for wavelengths in the reemission range.

Small Stokes shift

Here, we study the case of a small Stokes shift. When $\Delta\lambda_S \ll \sigma$, there is a large overlap between f_a and f_r, *i.e.*, the reabsorption cross section is large. In this case, the probability for reabsorption is high. This is typical for organic fluorescent particles, such as Rhodamine B (cf. [37]). In the computations below, we use (5.73) with $\lambda_a = 545, \lambda_r = 590$, and $\sigma = 150$. Therefore, the Stokes shift is small, *i.e.*, $\Delta\lambda_S \approx \frac{\sigma}{3}$.

First, we choose $\epsilon = 0.01$ and consider a forward peaked scattering phase function (5.44) with an anisotropy factor $g = 0.8$. Figure 5.4 shows that radiance on the top surface as a function of the direction μ computed using LRTE and DABL. This computation shows that DABL is very accurate. To understand this behavior of the radiance, we

recall that the source is a collimated beam on the top surface pointing downwards, *i.e.*, in the $\mu = 1$ direction. Since the medium is highly diffusive, much of the the radiance is backscattered from the medium to the top surface, which is consistent with the roughly constant radiance in the range $-1 \leq \mu < 0.7$. However, much of the forward peaked radiation gets transmitted outside of the medium, which is consistent with the dip of the radiance at the top surface in the range $0.7 < \mu \leq 1$.

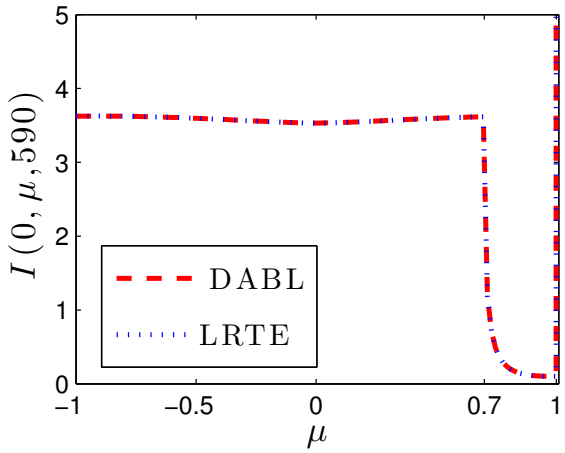

Figure 5.4: The radiance on the top surface a function of μ computed directly using the LRTE (dots) and DABL (dashes). Here $\epsilon = 0.01, g = 0.8, \lambda_a = 545, \lambda_r = 590$, and $\Delta\lambda_S \approx \frac{\sigma}{3}$.

To quantify the accuracy of DABL, we use the reflectance outside of the top surface and the transmittance outside of the bottom surface, defined respectively as

$$\mathbf{R} = -\int_{-1}^{0} [1 - r(\mu)] I(0, \mu, \lambda) \mu d\mu, \tag{5.76}$$

$$\mathbf{T} = \int_{0}^{1} [1 - r(\mu)] I(z_1, \mu, \lambda) \mu d\mu \, . \tag{5.77}$$

The respective relative errors of DABL are defined as

$$\|E_{\mathbf{R}}\|_\infty = \frac{\|\mathbf{R}_{LRTE} - \mathbf{R}_{DABL}\|_\infty}{\|\mathbf{R}_{LRTE}\|_\infty}, \quad \|E_{\mathbf{T}}\|_\infty = \frac{\|\mathbf{T}_{LRTE} - \mathbf{T}_{DABL}\|_\infty}{\|\mathbf{T}_{LRTE}\|_\infty}. \tag{5.78}$$

where $\|\cdot\|_\infty$ is the L^∞ norm.

It is interesting to study the behavior of the solutions and errors as ϵ varies. Figure 5.5(a) shows that the reflectance decreases and transmittance increases as ϵ increases. To understand this, recall that as ϵ increases, the fluorescence (reemission term) becomes larger [see Eq. (5.6)]. Since, in addition, the fluorescence is highly forward peaked ($g = 0.8$), as ϵ increases it is expected that the transmittance will increase and the reflectance

will decrease. Figure 5.5(b) shows the error of DABL *vs.* the LRTE as functions of ϵ. This result shows that the error of DABL scales as ϵ^2. Hence, this result shows that the accuracy of DABL is consistent with the asymptotic theory.

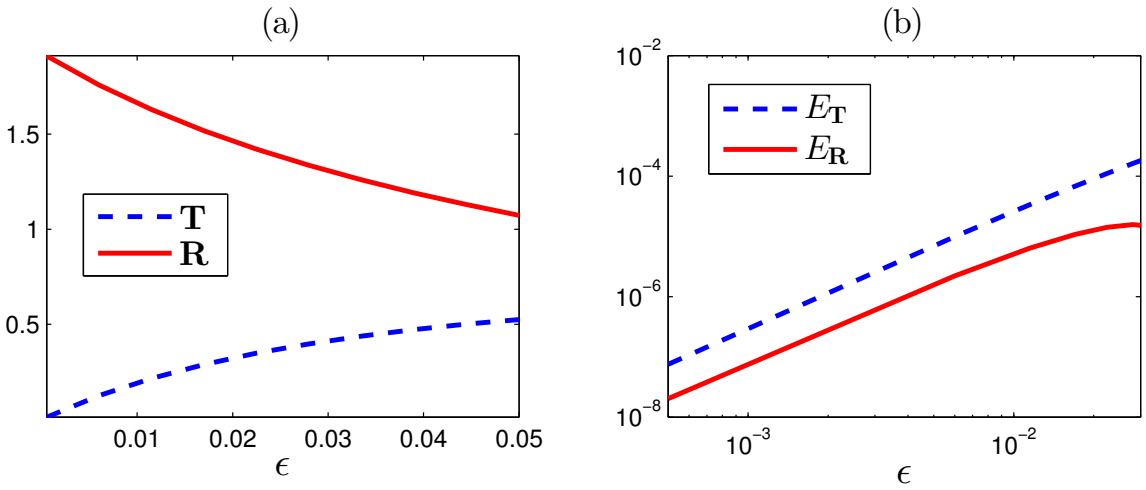

Figure 5.5: (a) Reflectance [Eq. (5.76), solid] and transmittance [Eq. (5.77), dashes] evaluated at $\lambda = 590$ as functions of ϵ. All other parameters are the same as in Figure 5.4. (b) Loglog plot of the relative errors [Eq. (5.78)].

Another interesting study is to seek the effect of anisotropy of the reemission phase function (5.2). To do so, we vary the anisotropy factor from $g = 0$ (isotropic) to $g = 1$ (forward peaked reemission). Figure 5.6(a) shows that the reflectance decreases and transmittance increases as the reemission becomes more forward peaked. Figure 5.6(b) shows the associated errors of reflectance and transmittance as a function of anisotropy factor. Both errors are found to be in the order of ϵ^2.

Large Stokes shift

It is also interesting to study the case of large Stokes shifts. In this case, the reabsorption cross-section is small and, therefore, the probability of reabsorption is small. This can be attained using fluorescent semiconductor particles, such as CdSe / CdTe (cf. [22]).

To study this case, we use (5.73) with $\lambda_a = 540, \lambda_r = 690, \sigma = 150$. This corresponds to a Stokes shift (5.74) $\Delta\lambda_S = \sigma$, *i.e.*, almost no overlap between f_a and f_r. In this case it is meaningful to define the absorption and reemission wavelength ranges, Λ_a and Λ_r, respectively.

Figure 5.7 shows that DABL is generally inaccurate in this case. In particular, Figure 5.7(a) shows that at $\lambda = 540$, *i.e.*, in the absorption range, DABL is inaccurate for all μ. On the other hand Figure 5.7(b) shows that at $\lambda = 690$, *i.e.*, the the reemission range, DABL is accurate for $0.7 < \mu \leq 1$. To understand this, it is important to note that since f_a and f_r decay to zero, the assumptions in (1) do not hold in general. In particular, since $f_r/f_a = o(\epsilon)$ in at least part of the absorption range, it follows from (5.4) that $\mathcal{L} = \mathbb{I} + o(\epsilon)$.

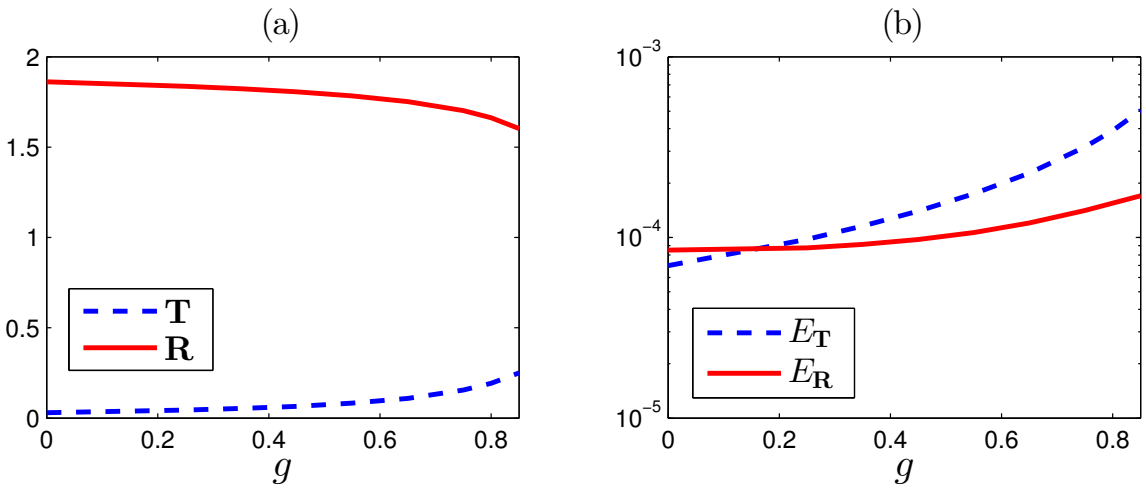

Figure 5.6: (a) Reflectance (solid) and transmittance (dashes) as functions of anisotropy factor g. All other parameters are the same as in Figure 4.1. (b) Semilogy plot of the relative errors.

Therefore, the asymptotic derivation (5.9) does not apply to this case. This explains the failure of the diffusion approximation.

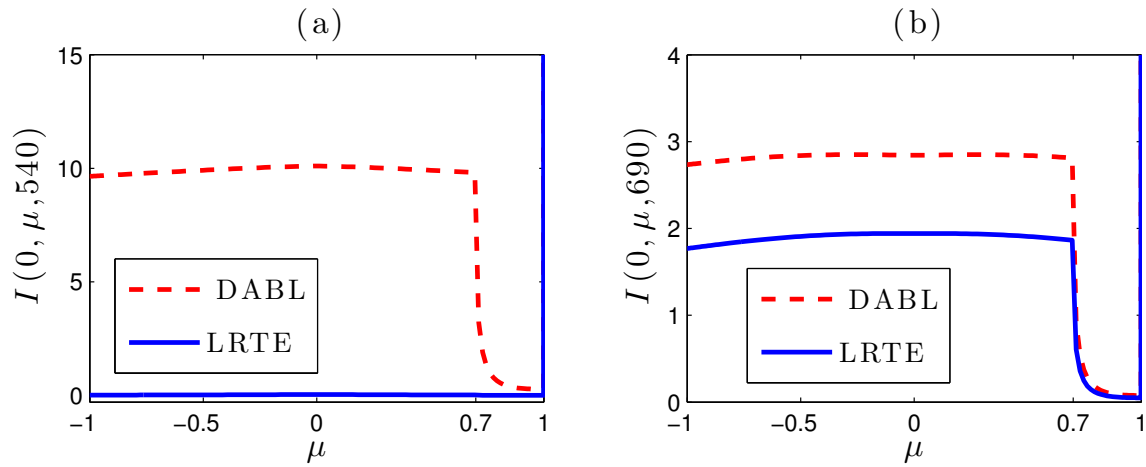

Figure 5.7: The radiance on the top surface as a function of direction evaluated at (a) $\lambda = 540$ and (b) $\lambda = 690$, and computed using the LRTE (solid) and DABL (dashes). The parameters are $\epsilon = 0.01, g = 0.8$ and the Stokes shift is $\Delta\lambda_S = \sigma = 150$.

Furthermore, in the case of a very large Stokes shift, *i.e.*, when the reabsorption is negligible, the original LRTE (4.11) can be broken up into two RTEs in the absorption and

reemission ranges as

$$\Omega \cdot \nabla I + \mu_a f_a(\lambda) I = 0 \,, \quad \lambda \in \Lambda_a \,, \tag{5.79a}$$

$$\Omega \cdot \nabla I = \mu_a Q Y f_r(\lambda) \int_{\Lambda_a} \int_{S^2} f_a(\lambda') P_r(\Omega \cdot \Omega') I(\mathbf{x}, \Omega', \lambda') \, d\Omega' d\lambda', \quad \lambda \in \Lambda_r \,. \tag{5.79b}$$

We remark that coupled RTEs for the absorption and reemission (also known as excitation and fluorescence, respectively) – and associated coupled diffusion approximation equations – have appeared in the optics / physics / biomedical literature, (cf. [9–14]). Some of those coupled equations have relied on effective coupling constants. Strictly speaking, the system (5.79) is physically correct only when the reabsorption is small.

Moreover, as mentioned above, the diffusion approximation is not asymptotically valid in this case. This can be understood from the system (5.79). The solution of (5.79a) in a parallel slab with the same boundary conditions as in Section 5.2 is

$$I(z, \mu, \lambda) \;\; = \begin{cases} \delta(\mu - 1) \left[1 + r^2(\mu) e^{-2\mu_a f_a(\lambda)/\mu}\right]^{-1} e^{-\mu_a f_a(\lambda) z/\mu}, & 0 < \mu \leq 1, \\ \delta(\mu - 1) r(\mu) \left[1 + r^2(\mu) e^{-2\mu_a f_a(\lambda)/\mu}\right]^{-1} e^{-\mu_a f_a(\lambda)(z+2)/\mu}, & -1 \leq \mu < 0. \end{cases} \tag{5.80}$$

where $\lambda \in \Lambda_a$ and $z \in [0, 1]$. Using the scaling (1), it follows directly from (5.79a), as well as from (5.80), that, apart from the $\mu = 1$ (forward peaked) direction, the radiance in the absorption range scales as $\mathcal{O}(e^{-1/\epsilon})$, which is consistent with the very small LRTE solution in Figure 5.7(a). A similar analysis shows that DABL is also inaccurate in the reemission range, apart from the forward peaked direction, which is consistent with the results in Figure 5.7(b).

Varying the Stokes shift

Since DABL is, in general, only accurate for small Stokes shifts, it is interesting to study its accuracy as the Stokes shift varies. To do this, we fix $\epsilon = 0.01, g = 0.8, \lambda_r = 690$, and $\sigma = 150$, while allowing λ_a – and hence $\Delta\lambda_S$ – to vary (*i.e.*, $\lambda_a \in [540, 690]$) .

Figure 5.8 shows the error of DABL for variable Stokes shifts computed for the averaged radiance on the top surface at the center of the reemission spectrum, *i.e.*,

$$\|E_S(\lambda_r)\|_\infty = \frac{\|\mathcal{U}_{LRTE} - \mathcal{U}_{DABL}\|_\infty}{\|\mathcal{U}_{LRTE}\|_\infty},$$

where, for either the LRTE or DABL,

$$\mathcal{U}(\lambda_r) = -\int_{-1}^{0} I(0, \mu', \lambda_r) \mu' d\mu' \,. \tag{5.81}$$

This figure shows that for $\Delta\lambda_S < \sigma/3$ the error of DABL is on the order of $\mathcal{O}(\epsilon^2)$, whereas, for $\Delta\lambda_S \geq \sigma$, the error beyond this scaling. This is further indication that the diffusion approximation can become inaccurate whenever the reabsorption is weak, *i.e.*, when the

overlap between f_a and f_r is small.

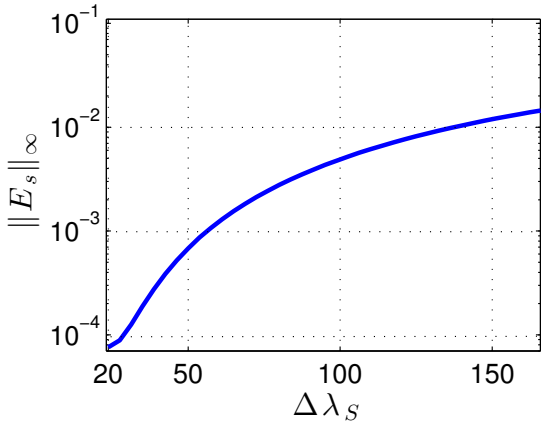

Figure 5.8: Semilogy plot for the relative error in L^∞-norm as a function of Stokes shift. The parameters are $\epsilon = 0.01, g = 0.8$, and $\Delta\lambda_S \in [0, \sigma]$, where $\sigma = 150$.

5.3.2 Using measured luminescent data

To further test the accuracy of DABL, we compute the solutions using measured luminescent data for semiconductor CdSe/CdTe nanoparticles [see Figure 4.6(a)]. Unlike the previously used synthetic spectral data (5.73), here it is less clear how to define the Stokes shift. Nonetheless, over the entire range of wavelengths, the reabsorption cross-section is relatively small due to the large absorptivity at shorter wavelengths. In addition, the source function on the top surface is taken as

$$\mathfrak{B}(\mu, \lambda) = f_{sol}(\lambda)\delta(\mu - 1) \ , \tag{5.82}$$

where $f_{sol}(\lambda)$ is the normalized typical average irradiance spectrum at sea level [[47]], as shown in Figure 4.6(a). Using the parameters $\epsilon = 0.01, g = 0.8$ we compute the solution of the LRTE, DABL, and also the diffusion approximation (DA) without the boundary layer solution but using the asymptotically accurate boundary conditions [see (5.28)].

Figure 5.9(b) shows the radiance on the top surface at $\lambda = 650$ nm, *i.e.*, at the center of the reemission spectrum. This plot shows that DABL is accurate compared with the LRTE. However, the DA is inaccurate. Hence, **this result further indicates the importance of including the asymptotic boundary layer solution near the top surface.** Similar to Figure 5.4, since the medium is highly diffusive, much of the the radiance is backscattered from the medium to the top surface, which is consistent with the roughly constant radiance in the range $-1 \leq \mu < 0.7$. However, much of the forward peaked radiation gets transmitted outside of the medium, which explains the low radiance at the top surface in the range $0.7 < \mu \leq 1$.

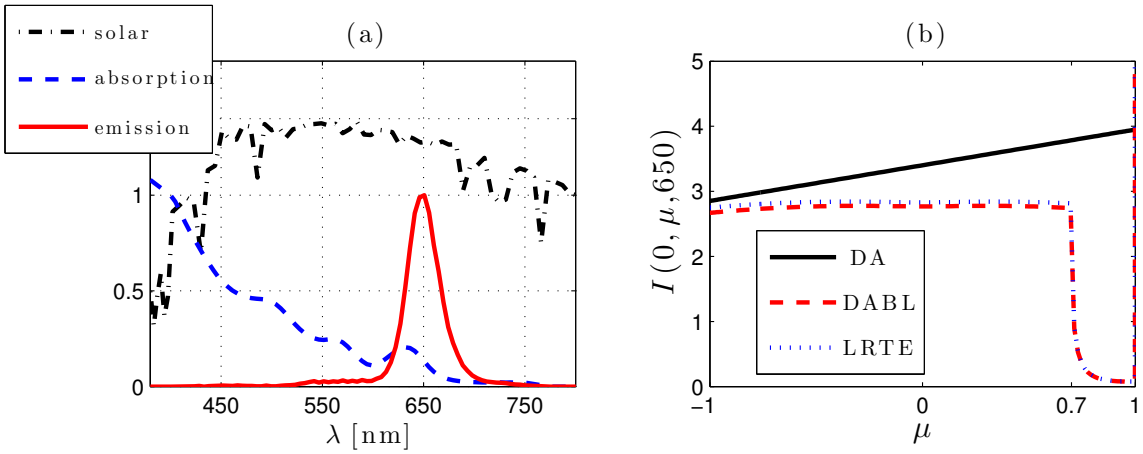

Figure 5.9: (a) Solar irradiance at sea level (dot-dashes), measured absorption (dashes) and measured reemission (solid) spectra of CdSe / CdTe semiconductor nanoparticles [[22]]. (b) Radiance on the top surface at $\lambda = 650$ nm, computed using the DA [see (5.28)], DABL (dashes), and the LRTE (dots). The parameters are $\epsilon = 0.01, g = 0.8$.

Similar to Figure 5.5(a), Figure 5.10(a) shows that the reflectance decreases and the transmittance increases as ϵ increases. However, unlike Figure 5.5(b), Figure 5.10(b) shows that the errors in the reflectance do not scale as $\mathcal{O}(\epsilon^2)$. In fact, the errors appear to scale as $\mathcal{O}(\epsilon)$, though this is not guaranteed by the asymptotic theory. This reduced accuracy due to the small reabsorption, as discussed in Sections 5.3.1 and 5.3.1. Notwithstanding this limitation, these results indicate that DABL can be fairly accurate even beyond its formal regime of validity.

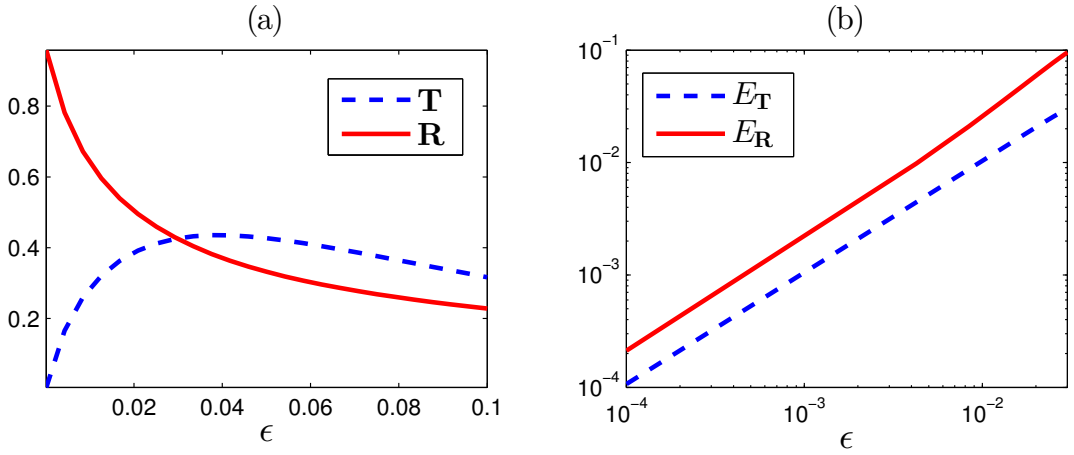

Figure 5.10: Same as Figure 5.5 using the measured data in Figure 5.9 and computed at $\lambda = 650$ nm.

5.4 Summary and Discussions

Light transport in a luminescent medium is studied in highly scattering (optically thick) regime. Using asymptotic matched expansion techniques, the LRTE (4.11) is reduced to the diffusion approximation with associated boundary conditions for the interior of the medium, and the boundary layer solution. This entire solution, *i.e.*, the corrected diffusion approximation (cDA, DABL), is shown to be accurate to $\mathcal{O}(\epsilon)$ globally, where ϵ is the small parameter in the problem. Using accurate numerical computations of the LRTE and DABL, we show that DABL is accurate when the Stokes shift is small. When the Stokes shift is large, DABL is, in general, not asymptotically valid. However, our computations show that, even for a large Stokes shift, DABL can be qualitatively reliable for wavelengths in the reemission range. This is the first detailed study of the reabsorption effects in optically thick media and the accuracy of the diffusion approximation in capturing these effects. The results of this study are encouraging for using DABL to solve these problems. This approach can be a flexible reduction technique for solving other inelastic scattering problems.

Chapter 6

Conclusions and Broader Impacts

In this dissertation, we develop a theoretical and computational framework to study light propagation in random luminescent media. Computational and analytical modeling approaches are studied with the application to solar science.

- A statistical approach MC is applied to model inelastic light scattering in luminescent solar concentrators.
- A deterministic approach radiative transport theory is developed to model inelastic scattering in luminescent media. The governing equation LRTE is studied using analytical and computational methods.
- The numerical and asymptotic solution techniques are used to solve the LRTE in different scattering and absorbing media.
- The computations of LRTE compared with MC and found to agree.
- The LRTE is studied for optically thick media. Using perturbation methods, a reduced (corrected diffusion approximation and boundary conditions) system is derived, and its accuracy is verified.
- Using experimental data, the important LSC loss mechanisms: reabsorption (self-absorption) and escape losses are studied in detail for semiconductor-based LSCS.

Consequently, the LRTE is an effective approach to model these kinds of problems. Beyond the LSC problem, the LRTE is an interesting equation for further analytical and computational studies. In particular, this study gives insightful results to the experimentalists for designing efficient LSCs. The results for semiconductor-based LSCs could be used for the improvement of current solar energy technologies, and this could help improving solar power production in a cost-effective way.

In addition, this research arises various appealing mathematical problems from the modeling perspective. The list of problems below gives a few examples of further developments of this research.

Further Studies

- In this dissertation, polarization effects have been neglected. Including polarization effects for the LRTE and solving the LRTE numerically in multidimensional domain can be useful for many applications.

- In this research, the corrected diffusion approximation has been applied in detail to a slab problem. Extending the corrected diffusion approximation to deal with more general geometries is interesting and useful for LSCs.

- In many cases, the reemitted light is sharply peaked in the forward direction. In that regime, the RTE can then be reduced to a Fokker-Planck partial differential equation (cf. [88–90]). Extending this approach to the LRTE could be computationally advantageous.

- The scattering can be highly peaked in a preferred direction, as in the case of aligned nanorods considered in Chapter 4. It would be interesting to derive from the LRTE a reduced, Fokker-Planck type, approximate PDE in this regime and compare it with the LRTE.

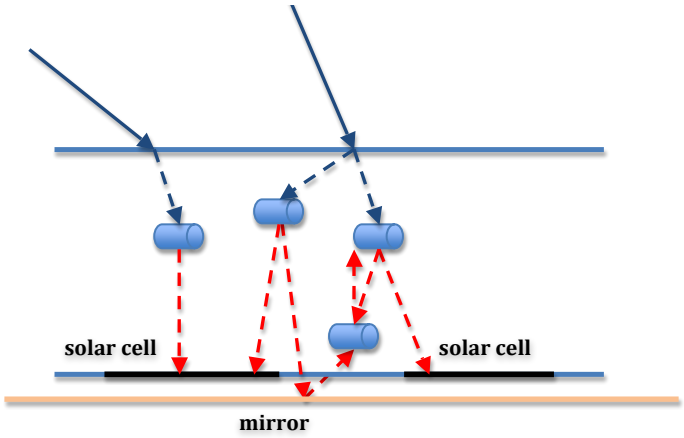

Figure 6.1: An illustration of a thin LSC as a slab, where the medium contains semiconductor nanorods that are aligned parallel to the surface. The solar cells are assumed to be located at the bottom with an aperture opening, and the LSC is located on a mirror where there is an air gap between the LSC medium and mirror.

- An alternative LSC design is to use nanorods that are aligned parallel to the top and bottom surfaces (see Fig. 6.1). These nanorods will scatter light mostly perpendicular to the surface of the LSC. This design could be more efficient. Computationally, the above-mentioned Fokker-Planck type reduced equation could help model this problem. In Fig. 6.1, each solar cell acts as an obstacle that prevents a portion of the light reaching the mirror and reflecting back to the medium. This could help us

developing a new analytical modeling approach, which can be used for more general inelastic scattering problems with partially absorbing and nonplanar obstacles.

Overall, this dissertation presents accurate and insightful results for modeling aspects of light transport in random luminescent media. The proposed modeling approaches can be applied to other problems that arise in real-world applications such as biochemistry, geology, biomedical engineering, and fluorescence tomography.

Appendix A

Solving LRTE numerically

We implement the source iteration method for the LRTE as follows,

$$\begin{aligned}
&\cos\varphi_m \tfrac{\partial}{\partial x} I^{(s)}_{m,\ell} + \sin\varphi_m \tfrac{\partial}{\partial z} I^{(s)}_{m,\ell} + \mu_a f^\ell_a I^{(s)}_{m,\ell} = \\
&\mu_a QY f^\ell_r p_r(\varphi_m; g) \Delta\varphi_m \Delta\lambda_\ell \tfrac{1}{2} I^{(s-1)}_{1,\ell}(x,z,\varphi_1,\lambda_\ell) \times f^\ell_a I^{(s-1)}_{m,1}(x,z,\varphi_m,\lambda_1) f^1_a \\
&+ \mu_a QY f^\ell_r p_r(\varphi_m; g) \times \Delta\varphi_m \Delta\lambda_\ell \textstyle\sum_{\ell=2}^{N_\lambda - 1} \sum_{m'=2}^{N_\varphi - 1} 2 I^{(s-1)}_{m',\ell}(x,z,\varphi_{m'},\lambda_\ell) f^\ell_a \\
&+ \mu_a QY f^\ell_r p_r(\varphi_m; g) \Delta\varphi_m \Delta\lambda_\ell \tfrac{1}{2} I^{(s-1)}_{N_\varphi,\ell}(x,z,\varphi_{N_\varphi},\lambda_\ell) \times f^\ell_a I^{(s-1)}_{m,N_\lambda}(x,z,\varphi_m,\lambda_{N_\lambda}) f^{N_\lambda}_a, \qquad \text{(A.1)}
\end{aligned}$$

where $f^\ell_a = f_a(\lambda_\ell),\ f^\ell_r = f_r(\lambda_\ell)$.

N_φ is total number of uniform angular discretization, $m = 1, \ldots, N_\varphi$. N_λ is total number of uniform spectral discretization, $\ell = 1, \ldots, N_\lambda$. Thus,

$$\Delta\varphi_{m'} = \frac{2\pi}{N_\lambda},\ \Delta\lambda_\ell = \frac{\|\Lambda\|_1}{N_\lambda}.$$

The integral with respect to λ, φ is computed by using Trapezoidal rule. The number of iterations is denoted by s, $s = 0, 1, \ldots$. The source iteration method is used for seeking an iterative solution in the form of

$$I \approx \sum_{s \geq 0} I^{(s)}, \qquad \text{(A.2)}$$

where the initial radiance is $I^{(0)} = 0$.

As a stopping criteria, we consider

$$\|I^{(s)}_{i,j,m,\ell}\|_\infty \leq \Delta \qquad \text{(A.3)}$$

$\Delta = 10^{-5}$. From here, we find the maximum number of iterations which vanishes the

solution. The iterative solution of the radiance will be found by (see also Figure 4.2)

$$\mathbf{I} = \sum_{s=0}^{\text{maxiter}} I^{(s)}_{i,j,m,\ell}. \tag{A.4}$$

The spatial ordering

To solve (A.1) and to find each iterative radiance $I^{(s)}$, we implement the upwinding scheme for the spatial discretization for each corresponding angular domain. Determining the characteristics of the flow with the sign of $\cos\varphi_m,\ \sin\varphi_m$, the angular domain is divided into four quadrants and the upwinding spatial scheme is applied based on the below spatial ordering,

- if $\varphi_m \in [0, \pi/2)$ the spatial index is swept through, in the order of $i = 1, \ldots, N_x$, $j = 1, \ldots, N_z$,
- if $\varphi_m \in [\pi/2, \pi)$ the spatial index is swept through, in the order of $i = N_x, \ldots, 1$, $j = 1, \ldots, N_z$,
- if $\varphi_m \in [\pi, 3\pi/2)$ the spatial index is swept through, in the order of $i = N_x, \ldots, 1$, $j = N_z, \ldots, 1$,
- if $\varphi_m \in [3\pi/2, 2\pi)$ the spatial index is swept through, in the order of $i = 1 \ldots, N_x$, $j = N_z, \ldots, 1$,

Here, the spatial orderings are $i = 1, ..., N_x$,$j = 1, ..., N_z$ for the interior spatial nodes where $x \in [-l_x/2, l_z/2]$, $z \in [-l_z/2, l_z/2]$ (see Figure A.1).

Boundary conditions

The spatial nodes of each boundary are defined as below.

1. PV (vacuum-Dirichlet) BCs: when $j = 1, \ldots, N_z$ for all $\lambda_\ell \in \Lambda$, $k = 1, \ldots, N_\lambda$, on each quadrant:

- *Quadrant I:* for $m1 = 1, \ldots, N_\varphi/4$

$$I^{(s)}_{N_x+1,j,m1,\ell} = I^{(s-1)}_{N_x+1,j,m1,\ell},$$

- *Quadrant II:* for $m2 = N_\varphi/4 + 1, \ldots, N_\varphi/2$

$$I^{(s)}_{N_x+1,j,m2,\ell} = 0,$$

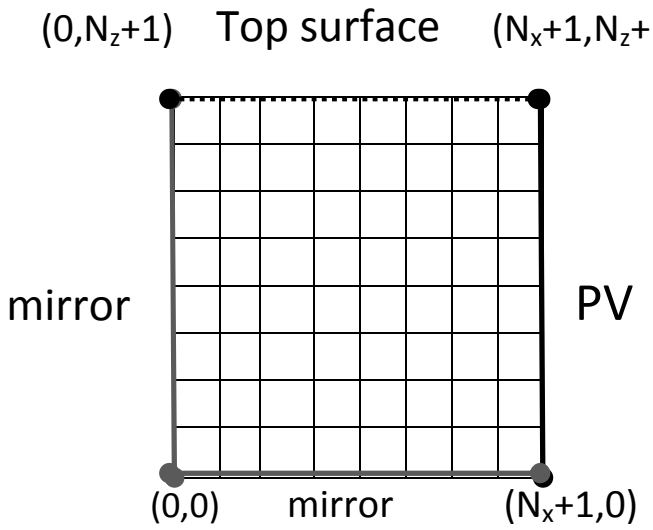

Figure A.1: The 2D schematic representation of LSC

- *Quadrant III:* for $m3 = N_\varphi/2 + 1, \ldots, 3N_\varphi/4 + 1$

$$I^{(s)}_{N_x+1,j,m3,\ell} = 0,$$

- *Quadrant IV:* or $m4 = 3N_\varphi/4 + 2, \ldots, N_\varphi$

$$I^{(s)}_{N_x+1,j,m4,\ell} = I^{(s-1)}_{N_x+1,j,m4,\ell}.$$

2. Top surface (transmission and reflecting) BCs: when $i = 1, \ldots, N_x$, on each quadrant,

- *Quadrant I:* For $s \geq 1$, and for $m1 = 1, \ldots, N_\varphi/4$, , $N_\varphi - m4$ denotes the angular nodes for the reflecting angle where $m4 = 3N_\varphi/4 + 2, \ldots, N_\varphi$,

$$I^{(s)}_{i,N_z+1,m1,\ell} = r_{(N_\varphi - m4)} I^{(s-1)}_{i,N_z+1,N_\varphi - m4,\ell},$$

  $r_{(N_\varphi - m4)}$ is the computed Fresnel reflection coefficient. The reflection angle is computed by $\varphi' = 2\pi - \varphi$ (see also Figure A.3).

- *Quadrant II:* For $s \geq 1$, $m2 = N_\varphi/4 + 1, \ldots, N_\varphi/2$ and $m3 = N_\varphi/2 + 1, \ldots, 3N_\varphi/4 + 1$,

$$I^{(s)}_{i,N_z+1,m2,\ell} = r_{(N_\varphi - m3)} I^{(s-1)}_{i,N_z+1,N_\varphi - m3,\ell},$$

- *Quadrant III:* for $m3 = N_\varphi/2+1, \ldots, 3N_\varphi/4+1$ and $m2 = N_\varphi/4+1, \ldots, N_\varphi/2$,

and $s = 1$,

$$I^{(1)}_{i,N_z+1,m3,\ell} = t_{m3}\mathfrak{B}_{m3,\ell} + r_{(N_\varphi - m2)} I^{(0)}_{i,N_z+1,N_\varphi-m2,\ell}.$$

In the first iteration, there is no internal reflection, ***i.e.***,

$$I^{(0)}_{i,N_z+1,N_\varphi-m2,\ell} = 0.$$

When $s > 1$,

$$I^{(s)}_{i,N_z+1,m3,\ell} = r_{(N_\varphi - m2)} I^{(s-1)}_{i,N_z+1,N_\varphi-m2,\ell}.$$

$\mathfrak{B}_{m3,\ell} = \mathfrak{B}(\varphi_{m3}, \lambda_\ell)$ is the source function which defines the solar irradiance in a particular direction,

$$\mathfrak{B}(\varphi_m, \lambda_\ell) = I_{sol}(\lambda_\ell) e^{-8(\varphi_m - \varphi_i)^2}, \tag{A.5}$$

- *Quadrant IV:* $m4 = 3N_\varphi/4 + 2, \ldots, N_\varphi$ and $m1 = 1, \ldots, N_\varphi/4$, when $s = 1$,

$$I^{(1)}_{i,N_z+1,m4,\ell} = t_{m4}\mathfrak{B}_{m4,\ell} + r_{(N_\varphi - m1)} I^{(0)}_{i,N_z+1,N_\varphi-m1,\ell},$$

when $s > 1$,

$$I^{(s)}_{i,N_z+1,m4,\ell} = r_{(N_\varphi - m1)} I^{(s-1)}_{i,N_z+1,N_\varphi-m1,\ell}.$$

3. Mirror (reflecting) BCs: when $i = 0$, $j = 0, N_z$ (left mirror) or $j = 0$, $i = 1, \ldots, N_x$ (bottom mirror),

- *left mirror BCs:* when $j = 1, \ldots, N_z$,

$$I^{(s)}_{0,j,m2,\ell} = I^{(s-1)}_{0,j,N_\varphi/2-m1,\ell}, \quad I^{(s)}_{0,j,m3,\ell} = I^{(s-1)}_{0,j,N_\varphi/2-m4,\ell}.$$

- *bottom mirror BCs:* when $i = 1, \ldots, N_x$,

$$I^{(s)}_{i,0,m3,\ell} = I^{(s-1)}_{i,0,N_\varphi-m2,\ell}, \quad I^{(s)}_{i,0,m4,\ell} = I^{(s-1)}_{i,0,N_\varphi-m1,\ell}.$$

Upwinding spatial scheme

Now, the the source iteration method is implemented to solve (A.1). by using upwinding spatial scheme for the spatial discreatization.

As a first step, we start from the right top corner (x_{N_x+1}, z_{N_z+1}), where φ_m is in the third quadrant. Sweeping through right to left in x direction and going downward in z direction, the radiance $I^{(s)}_{i,j,m3,\ell}$ is computed. Here, the spatial ordering is $i = N_x, \ldots, 1$, $j = N_z, \ldots, 1$.

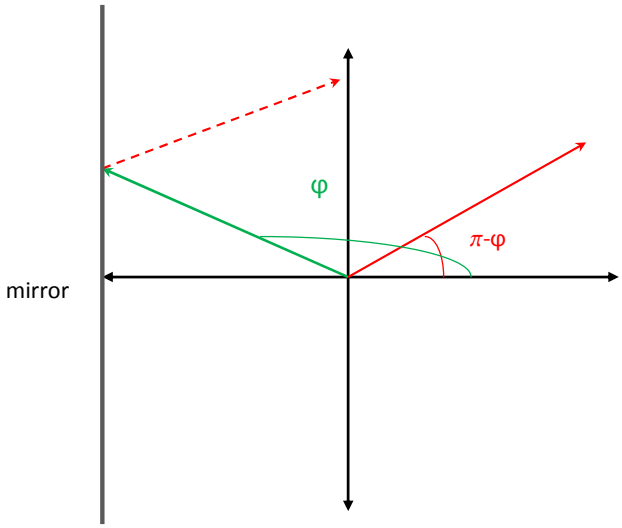

Figure A.2: A schematic representation for the reflection of light from the left mirror, $\varphi' = \pi - \varphi$.

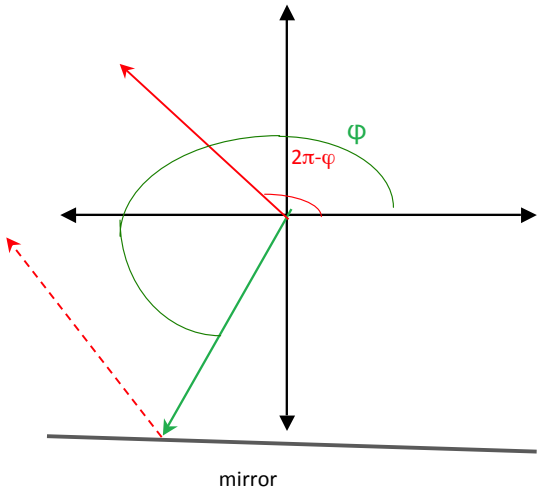

Figure A.3: A schematic representation for the reflection of light from the bottom mirror, $\varphi' = 2\pi - \varphi$.

Then, upwinding scheme is applied to (A.1).

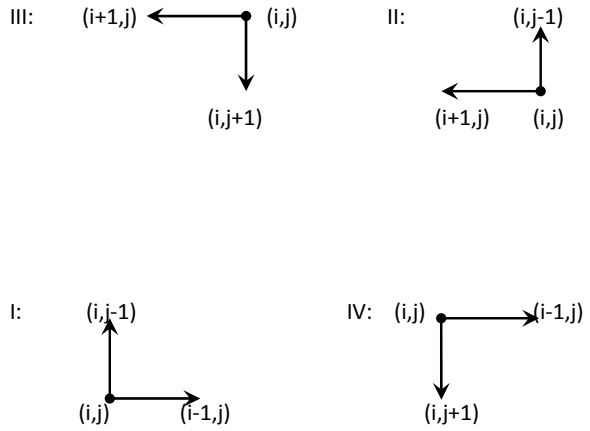

Figure A.4: The representation of upwinding scheme for each corresponding angular quadrant.

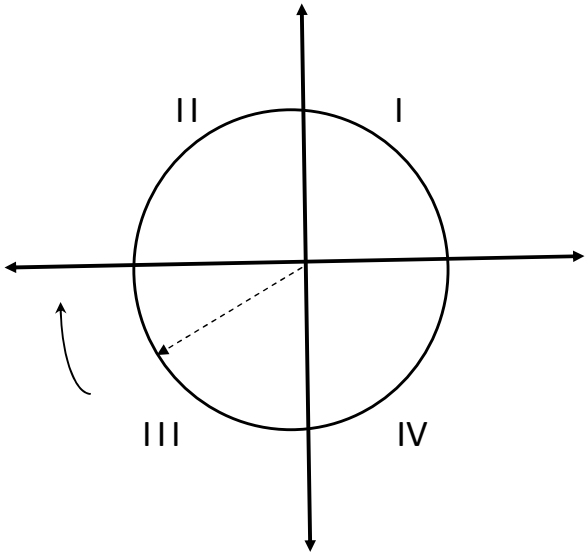

Figure A.5: The sweeping order: from III-II-I-IV

Calling $a_{m3} = \dfrac{\cos\varphi_{m3}}{\Delta x},\ b_{m3} = \dfrac{\sin\varphi_{m3}}{\Delta z},$

$$
\begin{aligned}
&(\mu_a f_a^\ell - a_{m3} - b_{m3}) I^{(s)}_{i,j,m3,\ell} + a_{m3} I^{(s)}_{i+1,j,m3,\ell} + b_{m3} I^{(s)}_{i,j+1,m3,\ell} = \\
&\qquad \mu_a Q Y f_r^\ell p_r(\varphi_m; g) \Delta\varphi_m \Delta\lambda_\ell \tfrac{1}{2} I^{(s-1)}_{1,\ell}(x, z, \varphi_1, \lambda_\ell) f_a^\ell I^{(s-1)}_{m,1}(x, z, \varphi_m, \lambda_1) f_a^1 \\
&\qquad + \mu_a Q Y f_r^\ell p_r(\varphi_m; g) \Delta\varphi_m \Delta\lambda_\ell \times \textstyle\sum_{\ell=2}^{N_\lambda - 1} \sum_{m'=2}^{N_\varphi - 1} 2 I^{(s-1)}_{m',\ell}(x, z, \varphi_{m'}, \lambda_\ell) f_a^\ell
\end{aligned}
\tag{A.6}
$$

where $a_{m3} \leq 0,\ b_{m3} \leq 0$. Taking

$$\begin{aligned} d_{m3,\ell} &= (\mu_a f_a^\ell - a_{m3} - b_{m3}), \\ Q_{i,j,m3,\ell}^{(s-1)} &= \mu_a QY p_r(\varphi_m; g)\Delta\varphi_m\Delta\lambda_\ell \times \frac{1}{2} I_{1,\ell}^{(s-1)}(x, z, \varphi_1, \lambda_\ell) f_a^\ell I_{m,1}^{(s-1)}(x, z, \varphi_m, \lambda_1) f_a^1 \\ &+ \mu_a QY f_r^\ell p_r(\varphi_m; g)\Delta\varphi_m\Delta\lambda_\ell \sum_{\ell=2}^{N_\lambda - 1} \times \sum_{m'=2}^{N_\varphi - 1} 2 I_{m',\ell}^{(s-1)}(x, z, \varphi_{m'}, \lambda_\ell) f_a^\ell, \end{aligned}$$

$I_{i,j,m3,\ell}^{(s)}$ is computed by

$$I_{i,j,m3,\ell}^{(s)} = \frac{-a_{m3} I_{i+1,j,m3,\ell}^{(s)} - b_{m3} I_{i,j+1,m3,\ell}^{(s)} + Q_{i,j,m3,\ell}^{(s-1)}}{d_{m3,\ell}}$$

After computing $I_{i,j,m3,\ell}^{(s)}$ for all i, js, the bottom mirror condition for second quadrant is obtained such that

$$I_{i,0,m2,\ell}^{(s)} = I_{i,0,N_\varphi - m3,\ell}^{(s-1)}$$

Now, on the second quadrant we sweep through right to left by going upward, $i = N_x, \ldots, 1$, $j = 1, \ldots, N_z$ (see Figure A.4). Thereby, the upwinding scheme will be

$$(\mu_a f_a^\ell - a_{m2} + b_{m2}) I_{i,j,m2,\ell}^{(s)} + a_{m2} I_{i+1,j,m2,\ell}^{(s)} - b_{m2} I_{i,j-1,m2,\ell}^{(s)} = Q_{i,j,m2,\ell}^{(s-1)} \tag{A.7}$$

where $a_{m2} \leq 0,\ b_{m2} \geq 0$ and $a_{m2} = \dfrac{\cos\varphi_{m2}}{\Delta x},\ b_{m2} = \dfrac{\sin\varphi_{m2}}{\Delta z}$,

$$d_{m2,\ell} = (\mu_a f_a^\ell - a_{m2} + b_{m2}).$$

Similarly, using the following scheme, $I_{i,j,m2,\ell}^{(s)}$ is computed for all i, js,

$$I_{i,j,m2,\ell}^{(s)} = \frac{-a_{m2} I_{i+1,j,m2,\ell}^{(s)} + b_{m2} I_{i,j-1,m2,\ell}^{(s)} + Q_{i,j,m2,\ell}^{(s-1)}}{d_{m2,\ell}}$$

Since the ordering in $x,\ z$ directions are $i = N_x, \ldots, 1,\ j = 1, \ldots, N_z$, by using partially reflectings BCs at the top surface and left mirror BCs, we can compute

$$I_{i,N_z+1,m3,\ell}^{(1)} = t_{m3} \mathfrak{B}_{m3,\ell}, \tag{A.8}$$

$$I_{i,N_z+1,m3,\ell}^{(s)} = r_{(N_\varphi - m2)} I_{i,N_z+1,N_\varphi - m2,\ell}^{(s-1)},\ (s > 1) \tag{A.9}$$

$$I_{0,j,m1,\ell}^{(s)} = I_{0,j,N_\varphi/2 - m2,\ell}^{(s-1)} \tag{A.10}$$

Now, the sweeping is on the first quadrant in which we will use the above left mirror conditions. The spatial ordering is $i = 1, \ldots, N_x$, $j = 1, \ldots, N_z$

Thus, the upwinding scheme will be

$$(\mu_a f_a^\ell + a_{m1} + b_{m1}) I_{i,j,m1,\ell}^{(s)} - a_{m1} I_{i,j-1,m1,\ell}^{(s)} - b_{m1} I_{i,j-1,m1,\ell}^{(s)} = Q_{i,j,m1,\ell}^{(s-1)} \tag{A.11}$$

where $a_{m1} \geq 0,\ b_{m1} \geq 0$ and $a_{m1} = \dfrac{\cos\varphi_{m1}}{\Delta x},\ b_{m1} = \dfrac{\sin\varphi_{m1}}{\Delta z}$,

$$d_{m1,\ell} = (\mu_a f_a^{\ell} + a_{m1} + b_{m1}).$$

Then, $I^{(s)}_{i,j,m1,\ell}$ for all i, js becomes

$$I^{(s)}_{i,j,m1,\ell} = \frac{a_{m1} I^{(s)}_{i-1,j,m2,\ell} + b_{m1} I^{(s)}_{i,j-1,m1,\ell} + Q^{(s-1)}_{i,j,m1,\ell}}{d_{m1,\ell}}. \tag{A.12}$$

From the first quadrant, the following mirror and top surface BCs are

$$I^{(1)}_{i,N_z+1,m4,\ell} = t_{m4}\mathfrak{B}_{m4,\ell}, \tag{A.13}$$

$$I^{(s)}_{i,N_z+1,m4,\ell} = r_{(N_\varphi - m1)} I^{(s-1)}_{i,N_z+1,N_\varphi - m1,\ell} \tag{A.14}$$

$$I^{(s)}_{0,j,m2,\ell} = I^{(s-1)}_{0,j,N_\varphi/2 - m1,\ell} \tag{A.15}$$

Similarly, we compute $I^{(s)}_{i,j,m4,\ell}$ within spatial ordering $i = 1, \ldots, N_x$, $j = N_z, \ldots, 1$. Using $a_{m4} = \dfrac{\cos\varphi_{m4}}{\Delta x},\ b_{m4} = \dfrac{\sin\varphi_{m4}}{\Delta z}$,

$$(\mu_a + a_{m4} - b_{m4}) I^{(s)}_{i,j,m4,\ell} - a_{m4} I^{(s)}_{i-1,j,m4,\ell} + b_{m4} I^{(s)}_{i,j+1,m4,\ell} = Q^{(s-1)}_{i,j,m4,\ell} \tag{A.16}$$

where $a_{m4} \geq 0,\ b_{m4} \leq 0$. Thus,

$$d_{m4,\ell} = (\mu_a f_a^{\ell} + a_{m4} - b_{m4}),$$

$$I^{(s)}_{i,j,m4,\ell} = \frac{a_{m4} I^{(s)}_{i-1,j,m4,\ell} - b_{m4} I^{(s)}_{i,j+1,m4,\ell} + Q^{(s-1)}_{i,j,m4,\ell}}{d_{m4,\ell}}.$$

Following that, the bottom mirror BCs become

$$I^{(s)}_{i,0,m1,\ell} = I^{(s-1)}_{i,0,N_\varphi - m4,\ell}. \tag{A.17}$$

By using the upwinding numerical scheme as mentioned above, we find iterative solution forms of $I^{(s)}_{i,j,m,\ell}$, $j = 1, \ldots,$ maxiter At first we take $s = 1$, thus $Q^{(0)}_{i,j,m,\ell} = 0$ from the initial guess $I^{(0)}_{i,j,m,\ell} = 0$. After finding $I^{(1)}_{i,j,m,\ell}$, from the first iteration we will have $Q^{(1)}_{i,j,m,\ell}$. Then we keep on iterating the solution until it converges such as $\lim_{s\to\infty} I^{(s)}_{i,j,m,\ell} = 0$.

Relation between the absorption constant and the particle concentration

μ_a and M play important role on initially absorption of light in a luminescent medium (*e*.g., LSC). The following proposition shows the relation between these two quantities.

Proposition. *An absorption constant is proportional to the value of a particle concentration, that is* $\mu_a \sim \ln 10M$.

Proof. To find the relation between those two design parameters, for simplicity let us consider consider the LRTE in $(1+1)$-D case, in which z, λ are spatial and spectral variables, and then analyze the initial absorption of the radiance.

Using the boundary conditions as given in chapter 4, the light is normal incident at the top surface of the LSC and the incident light propagates in z direction, ***i.e.***,

$$\frac{\partial}{\partial z} I(z,\lambda) + \mu_a f_a(\lambda) I(z,\lambda) = 0, \tag{A.18a}$$

$$\text{BC: } I(l_z/2,\lambda) = I_{sol}(\lambda), \tag{A.18b}$$

which describes the initial absorption of the light within the boundary condition before luminescing at longer wavelengths. Solving (A.18), the ratio of the radiance of the absorbed light to the incident radiance becomes

$$\frac{I(z,\lambda)}{I_{sol}(\lambda)} = e^{-\mu_a f_a(\lambda)\Delta z},\ \Delta z = |l_z/2 - z|, \tag{A.19}$$

$\dfrac{I(z,\lambda)}{I_{sol}(\lambda)}$ shows the fraction of light initially **not being** absorbed.

$$P_{abs}(z;\lambda) \sim 1 - e^{-\mu_a f_a(\lambda)\Delta z} \tag{A.20}$$

determines the fraction of light initially **being** absorbed.

Using the Beer Lambert law [45], when $\Delta z = \Delta s$, the probability of absorption is determined by

$$P_{abs}(z;\lambda) \sim 1 - 10^{-f_a(\lambda)M\Delta z}. \tag{A.21}$$

Hence, one can conclude that

$$10^{-f_a(\lambda)M\Delta z} = e^{-\mu_a f_a(\lambda)\Delta z}, \mu_a \sim \ln 10M,\ \ln 10 \sim 2.3.$$

□

Appendix B

Implementation of Monte-Carlo in 2D

Cosine of anisotropic scattering angle

In 2D, for the photon transport inside the semiconductor-based LSC, we consider the following modified Henyey-Greenstein scattering phase function,

$$p(\varphi; g) = \frac{1}{2\pi} \frac{1 - g^2}{(1 + g^2 - 2g\cos 2\varphi)},\ \varphi \in [0, 2\pi] \tag{B.1}$$

This function is normalized such that the integral over unit circle.

$$\int_0^{2\pi} p(\varphi; g) d\varphi = 1 \tag{B.2}$$

In order to use the above phase function for 2D Monte-Carlo model, the accumulated distribution function needs to be used,*i.e.*,

$$P(\varphi; g) = \frac{1}{2\pi} \int_0^{\varphi} \frac{1 - g^2}{(1 + g^2 - 2g\cos 2\varphi)} d\varphi, \tag{B.3}$$

which is

$$P(\varphi; g) = \frac{1}{2\pi} \begin{cases} \tan^{-1}(\frac{1-g}{1+g}\tan\varphi), & \varphi \in [0, \pi/2); \\ \pi + \tan^{-1}(\frac{1-g}{1+g}\tan\varphi), & \varphi \in [\pi/2, 3\pi/2); \\ 2\pi + \tan^{-1}(\frac{1-g}{1+g}\tan\varphi), & \varphi \in [3\pi/2, 2\pi) \end{cases} \tag{B.4}$$

Calling $\xi = P(\varphi; g)$ where $\xi \in [0, 1]$ is uniformly random variable, inverting (B.4) the scattering angle becomes

$$\varphi = \begin{cases} \tan^{-1}(\frac{1-g}{1+g}\tan(2\pi\xi)), & \xi \in [0, 1/4); \\ \tan^{-1}(\frac{1-g}{1+g}\tan(\pi(2\xi - 1))), & \xi \in [1/4, 3/4); \\ \tan^{-1}(\frac{1-g}{1+g}\tan(2\pi(\xi - 1))), & \xi \in [3/4, 1) \end{cases} \tag{B.5}$$

Initial conditions for 2D MC

In the MC simulations, to be consistent with the LRTE all incident photons are assumed to enter the LSC with a probability 1. Thus,

$$T(\varphi) = 1,\ \varphi \in (\pi, 2\pi).$$

After entering through the LSC, the photons are assumed to bounce back from the bottom mirror after entering the LSC, thus the distance photons travel is assumed to be equal to the thickness of the LSC. Here, the initial pathlength

$$\Delta s = |\frac{l_z}{\sin\theta_0}|,\ \theta_0 = 3\pi/2.$$

Initially, $n_p = 10^6$ number of photons are launched simultaneously at the top surface of the LSC. The initial positions of photons are assigned in the vectorized form such that $\mathbf{x}_0, \mathbf{z}_0$, where their length is n_p. Varying $\mathbf{x}_0 \in (-l_x/2, l_x/2]$, the positions vectors are distributed as following,

$$\mathbf{x}_0 = \begin{bmatrix} -l_x/2 \\ -l_x/2 + dx \\ -l_x/2 + 2dx \\ \vdots \\ -l_x/2 + (n_p - (n_p - 2))dx \\ l_x/2 - dx \end{bmatrix}_{n_p \times 1} \tag{B.6}$$

where $dx = l_x/n_p$. For $\mathbf{z}$ initially all entries are same.

$$\mathbf{z}_0 = \begin{bmatrix} l_z/2 \\ \vdots \\ l_z/2 \end{bmatrix}_{n_p \times 1}. \tag{B.7}$$

Therefore, each photon is located at the top surface of the LSC with the values of $(x_0, z_0) \in (\mathbf{x}_0, \mathbf{z}_0)$. Then, inside the LSC, the probability of each photon being absorbed is calculated due to Beer-Lambert law, *i.e.*

$$P_{abs}(\Delta s; \lambda) = 1 - 10^{-\epsilon(\lambda) M \Delta s}.$$

In the MC simulations, if the light is not initially being absorbed, it is assumed be lost. However, for the insufficient ratio of the initial absorption, very small percentage of light can still be trapped inside of the LSC via total internal reflections, and then guided to the PV. For sufficiently higher particle concentration,*i.e.*$\mu_a \sim \mathcal{O}(10^4)$, Δs becomes very small $\sim \mathcal{O}(10^{-6})$. This increases the number of the multiple reabsorption inside of the LSC.

Bibliography

[1] S. Chandrasekhar, *Radiative Transfer*, Dover Publications Inc., 1960.

[2] A. Ishimaru, *Wave Propagation and Scattering in Random Media*, Wiley-IEEE-Press, 1999.

[3] K. M. Case and P. F. Zweifel, *Linear Transport Theory*, Addison-Wesley, 1967.

[4] E. E. Lewis and W. F. J. Miller, *Computational Methods of Neutron Transport*, Wiley, 1984.

[5] L. Wang and H. Wu, *Biomedical optics: Principles and imaging*, Wiley, 2007.

[6] A. N. Society, A. Goodjohn, and G. Pomraning, *Reactor Physics in the Resonance and Thermal Regions: Neutron thermalization*, Reactor Physics in the Resonance and Thermal Regions: Proceedings of the National Topical Meeting of the American Nuclear Society, San Diego, February 7-9, 1966, M.I.T. Press, 1966.

[7] S. A. Bludman and K. A. Van Riper, Astrophysical Journal **224**, 631 (1978).

[8] F. Scheben and I. G. Graham, SIAM J. Sci. Comput. **33**, 2785 (2011).

[9] C. Hutchinson, J. Lakowicz, and E. Sevick-Muraca, Biophysical Journal **68**, 1574 (1995).

[10] G. Y. Panasyuk, Z.-M. Wang, J. C. Schotland, and V. A. Markel, Opt. Lett. **33**, 1744 (2008).

[11] A. D. Zacharopoulos,and P. Svenmarker, J. Axelsson, M. Schweiger,and Simon R. Arridge,and S. Andersson-Engels, Appl. Phys. Lett. **17**, 3042 (2009).

[12] C. T. Xu, J. Axelsson, and S. Andersson-Engels, Appl. Phys. Lett. **94**, 251107 (2009).

[13] A. Joshi, J. C. Rasmussen, E. M. Sevick-Muraca, T. A. Wareing, and J. McGhee, Physics in medicine and biology **53**, 2069 (2008).

[14] D. Yudovsky and L. Pilon, Appl. Opt. **49**, 6072 (2010).

[15] Kai Liu, Yujie Lu, Jie Tian, Chenghu Qin, Xin Yang, Shouping Zhu, Xiang Yang, Quansheng Gao, and Dong Han, Opt. Express **18**, 20988 (2010).

[16] F. Martelli, S. D. Bianco, and P. D. Ninni, Biomed. Opt. Express **3**, 26 (2012).

[17] Jinchao Feng, Chenghu Qin, Kebin Jia, Shouping Zhu, Xin Yang, Jie Tian, IEEE J. Sel. Top. Quant. **18**, 1394 (2012).

[18] A. D. Klose and T. Pöschinger, Physics in Medicine and Biology **56**, 1443 (2011).

[19] D. Şahin and B. Ilan, J. Opt. Soc. Am. A **30**, 813 (2013).

[20] S. Leyre et al., Opt. Express **20**, 17856 (2012).

[21] D. Şahin, B. Ilan, and D. F. Kelley, Photon transport in luminescent solar concentrators based on semiconductor nanoparticles, in *Optical Nanostructures and Advanced Materials for Photovoltaics*, Optical Society of America, 2011.

[22] D. Şahin, B. Ilan, and D. Kelley, J. of Appl. Phys **110**, 1 (2011).

[23] D. Şahin and B. Ilan, Modeling light propagation in semiconductor-based luminescent solar concentrators, in *SPIE Optical Engineering + Applications*, pages 883409–883409, International Society for Optics and Photonics, 2013.

[24] D. Şahin, B. Ilan, Asymptotic solution of light transport problems in optically-thick luminescent media, (*submitted*).

[25] The International Energy Agency, Solar energy perspective: executive summary, Technical report, ECD/IEA, 2011.

[26] W. H. Weber and J. Lambe, Appl. Optics **15**, 2299 (1976).

[27] A. Goetzberger and W. Greubel, J. Appl. Physics **14**, 123 (1977).

[28] J. S. Batchelder, A. H. Zewail, and T. Cole, Appl. Opt. **18**, 3090 (1979).

[29] R. W. Olson, F. L. Roger, and M. D. Fayer, Appl. Opt. **20**, 2934 (1981).

[30] M. S. de Cardona, M. Carrascosa, F. Meseguer, F. Cusso, and F. Jaque, Appl. Opt. **20**, 2934 (1985).

[31] Paul P. C. Verbunt, Shufen Tsoi, Michael G. Debije, Dirk. J. Broer, Cees W.M. Bastiaansen, Chi-Wen Lin, and Dick K. G. de Boer, Opt. Express **20**, 655 (2012).

[32] S. McDowall, B. L. Johnson, and D. L. Patrick, J. of Appl. Phys. **108**, 053508 (2010).

[33] W. G. V. Sark et al., Opt. Express **16**, 21773 (2008).

[34] B. Rowan, L. Wilson, and B. Richards, IEEE Journal Of Selected Topics In Quantum Electronics **14**, 1312 (2008).

[35] M. J. Currie, J. K. Mapel, T. D. Heidel, S. Goffri, and M. A. Baldo, Science **321**, 226 (2008).

[36] A. Chatten, K. Barnham, B. Buxton, N. Ekins-Daukes, and M. Malik, Semiconductors **38**, 909 (2004).

[37] V. Sholin, J. D. Olson, and S. A. Carter, J. Appl. Phys. **101**, 123114 (2007).

[38] M. G. Hyldahl, S. T. Baileya, and B. P. Wittmershaus, Solar Energy **83**, 566 (2009).

[39] G. V. Shcherbatyuk, R. H. Inman, C. Wang, R. Winston, and S. Ghosh, Appl. Phys. Lett. **96**, 191901 (2010).

[40] S. Kim, B. Fisher, H.-J. Eisler, and M. Bawendi, Journal of the American Chemical Society **125**, 11466 (2003).

[41] C.-H. Chuang, S. S. Lo, G. D. Scholes, and C. Burda, The Journal of Physical Chemistry Letters **1**, 2530 (2010).

[42] T. Ju, L. Yang, and S. Carter, Journal of Applied Physics **107**, 104311 (2010).

[43] N. Metropolis and S. Ulam, J. of the American Statistical Association **44**, 335 (1949).

[44] S. A. Prahl, M. Keizer, S. L. Jacques, and A. J. Welch, SPIE Institute Series **IS**, 102 (1989).

[45] W. Yu, L. Qu, W. Guo, and X. Peng, Chem. Matter **15**, 2854 (2003).

[46] M. Born and E. Wolf, *Principles of Optics: Electromagnetic Theory of Propagation, Interference and Diffraction of Light*, Cambridge University Press, 7 edition, 2005.

[47] K. Emery, Technical report, ASTM, http://rredc.nrel.gov/solar/spectra/am1.5, 2000.

[48] M. Kennedy, S. McCormack, J. Doran, and B. Norton, Ray-trace modelling of reflectors for quantum dot solar concentrators, in *High and Low Concentration for Solar Electric Applications*, edited by M. Symko-Davies, volume 6649 of *Proc. SPIE*, pages 664905 1–4, 2007.

[49] M. G. Debije et al., Appl. Opt. **49**, 745 (2010).

[50] P. P. C. Verbunt et al., Advanced Functional Materials **19**, 2714 (2009).

[51] C. L. Mulder et al., Opt. Express **18**, A79 (2010).

[52] C. L. Mulder et al., Opt. Express **18**, A91 (2010).

[53] R. W. MacQueen, Y. Y. Cheng, R. G. C. R. Clady, and T. W. Schmidt, Opt. Express **18**, A161 (2010).

[54] J. Hu et al., Science **292**, 2060 (2001).

[55] J. Hu, Wang, L.-s. Li, W. Yang, and A. P. Alivisatos, The Journal of Physical Chemistry B **106**, 2447 (2002).

[56] A. Shabaev and A. L. Efros, Nano Letters **4**, 1821 (2004).

[57] F. Shieh, A. E. Saunders, and B. A. Korgel, The Journal of Physical Chemistry B **109**, 8538 (2005).

[58] M. Jones, S. Kumar, S. S. Lo, and G. D. Scholes, The Journal of Physical Chemistry C **112**, 5423 (2008).

[59] L. Xi, C. Boothroyd, and Y. M. Lam, Chemistry of Materials **21**, 1465 (2009).

[60] T. Jevremovic, *Nuclear Principles in Engineering*, Springer, 2009.

[61] J. Bertolotti, Elbert G. van Putten, Christian Blum, Ad Lagendijk, Willem L. Vos, and Allard P. Mosk, Nature **491**, 232 (2012).

[62] L. G. Henyey and J. L. Greenstein, J. Astrophys. **93**, 70 (1941).

[63] A. Chatten, K. Barnham, B. Buxton, N. Ekins-Daukes, and M. Malik, Semiconductors **38**, 909 (2004).

[64] D. Yudovsky and L. Pilon, Appl. Opt. **49**, 6072 (2010).

[65] James T. Kajiya, Siggraph **20**, 143 (1986).

[66] D. D. Cooke and M. Kerker, J. Opt. Soc. Am. A. **59**, 43 (1969).

[67] E. Hecht, *Optics*, Addison-Wesley, 1987.

[68] F. Purcell-Milton and Y. K. Gun'ko, J. Mater. Chem. **22**, 16687 (2012).

[69] H. Gao and H. Zhao, Transport Theory and Statistical Physics **38**, 149 (2009).

[70] G. Bal and O. Pinaud, Wave Motion **43**, 561 (2006).

[71] V. A. Markel and J. C. Schotland, JOSA A **19**, 558 (2002).

[72] J. Heino, S. Arridge, J. Sikora, and E. Somersalo, Phys. Rev. E **68**, 031908 (2003).

[73] H. Ammari, E. Bossy, J. Garnier, W. Jing, and L. Seppecher, J. of Math. Phys. **54**, 021501 (2013).

[74] W. E. Meador and W. R. Weaver, Appl. Opt. **18**, 1204 (1979).

[75] K. M. Yoo, F. Liu, and R. R. Alfano, Phys. Rev. Lett. **64**, 2647 (1990).

[76] G. Bal and L. Ryzhik, SIAM Journal on Applied Mathematics **60**, pp. 1887 (2000).

[77] G. Y. Panasyuk, V. A. Markel, and J. C. Schotland, Appl. Phys. Lett. **87**, 101111 (2005).

[78] R. Sanchez, J. Ragusa, and E. Masiello, J. of Math. Phys. **49**, 083504 (2008).

[79] E. W. Larsen and J. B. Keller, J. Math. Phys. **15**, 75 (1974).

[80] G. J. Habetler and B. J. Matkowsky, Journal of Mathematical Physics **16** (1975).

[81] E. W. Larsen, J. E. Morel, and W. F. M. Jr., J. of Comput. Phys. **69**, 283 (1987).

[82] A. D. Kim, J. Opt. Soc. Am. A **28**, 1007 (2011).

[83] A. Kim and M. Moscoso, Multiscale Modeling & Simulation **9**, 1624 (2011).

[84] J. Mika, Journal of Quantitative Spectroscopy and Radiative Transfer **11**, 879 (1971).

[85] F. Malvagi and G. C. Pomraning, Journal of Mathematical Physics **32**, 805 (1991).

[86] R. C. Haskell et al., J. Opt. Soc. Am. A **11**, 2727 (1994).

[87] R. Aronson, J. Opt. Soc. Am. A **12**, 2532 (1995).

[88] C. L. Leakeas and E. W. Larsen, Nuclear science and engineering **137**, 236 (2001).

[89] A. D. Kim and J. B. Keller, J. Opt. Soc. Am. A **20**, 92 (2003).

[90] K. G. Phillips and C. Lancellotti, Appl. Opt. **48**, 229 (2009).